國立交通大學

材料科學與工程學系

博士論文

一維暨二維氧化鋅奈米光電特性及結構研究

Optoelectronic Characteristics and Structure Development of One- and Two-Dimensional Zinc Oxide Materials

研究生：林晉慶

指導教授：陳三元 教授

中華民國九十五年六月

一維暨二維氧化鋅奈米光電特性及結構研究

Optoelectronic Characteristics and Structure Development of One- and Two-Dimensional Zinc Oxide Materials

學生：林晉慶　　Student: Chin-Ching Lin

指導教授：陳三元　　Advisor: Prof. Dr. San-Yuan Chen

國立交通大學
材料科學與工程學系
博士論文

A Dissertation
Submitted to Department of Materials Science and Engineering
College of Engineering
National Chiao Tung University
In Partial Fulfillment of the Requirements for the Degree of Doctor of Philosophy
in

Materials Science and Engineering

June 2006

Hsinchu, Taiwan, Repubile of China

中華民國九十五年六月

Contents

Acknowledgments

First of all, I am deeply appreciative to my supervisor Prof. Dr. San-Yuan Chen for his all-out supports, useful discussions and kindness advices during my study period. Prof. Dr. San-Yuan Chen is not only a benevolent advisor but also a very erudite philosopher. I have benefited much from his philosophy of life. I also sincerely thank Dr. Syh-Yuh Cheng of the Industrial Technology Research Institution for his fruitful discussions and warmhearted help in my thesis work. Moreover, I am grateful to Prof. Dr. Klaus von Klitzing and my co-advisor Dr. Siegmar Roth for giving me an opportunity to visit their impressive department and enthusiastic laboratory during the period when I studied at Max-Planck Institut für Festkoerperforschung in Stuttgart of Germany.

My works have largely been a collaborative effort. Therefore, I would like to thank my colleagues: Mr. Kun-Ho Liu, Mrs. Hung-Pei Chen, Mr. Pai-Chia Kuo, Miss Shu-Ping Lee, Mr. Hung-Chou Liao and Mr. Chi-Sheng Hsiao of the National Chiao Tung University in Taiwan and Dr. Miroslav Haluska, Prof. Dr. Viera Skakalova, Dr. Yun Sung Woo, Dr. Ursula Dettlaff, Dr. Martti Kaempgen, Dr. Jannik Meyer, Dr. Dirk Obergfell, Dr. Michael Schmid, Dr. Mitauharu Konuma, Dr. Michael Lebert, Prof. Dr. Po-Wen Chiu, Mr. Chen-Wei Liang, Mr. Jiangping Wang, Mr. Serhat Sahakalkan, Mr. Viktor Siegle, Mr. Bjoern Hornbostel, Mr. Alberto ansaldo, Mr. Thomas Reindl, Miss Franziska Koch and Mr. Jiri Cech of Max-Planck Institut für Festkoerperforschung in Stuttgart for supplying the valuable suggestions and sharing their time with me. Finally, I want to thank my family and friends for their selfless supports and encouragement during my study period.

Chin-Ching Lin, Taiwan, 10, 05, 2006

Abstract

Zinc oxide (ZnO) has unique physical properties that make it a most promising material for optoelectronic device. The main reasons are a direct band gap of 3.3 eV and a large exciton binding energy (60 meV), which permits exciton recombination even above room temperature. Owing to its distinctive characteristics the research trend on ZnO has continued for many decades. The former studies are focused on the basic physical properties of three- and two-dimensional ZnO materials, such as lattice parameter, vibrational properties, and optical studies. As improving the technology of materials growth, scientists have more opportunities to produce high-quality ZnO materials and then can do deeply research in it. In this nearly decade, the main obstacle to the development of ZnO has been the lack of reproducible and low-resistivity *p*-type ZnO. For the moment, many groups have attacked this problem and several have been successful to solve some problems of them **[64-67]**. Moreover, theoreticians have also been active in this area, and have predicted the electrical activities of various dopants and native defects **[68-70]**. In addition to ZnO thin films, significant interest has emerged in the synthesis of nanoscale ZnO materials, in recent years. It is due to the one-dimensional ZnO nanostructures provide an attractive candidate system for fundamental quantization and low-dimensional transport studies for chemical sensing and biomedical applications. This thesis outlines the process of fabricating *p*-type ZnO thin films and one-dimensional ZnO nanostructures, as well as the study of their physical properties.

In chapter 1 we will present an introductory overview to ZnO materials. It is devoted, respectively, fundamental, doping, and defects properties in ZnO. Chapter 2 will discuss the fabrication of one- and two-dimensional ZnO materials and basic

theoretical concepts of nanoscience. This chapter also includes how we developed high-quality ZnO films and nanorods and measured their excellent physical properties. The individual nanorod measurement setup for electrical transport is also shown in this chapter.

Chapter 3 discusses the defects engineering on ZnO thin films. The transitions of native defects in ZnO are inspected by photoluminescence (PL) spectroscopy, in this study. Different buffer-layers could change the concentration of native defects and improve the physical properties of ZnO. We will, therefore, discuss the relationship between the predominant defects and PL emissions in the ZnO films. In chapter 4, we will present the results for the electrical and optical properties of group-V elements doping in ZnO films. Reproducible *p*-type ZnO films with high carrier concentration (7.3×10^{17} cm^{-3}) are fabricated by nitrogen-implanted on nitride layer and then annealed at 850 ^{o}C in N_2 ambient.

To date, the most popular method to grow ZnO nanorods is vapor-solid process. However, this method is usually operated under high temperature and it has also locked the size of the sample due to the size of the furnace. In chapter 5, we will show a convenient method to produce large scale ZnO nanorods on organic and inorganic substrates. The growth mechanism and thermal annealed effect of ZnO nanorods will be investigated by high-resolution transmission electron microscopy. The plasma treatments are used to improve the luminescent and electrical properties in ZnO nanorods. The high conductivity n-type and rectifying behavior p-type ZnO nanorods are revealed in chapter 6. The electrical transport of individual ZnO nanorods and single-walled carbon nanotubes composite will be discussed in chapter 7.

Chapter 1

Introduction

1.1 Zinc oxide materials

Nowadays, ZnO is attracting attention for its application to ultraviolet (UV) light-emitters, transparent high power electronics, surface acoustic wave devices, piezoelectric transducers, gas-sensing and solar cells. Some optoelectronic applications of ZnO have advantages over GaN, another wide-gap semiconductor (*Eg* ~3.4 eV at 300 K) and widely used for production of light-emitting devices, because of its availability in bulk, single-crystal form and its larger exciton binding energy (60 meV at 300K) **[1-15]**. As a wide bandgap semiconductor, ZnO is a candidate host for solid state blue to UV optoelectronics, including laser development. This has important applications in high density data storage systems, solid-state lighting, secure communications and bio-detection **[16]**. Transparency to visible light provides opportunities to develop transparent electronics, UV optoelectronics, and integrated sensors, all from the same material system. ZnO is a direct bandgap semiconductor with Eg~3.2 eV. The bandgap of ZnO can be tuned via divalent substitution on the cation site.

It is well-known that ZnO is not really a newly discovered material. Interest in this material at the time of this writing is again at a high point. In terms of its characterization, reports go back to 1935 or even earlier. Studies of ZnO properties presume that ZnO samples were available. Growth methods not much different from what is employed lately have been explored, among which are chemical-vapor transport, vapor-phase growth, hydrothermal, high-quality platelets. ZnO has recently found other niche applications as well, such as fabrication of transparent thin-film transistors, where the protective covering preventing light exposure is eliminated since ZnO-based transistors are insensitive to visible light. Today scientists can use heavy substitutional doping method to increase the carrier concentrations up to $2x10^{21}$ cm^{-3}. By controlling the doping level electrical properties can be changed from insulator through *n*-type semiconductor to metal while keeping optical transparency that makes it useful for transparent electrodes in flat-panel displays and field effect transistor.

However, an important problem should be overcome before ZnO transforms into a potential optoelectronics devices in the world: the fabrication of *p*-type-conductivity ZnO materials. Notwithstanding all the progress that has been made and the reports of *p*-type conductivity in ZnO films using various growth methods and various group-V dopant elements (N, P, and As), a reliable and reproducible high quality *p*-type conductivity has not yet been achieved for ZnO. Therefore, it remains to be the major topic in ZnO research today, and congruently most of the research efforts are directed just to solving this problem. Many results are just heralds of what can be expected of ZnO in an effort to position it for future device applications. As in the early developments of GaN predating the demonstration of *p*-type conductivity, metal-insulator-semiconductor device structures not requiring *p*-type ZnO have been introduced but lack the high efficiency.

1.2 Physical characteristics of ZnO materials

1.2.1 Crystal and electronic band structures

(i) Crystal structure

Most of the group *II-VI* binary compound semiconductors crystallize in either cubic zinc-blende or hexagonal wurtzite structure where each anion is surrounded by four cations at the corners of a tetrahedron, and vice versa. This tetrahedral coordination is typical of sp^3 covalent bonding, but these materials also have a substantial ionic character. ZnO is an II-VI compound semiconductor whose ionicity resides at the borderline between covalent and ionic semiconductor. The crystal structures shared by ZnO are wurtzite, zinc blende, and rocksalt. At ambient conditions, the thermodynamically stable phase is wurtzite, as schematically shown in **Figure 1.1a**. The zinc-blende ZnO structure can be stabilized only by growth on cubic substrates, and the rocksalt structure may be obtained at relatively high pressures.

The wurtzite structure has a hexagonal unit cell with two lattice parameters, *a* and *c*, in the ratio of c/a=1.633 and belongs to the space group of $P6_3mc$. The structure is composed of two interpenetrating hexagonal-close-packed sublattices, each of which consists of one type of atom displaced with respect to each other along the threefold *c*-axis by the amount of u =3/8=0.375 (in an ideal wurtzite structure) in fractional coordinates. Each sublattice includes four atoms per unit cell and every atom of one kind (group-II atom) is surrounded by four atoms of the other kind (group VI), or vice versa, which are coordinated at the edges of a tetrahedron **[17]**. In a real ZnO crystal, the wurtzite structure deviates from the ideal arrangement, by changing the c/a ratio or the u value. It should be pointed out that a strong correlation exists between the c/a ratio and the u parameter in that when the c/a ratio decreases, the u parameter increases in such a way that those four tetrahedral distances remain nearly constant through a distortion of tetrahedral angles due to long-range polar interactions. Since the c/a ratio also correlates with the difference of the electron negativities of the two constituents, components with the greatest differences show the largest departure from the ideal c/a ratio.

The convention is that the [0001] axis points from the face of the O plane to the Zn plane and is the positive z direction. In other words, when the bonds along the c direction are from cation (Zn) to anion (O), the polarity is referred to as Zn polarity. By the same argument, when the bonds along the c direction are from anion (O) to cation (Zn), the polarity is referred to as O polarity. Many properties of the material depend also on its polarity, for example, growth, etching, defect generation and plasticity, spontaneous polarization, and piezoelectricity. In wurtzite ZnO, besides the primary polar plane (0001) and associated direction <0001>, which are the most commonly used surface and direction for growth, many other secondary planes and directions exist in the crystal structure.

(ii) Electronic band structures

The band structure of a given semiconductor is pivotal in determining its potential utility. Consequently, an accurate knowledge of the band structure is critical if the semiconductor in question is to be incorporated in the family of materials considered for device applications. Several theoretical approaches of varying degrees of complexity have been employed to calculate the band structure of ZnO for its wurzite, zinc-blende, and rocksalt. **Figure 1.1b** shows the calculated band structure and the total density of states of ZnO for wurzite phase. Besides, a number of experimental data have been published regarding the band structure of the electronic states of wurtzite ZnO. X-ray or UV reflection/absorption or emission techniques have conventionally been used to measure the electronic core levels in solids. These methods basically measure the energy difference by inducing transitions between electronic levels. For example, transitions from the upper valence band states to the upper conduction band states, and from the lower valence-band states, or by exciting collective modes,such as, the upper core states to the lower edge of the conduction band and to excitations of plasmons. After the theoretical work on band-structure calculation of ZnO proposed by Rössler using Green's function in 1969, there have been several experimental works **[18-19]** performed on the wurtzite ZnO which proved Rössler's predicted bulk electronic structure to be far from satisfactory.

Langer and Vesely **[20]** have reported experimental data related to the energy levels of core electrons in ZnO using x-ray-induced photoemission spectroscopy. They have drawn two conclusions from their studies: (a) the location of the Zn 3*d* level in ZnO has been unambiguously determined and (b) the discrepancy between the measured values and the theoretically determined energy values was angular momentum dependent. Powell *et al.* **[18]** have carried out UV photoemission measurements on hexagonal ZnO cleaved in vacuum. Those authors have placed the Zn 3*d* core level at about 7.5 eV below the valence-band maximum, which is 3 eV lower than the value predicted by Rössler's band calculation. In the following years, LDA and tight binding methods were employed **[21,22]** by considering the Zn 3*d* states as core levels to ease calculations. Satisfactory agreement with qualitative valence-band dispersions was achieved with this assumption. However, quantitative disagreements remained and the location of the Zn 3*d* states could not be predicted.

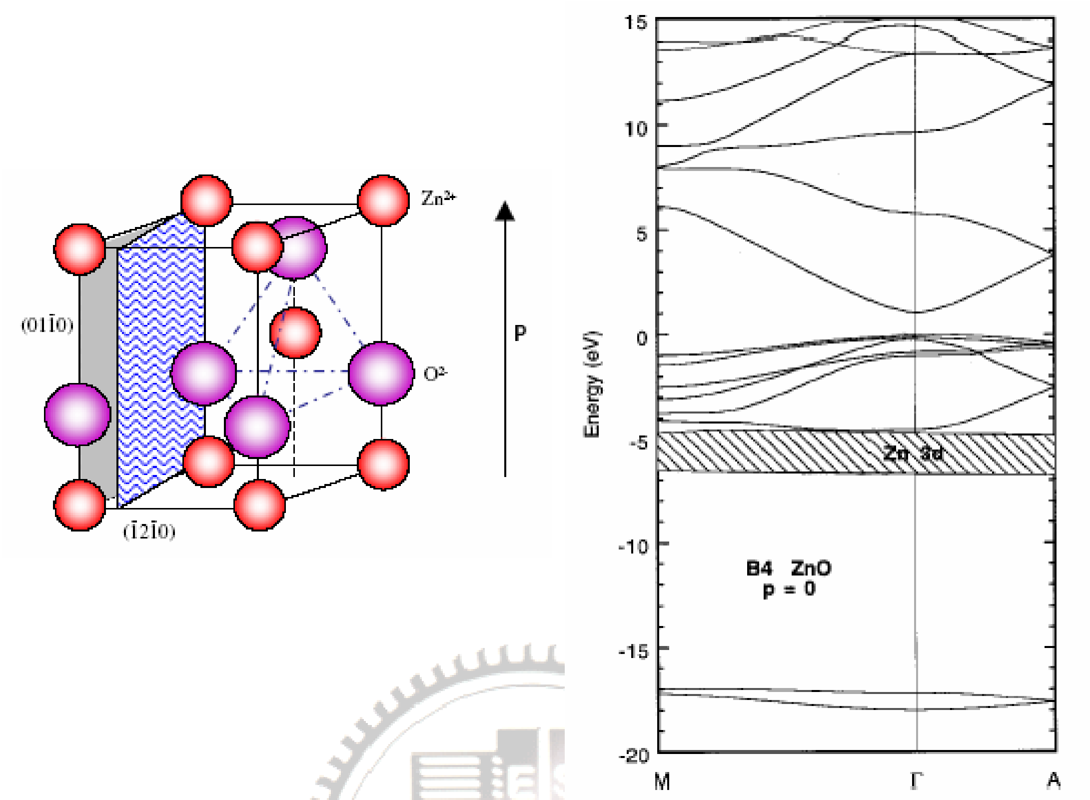

Figure 1.1: (a) Crystal structure, and (b) Band structure for wurtize type in the ZnO **[33]**.

Recently, Girard *et al.* **[23]** have studied the electronic structure of the ZnO (0001) surface by angle-resolved photoelectron spectroscopy. They recorded both normal and off normal emission spectra, which give valuable information about bulk and surface states as well as the Zn 3*d* states. In these measurements, the binding energies were referred to the Fermi level and the intensities were normalized to the photon flux. Among all the spectra displayed, seven features were seen, labeled from A to G. The dispersions of the four valence bands observed in the (0001) direction were compared with theory based on LDA calculations, which consider the Zn 3*d* electrons as part of the valence band, **[24]** and good agreement was realized. It should also be noted that the Zn 3*d* states were observed to separate into two groups of four and six bands, which show dispersion with *k*, which is in agreement with theoretical results, but the location of these states were not accurately predicted.

The polar (0001)-Zn and (000-1)-O surfaces and the nonpolar (10-10) surface (*m* plane) have also been the object of experimental and theoretical investigations. Of these surfaces, the nonpolar (10-10) surface is of particular interest from the viewpoint of surface chemistry, because the surface is terminated with the same number of O and Zn atoms. The low-energy electron-diffraction (LEED) studies have revealed that the surface undergoes relaxation, which is characterized by downward shift of both surface Zn and O atoms, with a greater shift for the Zn atom than the O atom, resulting in the Zn–O bond rotation by 6.2° or 11.5° **[25]** with respect to the ideal surface plane. Such a surface relaxation should influence the energetic position as well as the dispersion width of the surface dangling bond bands of the occupied O 2*p* and unoccupied Zn 4*s* states. Besides, several theoretical studies have indicated that, upon relaxation, the O 2*p* dangling-bond state is stabilized while the Zn 4*s* dangling-bond state shifts up in energy. **[26]** The theoretically determined position of these dangling-bond bands, especially the occupied O 2*p* dangling-bond band, relative to the bulk bands projected onto the (10-10) surface varies depending on the method employed in the calculations.

The theoretical calculation of the band structure of ZnO mostly involve the LDA, **[24,27,28]**which is very demanding because of the cationic *d* electrons. If the *d* electrons are treated as core electrons, the calculated lattice constant underestimates the experimental values by as much as 18% for wurtzite ZnO, while inclusion of the *d* electrons in the valence band yields very accurate lattice constants. However, even if the *d* electrons are properly taken into account, the results of standard LDA calculations show distinct shortcomings, such as strongly underestimated band gap and overestimated occupied cationic *d* bands, which roughly reside 3 eV high in energy as compared to experiment. In addition, their interactions with the anion *p* valence bands are artificially enlarged, resulting in overestimated dispersion and bandwidth of the latter and shifting them unphysically close to the conduction bands. Zakharov *et al.* **[29]** have recently reported plane-wave *GW* method for a number of II-VI compounds. They simply treated the *d* electrons as core electrons and deliberately carried out their *GW* calculation at the experimental lattice constants. They obtained very good results for the anion *p* valence bands and for the band-gap energies but no assertion concerning the *d*-band positions could be made. Recently, Vogel *et al.* **[30]** suggested an alternative approach to treat the II-VI semiconductor compounds, which approximately incorporates dominant self-interaction corrections. It has been shown that self-interaction corrections to LDA can be very important for a quantitative description of a system with strongly localized states such as 3*d* electrons. The electronic band structure of the other phases of ZnO has also been studied by a number of researchers [**30-32**]. When wurtzite ZnO is compressed, it has been observed that the peak at the top of the upper valence band is slightly reduced in height and shifted down in energy, the O 2*s* and Zn 3*d*-derived peaks are slightly broadened and shifted up in energy, and a splitting appears in the Zn 3*d* states.

1.2.2 Electrical behaviors

As a direct and large-band-gap material, ZnO is attracting a lot of attention for a variety of electronic and optoelectronic applications. Advantages associated with a large band gap include higher breakdown voltages, ability to sustain large electric fields, lower noise generation, and high temperature and high power operation. The electron transport in semiconductors can be considered for low and high electric fields. (a) At sufficiently low electric fields, the energy gained by the electrons from the applied electric field is small compared to the thermal energy of electrons, and therefore, the energy distribution of electrons is unaffected by such a low electric field. Since the scattering rates determining the electron mobility depend on the electron distribution function, electron mobility remains independent of the applied electric field, and Ohm’s law is obeyed. (b) When the electric field is increased to a point where the energy gained by electrons from the external field is no longer negligible compared to the thermal energy of the electron, the electron distribution function changes significantly from its equilibrium value. These electrons become hot electrons characterized by an electron temperature larger than the lattice temperature. Furthermore, as the dimensions of the device are decreased to submicron range, transient transport occurs when there is minimal or no energy loss to the lattice during a short and critical period of time, such as during transport under the gate of a field-effect transistor or through the base of a bipolar transistor. The transient transport is characterized by the onset of ballistic or velocity overshoot phenomenon. Since the electron drift velocity is higher than its steady-state value, one can design a device operating at frequencies exceeding those expected from linear scaling of dimensions.

Hall effect is the most widely used technique to measure the transport properties and assess the quality of epitaxial layers. For semiconductor materials, it yields the carrier concentration, its type, and carrier mobility. More specifically, experimental data on Hall measurements over a wide temperature range, as 4.2–300 K, provide quantitative information on impurities, imperfections, uniformity, scattering mechanisms, etc. The Hall coefficient and resistivity (ρ) are experimentally determined and then related to the electrical parameters through (for n-type conduction) $R_H=r_H/ne$ and $\mu H=R_H/\rho$, where n is the free-electron concentration, e is the unit electronic charge, μH is the Hall mobility, and r_H is the Hall scattering factor which is dependent on the particular scattering mechanism. The drift mobility is the average velocity per unit electric field in the limit of zero electric field and is related to the Hall mobility through the Hall scattering factor by $\mu_H = r_H\mu$. As noted above, the Hall scattering factor depends on the details of the scattering mechanism, which limits the drift velocity. As the carriers travel through a semiconductor, they encounter various scattering mechanisms that govern the carrier mobility in the electronic system. The parameter for characterizing the various scattering mechanisms is the relaxation time τ, which determines the rate of change in electron momentum as it moves in the semiconductor crystal.

Experimental investigation of the temperature-dependent carrier mobility and concentration can be used to determine the fundamental material parameters and understand the carrier scattering mechanisms along with an accurate comparison with theory. The transport properties reported in the literature are mostly based on Hall-effect measurements, assuming the Hall scattering factor to be unity. Using Monte Carlo simulations, Albrecht *et al.* **[34,35]** predicted the room-temperature electron mobility of ZnO as 300 cm^2/Vs. Nominally undoped ZnO with a wurtzite structure naturally becomes an *n*-type semiconductor due to the presence of intrinsic or extrinsic defects, which were generally attributed to native defects, such as O_{Zn}, Zn_i, and V_O.

Ohmic and Schottky contacts on ZnO

An Ohmic contact can be defined as having a linear and symmetric current-voltage relationship for both positive and negative voltages and is so important for carrying electrical current into and out of the semiconductor, ideally with no parasitic resistance. The major loss of device performance is often caused by high-resistance metal-semiconductor Ohmic contacts through thermal stress and or contact failure

[36]. Thus, in order to attain high-performance ZnO-based optical and electrical devices, it is essential to achieve Ohmic contacts that have both low resistance and are thermally stable and reliable. This can be achieved either by performing surface preparation to reduce the metal-semiconductor barrier height which would allow to increase carrier tunneling probability or by increasing the effective carrier concentration of the surface perhaps taking advantage of oxygen loss **[37,38]**. In ZnO, Specific contact resistances of $3x10^{-4}$ Ωcm^2 were reported for Pt-Ga contacts on n-ZnO epitaxial layers **[39]**, $2x10^{-4}$ Ωcm^2 for Ti/Au on Al-doped epitaxial layers **[40]**, 0.7 Ωcm^2 for non-alloyed In on laser-processed n-ZnO substrates **[41]**, $2.5x10^{-5}$ Ωcm^2 for non-alloyed Al on epitaxial n-type ZnO **[42]**, $7.3x10^{-3}$ to $4.3x10^{-5}$ Ωcm^2 for Ti/Au on plasma exposed, Al-doped n-type epitaxial ZnO **[43]** and 9 $x10^{-7}$ Ωcm^2 for Ti/Al on n^+ epitaxial ZnO **[44]**.

The chemical reactions between the metal and the semiconductor, the surface states, the contaminants, the defects in the surface layer, and the diffusion of the metal into the semiconductor are well-known problems in the formation of Schottky contacts. To create Schottky barrier with undoped ZnO, a high work function can be applied to the surface of a ZnO crystal. Many publications reveal that Au has some serious problems at high temperatures, **[45,46]** but it has widely been applied to ZnO to form Schottky barriers **[45-47]**. Au and Ag Schottky contacts on (0001) Zn surface of undoped *n*-ZnO samples have been investigated by Polyakov *et al.*, **[46]** comparing their barrier heights and thermal stabilities. Schottky barrier heights of 0.65–0.69 eV and diode ideality factors of 1.6–1.8 have been obtained by capacitance-voltage and current-voltage measurements, respectively. The ideality factor had a value close to 2 for almost all the samples studied due to an increase of the tunneling current through the junction. Some authors have reported good electrical performance of the Schottky diodes after etching in concentrated nitric acid **[48]**. However, it should be noted that in the majority of papers the ideality factors of the ZnO Schottky diodes are considerably higher than unity which has been explained by the prevalence of tunneling, the impact of interface states or the influence of deep recombination centers.

1.2.3 Luminescent properties

(i) Basic concept of excitons

The absorption of a photon by an interband transition in a semiconductor or insulator creates an electron in the conduction band and a hole in the valence band. The oppositely charged particles are created at the same point in space and can attract each other through their mutual Coulomb interaction. This attractive interaction increases the probability of the formation of an electron-hole pair, and therefore increases the optical transition rate. Moreover, if the right conditions are satisfied, a bound electron-hole pair can be formed. This neutral bound pair is called an exciton. In the simplest picture, the exciton may be conceived as a small hydrogenic system similar to a positronium atom with the electron and hole in a stable orbit around each other. Excitons are observed in many crystalline materials. There are two basic types of excitons, Wannier-Mott excitons (free excitons) and Frenkel excitons (tightly bound excitons). The free excitons are mainly observed in semiconductors, while the Frenkel excitons are found in insulator crystals and molecular crystals. Moreover, Wannier-Mott type excitons have a large radius that encompasses many atoms, and they are delocalized states that can move freely throughout the crystal; hence the alternative name of "free" excitons. In contrast, Frenkel excitons have a much smaller radius which is comparable to the size of the unit cell. This makes them localized states which are tightly bound to specific atoms or molecule; hence their alternative name of “tightly bound” excitons. Tightly bound excitons are much less mobile than free excitons, and they have to move through the crystal by hopping from one atom site to another **[49]**.

In a free exciton, the average separation of the electrons and holes is much greater than the atomic spacing, as shown in **Figure 1.2(a)**. This is effectively the definition of a Wannier exciton, and it specifies more accurately what is meant by saying that the free exciton is a weakly bound electron-hole pair. Since the electron-hole separation is so large, it is a good approximation to average over the detailed structure of the atoms in between the electron and hole and considers the particles to be moving in a uniform dielectric material. The energies of the bound states can be determined by finding the eigenvalues of the Schroedinger equation for the relative motion, or alternatively by using approximation techniques such as the variational method. Bound excitons are localized on the atom site at which they are created, as shown in **Figure 1.2(b)**. The excitons may therefore be considered as excited states of the individual atoms or molecules on which they are localized. They have very small radii and correspondingly large binding energies, with typical values ranging from about 0.1 eV to several eV. This means that Bound excitons are usually stable at room temperature. The excitons can propagate through the crystal by hopping from atom site to site in the same way that spin excitations propagate through crystals as magnon waves. The theoretical treatment of Bound excitons requires techniques more akin to atomic or molecular physics than solid state physics. The calculation of the exciton energies usually follows a tight binding approach, in order to emphasize the correspondence to the atomic or molecular states from which the excitons are derived. The calculation is further complicated by the fact that the coupling between the excitons and the crystal lattice is usually very strong. This leads to ‘self-trapping’ effects, in which the exciton produces a local distortion of the lattice, which then causes further localization of the exciton wave functions.

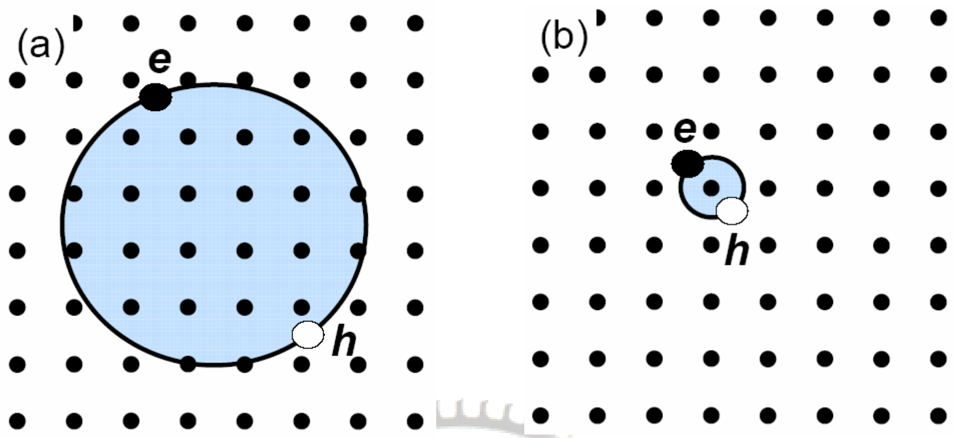

Figure 1.2: Schematic diagram of (a) Wannier-Mott excitons and (b) Frenkel excitons.

(ii) Free and Bound excitons in ZnO

The wurtzite ZnO conduction band is mainly constructed from the *s*-like state having Γ^7_c symmetry, whereas the valence band is a *p*-like state, which is split into three bands due to the influence of crystal-field and spin-orbit interactions **[50]**. The near-band-gap intrinsic absorption and emission spectrum is therefore dominated by transition from these three valence bands. The related free-exciton transitions from the conduction band to these three valence bands or vice versa are usually denoted by the heavy hole, light hole, and crystal-field split band.

Bound excitons are extrinsic transitions and are related to dopants or defects, which usually create discrete electronic states in the band gap, and therefore influence both optical absorption and emission processes. The electronic states of the bound excitons depend strongly on the semiconductor material, in particular, the band structure. From above statement, excitons could be bound to neutral or charged donors and acceptors. A basic assumption in the description of the bound exciton states for neutral donors and acceptors is a dominant coupling of the like particles in the bound-exciton states. These two classes of bound excitons are by far the most important cases for direct band-gap materials. In high-quality bulk ZnO substrates, the neutral shallow neutral-donor bound exciton (DBE) often dominates because of the presence of donors due to doped impurities and/or shallow donor-like defects. In samples containing acceptors, the acceptor-bound excitons (ABE) is observed. The recombination of bound excitons typically gives rise to sharp lines with a photon energy characteristic to each defect. Many sharp donor and acceptor bound-exciton lines were reported in a narrow energy range from 3.348 to 3.374 eV in ZnO. However, the chemical origin and binding energy of the most underlying donor and acceptor atoms remain unclear.

(iii) Two-electron satellites and Stimulated emission in ZnO

Another characteristic of the neutral-donor-boundexciton transition is the two-electron satellite transition in the spectral region of 3.32–3.34 eV. These transitions involve radiative recombination of an exciton bound to a neutral donor, leaving the donor in the excited state, thereby leading to a transition energy which is less than the DBE energy by an amount equal to the energy difference between the first excited and ground states of the donor. In the effective-mass approximation, the energy difference between the ground-state neutral donor-bound excitons and their excited states can be used to determine the donor binding energies **[51]** and catalog the different species present in the material.

Even though *n*- and *p*-type dopings have been reported in ZnO thin-films, **[52]** there is no demonstration of electrically pumped lasing in ZnO-based structures. However, optically pumped stimulated emission has been observed by many researchers from ZnO epitaxial layers grown by a variety of methods. Fabrication of low-dimensional structures such as quantum wells and dots has been the focus of semiconductor laser research to decrease the threshold for lasing. Efficient stimulated emission may be obtained from these quantum structures since the transfer integral at the band edge is larger than that of the bulk semiconductor. Excitonic emission may also be used to obtain efficient lasing, which may be realized for ZnO due to its larger exciton binding energy (60 meV) **[53]** compared to other wide band-gap semiconductors. Exciton-exciton scattering-induced stimulated emission is very important for the realization of low-threshold lasers since it occurs at a threshold lower than that for the electron-hole plasma (EHP) recombination. The demonstration of stimulated emission with excitonic origin paves the way for the realization of blue-violet laser diodes based on ZnO.

1.2.4 Defects in ZnO

As in any semiconductor, point defects affect the electrical and optical properties of ZnO as well. Kohan *et al.* and Van de Walle **[54,55]** recently calculated formation energies and electronic structure of native point defects and hydrogen in ZnO by using the first-principles, plane-wave pseudopotential technique together with the supercell approach. It can be concluded that, depending on the partial pressure of Zn, the two most common defects in ZnO are likely to be oxygen and zinc vacancies. In particular, oxygen vacancies (V_O) have lower formation energy than the zinc interstitials (Zn_i) and hence should be more abundant in Zn-rich conditions. In O-rich conditions, zinc vacancies (V_{Zn}) should dominate. **Figure 1.3** shows the various structure of native defects in ZnO crystal. As for the electronic structure of the main point defects in ZnO, the oxygen vacancy has been identified as a negative-U defect, since with increasing Fermi level a transition occurs from the +2 to the neutral state. Zinc vacancy is expected to have charge -2 in *n*-type ZnO where its formation is more favorable. The transition level between the -1 and -2 charge states of V_{Zn} occurs at 0.8 eV above the valence band. Thus, we may expect transitions from the conduction band or a shallow donor to the V_{Zn} acceptor at around 2.6 eV in *n*-type ZnO. Thus, the broad green luminescence commonly observed in *n*-type ZnO can be attributed to V_{Zn} **[54]**. The 2+ /0 level of the oxygen vacancy is predicted at about 2.7 eV above the valence band **[55]**. Since the positive charge state of V_{O} is unstable in ZnO, an electron paramagnetic resonance signal associated with this defect is not expected to be observable, at least in thermodynamically stable conditions.

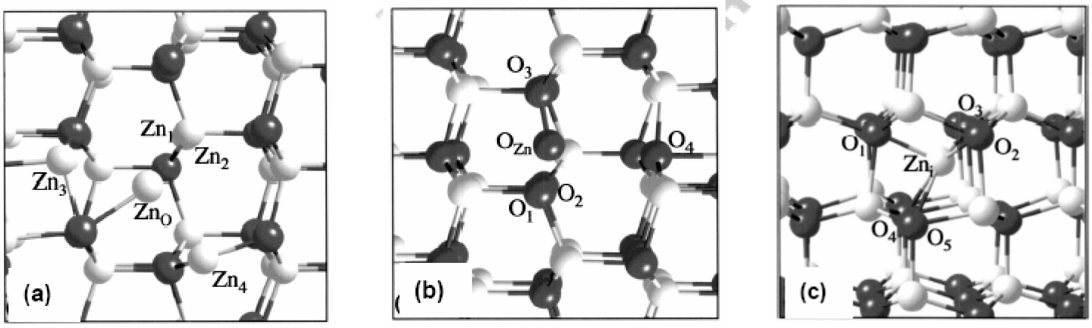

Figure 1.3: Structures of fully relaxed (a) Zn_o and , (b) O_{Zn} antisite, and (c) Zn_i point defects. (The dark balls indicate O atoms, whereas the gray balls are Zn atoms) **[154]**

Besides strong and rich exciton-related emissions in the photon energy range of 3.25–3.4 eV, PL spectrum of undoped high-quality ZnO usually contains a sharp peak at about 3.22 eV followed by at least two LO-phonon replicas. This emission has been attributed to the donor-acceptor pair (DAP) transitions involving a shallow donor and a shallow acceptor **[56]**. This conclusion is based mostly on a characteristic transformation of the DAP emission lines to similar, but shifted, emission lines arising from transitions from the conduction band to the same shallow acceptor with increasing temperature. The nature of the Green Luminescence, appearing at about 2.5 eV in undoped ZnO, may be related to a native point defect such as V_{O} or V_{Zn}. A red luminescence band emerged at about 1.75 eV in the PL spectrum of undoped bulk ZnO. Doping ZnO with Li acceptor results in the yellow luminescence band with a peak at about 2.2 eV. In contrast to the Green Luminescence band, the yellow luminescence band decays very slowly after switching off the excitation source, and can be observed also in the thermal luminescence spectrum **[14]**.

1.3 Doped ZnO materials

ZnO has a strong potential for various short-wavelength optoelectronic device applications. In order to attain the potential offered by ZnO, both high-quality *n*- and *p*-type ZnO are indispensable. However, difficulty in bipolar carrier doping is a major obstacle as seen in other wide-band-gap semiconductors.

1.3.1 *N*-type doping

ZnO with a wurtzite structure is naturally an *n*-type semiconductor because of a deviation from stoichiometry due to the presence of intrinsic defects such as O vacancies and Zn interstitials. Undoped ZnO shows intrinsic *n*-type conductivity. The first-principles study suggested that none of the native defects show high concentration shallow donor characteristics **[54]**. *N*-type doping of ZnO is relatively easy compared to *p*-type doping. Group-III elements Al, Ga, and In as substitutional elements for Zn and group-VII elements Cl and I as substitutional elements for O can be used as *n*-type dopants **[57]**. Doping with Al, Ga, and In has been attempted by many groups, resulting in high-quality, highly conductive *n*-type ZnO films **[58-60]**.

1.3.2 *P*-type doping

As mentioned repeatedly it is very difficult to obtain *p*-type doping in wide-band-gap semiconductors, such as GaN and ZnSe. The difficulties can arise from a variety of causes. Dopants may be compensated by low-energy native defects, such as Zn_i or V_O. Low solubility of the dopant in the host material is also another possibility **[61,62]**. Deep impurity level can also be a source of doping problem, causing significant resistance to the formation of shallow acceptor level. In ZnO, most candidate *p*-type dopants introduce deep acceptor levels. Copper doping introduces an acceptor level with an energy 0.17 eV below the conduction band **[63]**. Silver behaves as an acceptor with a deep level 0.23 eV below the conduction band. Lithium introduces a deep acceptor, and induces ferroelectric behavior **[64,65]**. It appears that the most promising dopants for *p*-type materialare the group V elements, although theory suggests some difficulty in achieving shallow acceptor states **[66]**.

A number of theoretical studies have addressed the fundamental microscopic aspects of doping in wide-band-gap semiconductors. The majority of these studies have dealt with the manner in which dopant solubility **[67]** or native defects **[68,69]** such as vacancies, interstitials, and antisites interfere with doping. Recently, various substitutional impurities for ZnO were examined as *p*-type dopants by using the first-principles pseudopotential method **[70]**. *P*-type doping in ZnO may be possible by substituting either group-I elements for Zn sites or group-V elements for O sites. It was shown that group-I elements could be better *p*-type dopants than group-V elements in terms of shallowness of acceptor levels **[70]**. However, group-I elements tend to occupy the interstitial sites, in part mitigated by their small atomic radii, rather than substitutional sites, and therefore, act mainly as donors instead.425 Moreover, significantly larger bond length for Na and K than ideal Zn–O bond length (0.193 nm) induces lattice strain, increasingly forming native defects such as vacancies which compensate the very dopants. These are among the many causes leading to difficulties in attaining *p*-type doping in ZnO. A similar behavior is observed for group-V elements except for N. Both P and As also have significantly larger bond lengths and, therefore, are more likely to form antisites to avoid the lattice strain. The antisites, A_{Zn}, are donor like and provide yet another unwelcome possible mechanism for compensating acceptors. It then appears that perhaps the best candidate for *p*-type doping in ZnO is N because among the group-V impurities, N has the smallest ionization energy, it does not form the N_{Zn}, and the *AX* center of N is only metastable. **Figure 1.4** shows the possible sites of N bind on ZnO crystal structure.

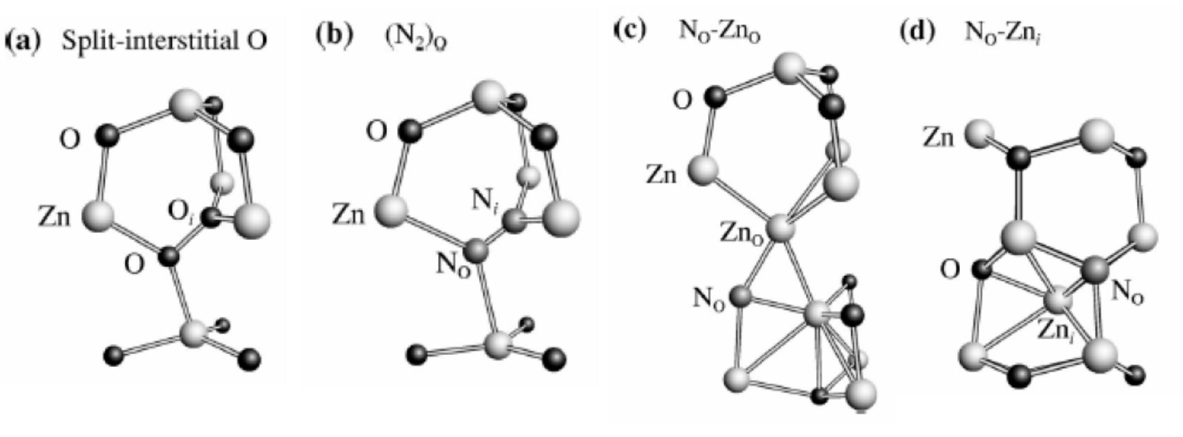

Figure 1.4: Atomic structures of the (a) split-interstitial-O*i* complex, (b) N2 molecule at an O site,(c) N-acceptor–Zn-antisite complex, and (d) N-acceptor–Zn-interstitial complex in ZnO **[155]**.

1.4 Nanoscience and nanostructures in ZnO materials

1.4.1 Nanoscience

Nanoscience is the study of atoms, molecules, and objects whose size is on the nanometer scale (1 - 100 nanometers). Physics is different on the nanometer scale. Properties not seen on a macroscopic scale now become important such as quantum mechanical and thermodynamic properties. Rather than working with bulk materials, one works with individual atoms and molecules. By learning about the properties of an individual molecule, scientists put them together in very well-defined ways to produce new materials with new and amazing characteristics.

The prospect of changing the big world by working in the nanoworld was first proposed by ***Richard Feynman*** back in 1959. Nanoscience involves working with objects on an extremely small scale. Recent developments in technology are only now allowing scientists to understand what is happening down at this level. While we can't literally see the atomic landscapes of molecules, we can model their composition and structure by using a variety of techniques such as X-ray crystallography, nuclear magnetic resonance spectroscopy and scanning probe microscopy. By controlling the mode in which nanometer scale molecular structures are formed, it is possible to control the fundamental properties of the materials these molecules build properties such as color, electrical conductivity, melting temperature, hardness, and strength.

The physical and chemical properties change because we opened up and exposed more surface area of the material. When particle sizes are reduced to the nanoscale, the ratio of surface area to volume increases dramatically. Since many important chemical reactions occur at surfaces, it is not too surprising that very small particles are staggeringly reactive.

1.4.2 Nanostructures in ZnO

The ZnO nanostructures presented here include nanorods, nanobelts, nanocombs, nanocages, nanotubes and nanorings. Recently, many research groups developed several methods for growing ZnO nanostructures, such as, vapor transport process, electrodeposition, sol-gel, polymer assisted growth, and aqueous chemical growth (ACG) technique. The most usual method to synthesize ZnO nanostructures used a vapor transport and ACG process **[71]**. Aligned growth of ZnO nanorods has been successfully achieved on a solid substrate via the VLS process with the use of catalysts and ACG process, which initiate and guide the growth **[72]**, as shown in **Figure 1.5 and 1.6.** There were also other techniques employed for the growth of vertically aligned ZnO nanorods which did not use any catalyst **[73]**. The vapor-liquid-solid (VLS) crystal growth mechanism was first proposed by Wagner and Ellis **[74]** in 1964 for Si whisker growth, in which Si whiskers with diameters of up to the micrometer scale were grown by hydrogen reduction of $SiCl_4$ with the presence of Au, Pt, Ag, Pd, Cu and Ni as the catalysts. In addition, Nanobelts are nanowires that have a well-defined geometrical shape and side surfaces. Nanobelts of ZnO are usually grown **[75]** by sublimation of ZnO powder without introducing a catalyst. **Figure 1.7** shows a TEM image of ZnO nanobelts, displaying different morphologies from the nanowires and nanorods. Each nanobelt has a uniform width along its entire length and the typical widths of the nanobelts are in the range of 50 to 300 nm and thicknesses are 10 to 30 nm. No particle was observed at the ends of the nanobelts. A ripple-like contrast that appeared in the TEM image is due to strain resulting from the bending of the belt. The nanobelt grows along [01-10], with top and bottom flat surfaces ±(2-1-10) and side surfaces ±(0001).

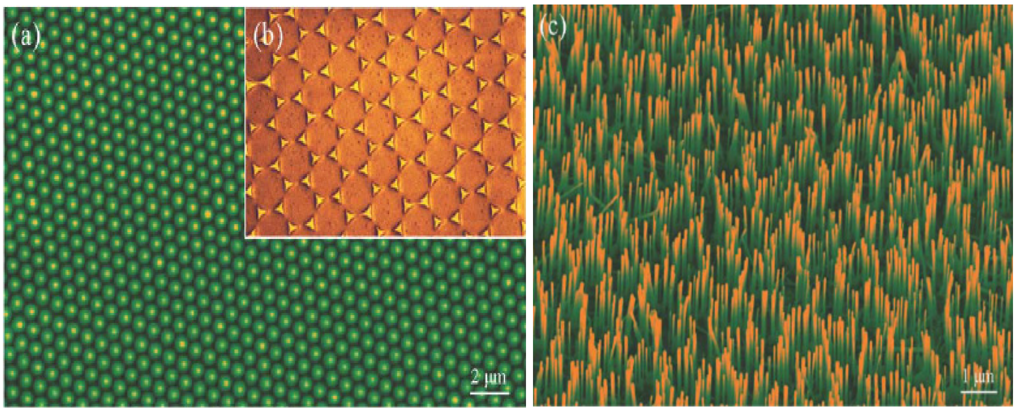

Figure 1.5: Growth of patterned and aligned ZnO nanowires. (a) Self-assembled monolayer of polystyrene spheres that serves as a mask. (b) Hexagonally patterned Au catalyst on the substrate. (c) Aligned ZnO nanowires grown on a single-crystal alumina substrate in a honeycomb pattern defined by the catalyst mask.**[72]**

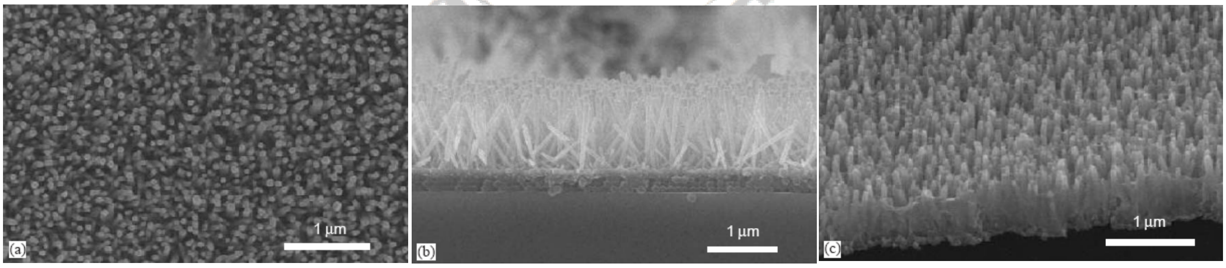

Figure 1.6: SEM images of large arrays of oriented ZnO nanorods grown on polystyrene (PS)/polycarbonate (PC) substrates for 8 h. (a) Low magnification, face-on view. (b) Cross-sectional SEM image of ZnO nanorods grown on PS/PC substrates. (c) SEM image of ZnO nanorods grown on PS/PC substrates after removingthe PS beads.

Recently, some scientists have discovered a novel nanostructure named “nanocage” or polygon prismatic nanocrystals **[76,77]**. In the temperature zone of 300-500 ^{o}C that we are interested in, balls and polyhedral are observed; some of them are dispersed on the substrate and there appears to be no correlation among them, as shown in **Figure 1.8**. The polyhedron is enclosed by (0001) (top and bottom surface), {10-10} (side surfaces), stepped {10-11} (inclined surfaces) and high index planes with rough surfaces. Some truncated hexagon based drums show open corners. In some cases, one side of the shell collapses possibly due to the high growth temperature as well as the small shell thickness. A common feature is that the shell exhibits mesoporous structure. Although the polyhedral shell structure appears to be composed of nanocrystals, transmission electron diffraction and imaging indicates that they have a ‘single-crystalline’ textured orientation and the side surfaces are {10-10}.

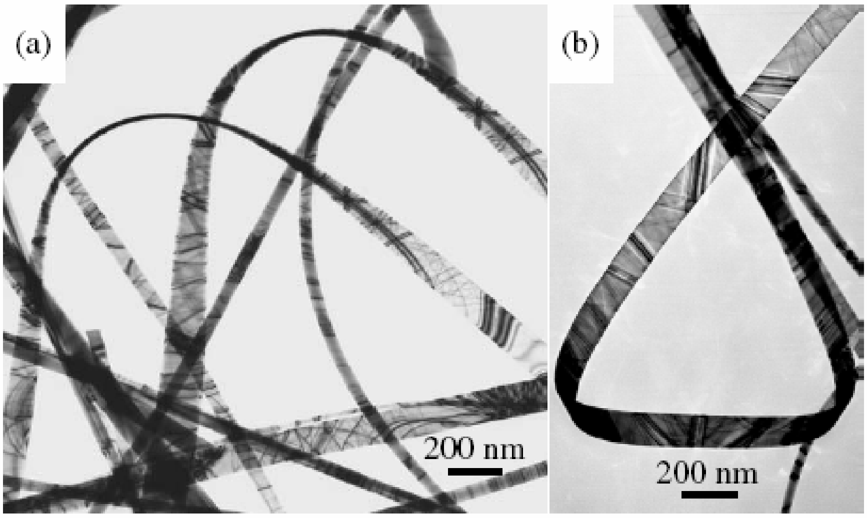

Figure 1.7: TEM images of the as-synthesized ZnO nanobelts, showing uniform morphology **[75]**.

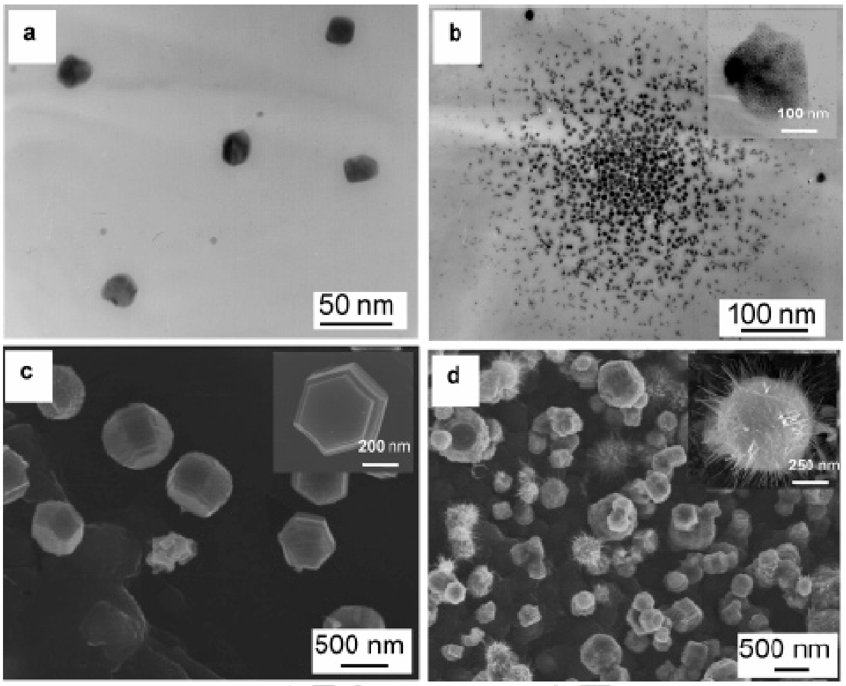

Figure 1.8: Morphology development of polygon prismatic compact Zn crystals as a function of growth time at 300 °C in an Ar atmosphere. (a) TEM image of polygon prismatic Zn nanoparticles (<30 nm) formed by the thermal vapor process in the initial growth stage. (b) Polygon prismatic Zn clusters are attracted together in 0.5 h and arranged into a polygonbased shape (inset). Also shown is the morphology of polygon prismatic Zn crystals in (c) 2 h and (d) 4 h. **[77]**

Chapter 2

Theory and Experiment

2.1 Theory

2.1.1 Theoretical concepts of nanomaterials

The goal is to develop a strategy to reach the rational design of nanomaterials with modeled and controlled particles size, morphology, orientation, and crystal structure. And then we could fabricate functional nanomaterials, to probe, tune, and optimize their physical and chemical properties. In our view, to achieve such ambitious challenge, the most pertinent parameter to monitor is the interfacial free energy of the system.

The main idea is to tune the thermodynamics and kinetics of nucleation, growth, and ageing of a system by controlling experimentally its interfacial tension **[78]**. For instance, the ability to segregate the nucleation and the growth stage enables to control the monodispersion of nanoparticles. Indeed, performing an aqueous precipitation far from the typical point of zero charge of the investigated metal oxide allows an enhanced control of the nucleation, growth, and ageing processes. According to the acid-base properties of metal oxide surfaces, increasing (or decreasing) the pH of precipitation/dispersion from the point of zero charge will increase the surface charge density by adsorption of hydroxyl ions. Consequently, the chemical composition of the interface and the interfacial tension of the system will be changed. In addition, a high ionic strength will contribute to a further increase of the surface charge density. This is understood by considering the electrostatic forces at the interface; indeed by increasing the ionic strength of the medium, a more effective screening effect of the interfacial charged sites will allow further surface sites to develop a charge. In such case, the surface charge may therefore reach its maximum charge density, which ultimately depends on the oxygen structure and composition of the interface. At maximum charge density, the interfacial tension of the system will reach a minimum. Thermodynamic colloidal stability may thus be reached resulting in a considerable lowering of the secondary ageing processes, henceforth preventing the nanoparticle size to increase as well as avoiding crystal phase transformations. Any adsorption phenomenon at interface decreases the surface (or interfacial) tension γ.

Moreover, the nanoparticles will evolve in solution, that is, their size will increase with time, and their crystal structure may be subjected to phase transformations. This is the unstable region of the precipitation. [Note: The *stable* region, the nanoparticles are thermodynamically stabilized, and consequently secondary growth phenomenon such as Ostwald ripening does not occur.] No longer submitted to ageing, the nanoparticle size is finite and is directly related to the precipitation conditions such as pH and ionic strength at a given temperature and precursor concentration. By consideration of the nucleation and growth processes which rule the generation of solid phases from solutions, a maximum is found for the first derivative of the free enthalpy of nucleation with respect to the number of precursors (which essentially represents the particle size). Therefore, reducing the interfacial tension leads to an important lowering of the nucleation energy barrier, which in turn leads to the decrease of the nanoparticle size. A large stage of nucleation of very small particle accompanied by a very short stage of growth is predicted. As a result, the average nanoparticle size is expected to decrease substantially.

As the thermodynamic stabilization is achieved, not only the size is tailored but also the shape as well as the crystallographic structure may be controlled. For example, at low interfacial tension, the shape of nanoparticles does not necessarily require being spherical; indeed very often nanoparticles develop a spherical morphology to minimize their surface energy because the sphere represents the smallest surface for a given volume. However, if the synthesis and dispersion conditions are suitable, the shape of the crystallites will be driven by the symmetry of the crystal structure as well as by the chemical environment, and various morphologies may therefore be developed. Manipulating and controlling the interfacial tension enables to grow nanoparticles with sizes and shapes tailored for their applications. Additionally, particle size and shape control, the precipitation of nanoparticles at low interfacial tension allows the stabilization of oxide and oxyhydroxide metastable crystal structures. Crystal phase transitions in solution generally operate through a dissolution re-crystallisation process to comply with the surface energy minimization requirement of the system. Indeed, when a solid offers several allotropic phases and polymorphs, it is typically the one with the highest solubility and consequently the lowest stability, which precipitates first. This is understood by considering the nucleation kinetics of the solids. At a given super-saturation ratio, the germ size is as small (and the nucleation rate as high) as the interfacial tension of the system is low. Thus, given that the solubility is inversely proportional to the interfacial tension, the precipitation of the most soluble phase and consequently the less stable thermodynamically, is therefore kinetically promoted.

2.1.2 Theoretical concepts of photoluminescence

(i) Excitation and relaxation

The band diagram corresponding to the photoluminescence process in a direct gap material is given in **Figure 2.1(a).** Photons are absorbed from an excitation source such as a laser or lamp, and this injects electrons into the conduction band and holes into the valence band. This will be possible if the frequency ν_L of the source is chosen so that $\mathbf{h}\nu_L$ is greater than E_g.

It is apparent from **Figure 2.1(a)** that the electrons are initially created in states high up in the conduction band. The electrons do not remain in these initial states for very long, because they can lose their energy very rapidly by emitting phonons. This process is indicated by the cascade of transitions within the conduction band shown in **Figure 2.1(a).** Each step corresponds to the emission of a phonon with the correct energy and momentum to satisfy the conservation laws. The electron-phonon coupling in most solids is very strong and these scattering events take place on time scales as short as 100 fs (10^{-13}s). This is much faster than the radiative lifetimes which are in the nanosecond range, and the electrons are therefore able to relax to the bottom of the conduction band long before they have had time to emit photons. The same conditions apply to the relaxation of the holes in the valence band. After the electrons and hole have relaxed as far as they can by phonon emission, they must wait at the bottom of the bands until they can emit a photon or recombine non-radiatively. This leaves time to form thermal distributions, as sketched in **Figure 2.2(b)**, and the shading indicates the occupancy of the available states. These occupancy factors can be calculated by applying statistical physics to the electron and hole distributions.

(ii) Photoluminescence spectroscopy

Photoluminescence spectroscopy is mainly used as a diagnostic and development tool in semiconductor research. The usual goal is to develop electroluminescent devices such as light-emitting diodes and lasers. This is usually only achieved after the emission mechanisms have been studied in detail using photoluminescence spectroscopy. Photoluminescence spectra can be recorded with an experimental arrangement such as the one shown in **Figure 2.2.** The sample is mounted in a variable temperature cryostat and is illuminated with a laser or bright lamp with photon energy greater than $\boldsymbol{E_g}$. If a liquid helium cryostat is used, sample temperatures from 2 K upwards are easily obtained. The luminescence is emitted at lower frequencies and in all directions. A portion is collected with a lens and focused onto the entrance slit of a spectrometer. The spectrum is recorded by scanning the spectrometer and measuring the intensity at each wavelength with a sensitive detector such as a photomultiplier tube. Alternatively, the whole spectrum is recorded at once using an array of detectors such as a charge coupled device (CCD).

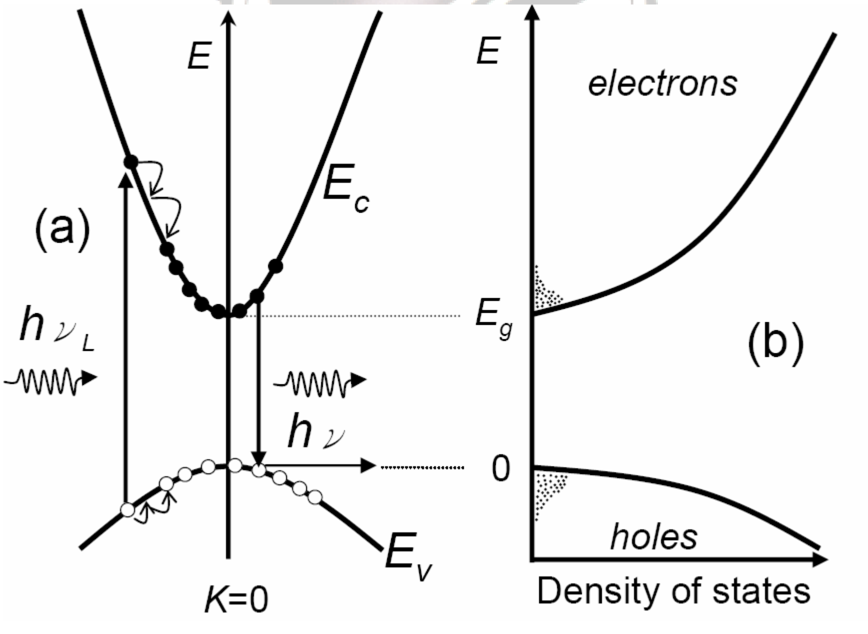

Figure 2.1: (a) Schematic diagram of the processes occurring during photoluminescence in a direct gap semiconductor after excitation at frequency. (b) Density of states and level occupancies for the electrons and holes after optical excitation.

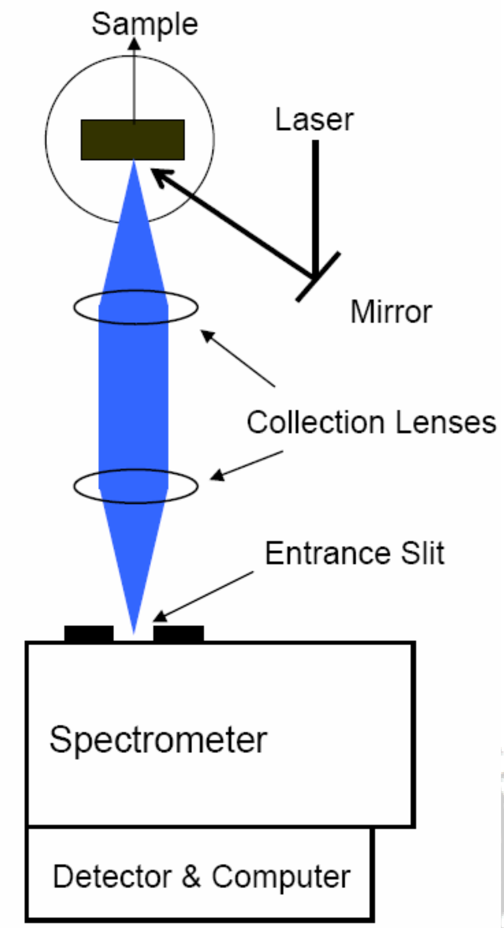

Figure 2.2: Experimental arrangement used for the observation of photoluminescence spectra.

2.2 Material fabrication

2.2.1 ZnO thin films formation

The ZnO thin films (~100 nm) were deposited on 4 inch diameter Si (001) substrates buffered with SiO_2 and Si_3N_4 and without inter-layers by radio-frequency (RF) magnetron sputtering using 99.99% ZnO as the target. The growth chamber was evacuated by a turbo pump and mechanical pump. The gas mole ratio of oxygen to argon (OMR) was varied in the range of 0-72%. Silicon substrates were cleaned by usual semiconductor technology before loading into the chamber. Sputtering conditions were optimized at a substrate temperature of 50˚C, RF power of 50W, sputtering pressure of 10mTorr and sputtering time of 30-40 minutes. The buffer layers (inter-layers) were grown by electron evaporation and the thickness of the buffer layers for Si_3N_4 and SiO_2 was measured to be about 10-40 nm, respectively. After sputtering, the as-grown films were cut into several pieces and then annealed at 500, 850 and 1000^oC for 20-40 minutes under pure oxygen and nitrogen atmospheres.

2.2.2 Ions implantation in ZnO films

Ion implantation is a precise method of introducing dopants into a semiconductor and can also be used to create high resistance regions for inter-device isolation. The residual implant damage remaining after annealing appears to have donor-like character. To minimize this damage, it may be necessary to adopt techniques used for other compound semiconductors, such as elevated temperatures during the implant step to take advantage of so-called dynamic annealing in which vacancies and interstitials created by the nuclear stopping process are annihilated before they can form stable complexes.

The ZnO films were subsequently subjected to phosphor and nitrogen implantation at room temperature. The phosphor and nitrogen ions with energy of 120 and 80 KeV were injected into the as-grown ZnO films, respectively. The fluences range was from 5×10^{12} -5×10^{15} cm^{-2}. Based on Rutherford back scattering measurement followed by (the transport of ions in matter) TRIM simulations, the implanted ions distribution in ZnO films forms a nearly perfect Gaussian shape with the peak position at (80±10) nm below the surface. After ions implantation, the specimens were annealed at 850˚C and 1000˚C for 20 minutes under pure oxygen and nitrogen atmospheres.

2.2.3 Soft chemical growth and treatment on ZnO nanorods

The ZnO-coated silicon substrates were placed in a solution containing an equimolar (0.01-0.1M) aqueous solution of $Zn(NO_3)_2.6H_2O$ and Hexamethylenetetramine (HMT) and reacted at 75-95^{o}C for 10-24 h. After that, the substrates were removed from the aqueous solutions, rinsed with distilled water, and dried at room temperature overnight. Finally, high quality one-dimensional ZnO nanostructures were developed.

The ZnO nanorods were exposed to various plasma atmospheres (nitrogen, oxygen, ammonia, and hydrogen) for 30, 60, 120, 300, and 900 sec by inductively coupled plasma (ICP) system. For the plasma treatment, the substrate temperature, total gas pressure, ICP top power, and bottom power were maintained at different conditions such as **Table 2.1**.

Table 2.1: Conditions of plasma treatment on ZnO nanorods.

Insert Gas	RF / ICP power (W)	Working Pressure (mTorr)	Working Temperature (^{o}C)	Treatment period (sec)
NH_3	50/250	300	300	30,60,90,180,900
H_2	50/600	400	100	30,60,120,300,900
N_2	50/300	300	200	30,60,120,300,900
O_2	50/250	250	150	30,60,120,300,900

2.2.4 Fabrication of one-dimensional nanotube composite device

Figure 2.3 shows the optical microscopy bright-field images of electrode structure made by the electron-beam lithography process. In **Figure 2.3 (a)**, the 16 large electrode pads are used for wire bonding, connecting to the outside part circuit. In the central part shown in **Figure 2.3 (b)**, several tiny electrode arrays intended to contact nanotubes (or nanowires) are shown. Thin Cr layer (1 nm) is used to enhance the reliable contact and adhesion between the contact metal and SiO_2. As we zoomed in **Figure 2.3(b)**, there are four squares in the corners, which are used as alignment markers (**Figure 2.3 (c)**). For electrical transport measurement, device configuration is shown in **Figure 2.4**. The nanotube (or nanowire) is embedded in metal electrodes (AuPd alloy) to enhance the electrical coupling between nanotube and electrode. To achieve this aim, predefined coordinate markers are needed to calculate the exact position of selected nanotubes relative to the neighboring coordinate markers. The tolerance shift in our alignment technique is well controlled within around 50 nm. The main advantages of this contact method are to decrease the contact resistance and make possible contact patterns on complicated nanostructures.

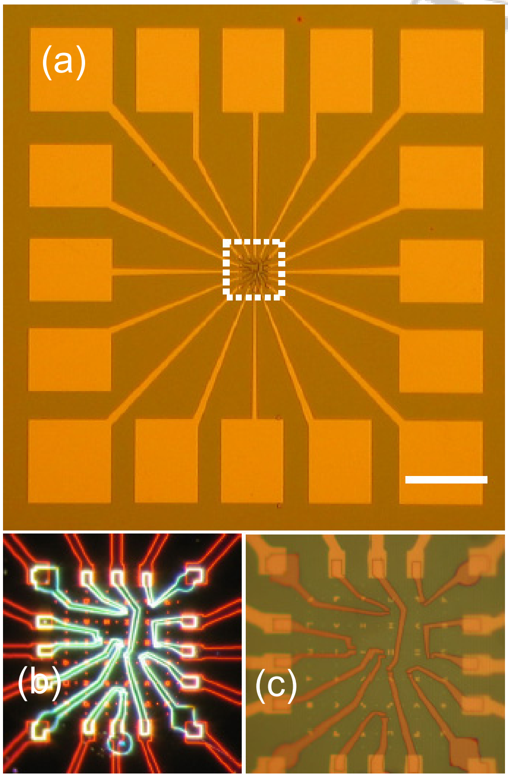

Figure 2.3: SEM images of electrode patterns for contacting nanotubes, (a) Large-scale view of pattern. (b) Dark-field image of central part of (a), (c) Bright-field image of (b). Scale bar is 200 μm.

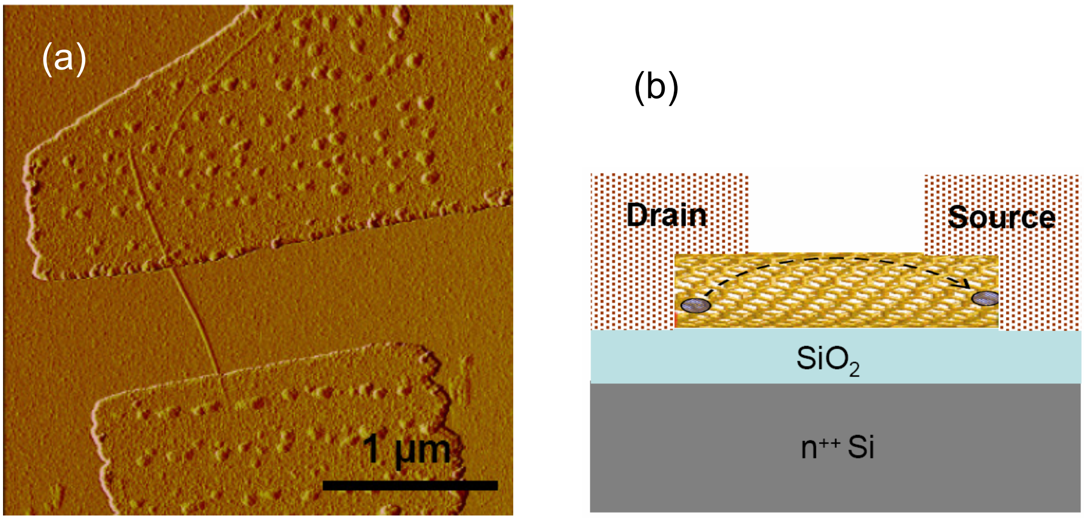

Figure 2.4: (a) AFM image of coated SWNT embedded in source and drain electrodes. (b) Schematic illustration of coated SWNT device.

2.3 Characterization of ZnO materials and electrical transport

The surface morphology of ZnO materials were observed by field emission scanning electron microscopy (FE-SEM). JEOL-6500 FE-SEM system was employed in this study. In order to prevent to damage our samples, we used low voltage (20KeV) to scan these serial images. The transmission electron microscopy (TEM; Philips TECNAI 20) with energy dispersive x-ray spectroscopy (EDS) operated at 200 keV was used for detail crystal analysis. The crystal structures of ZnO films and nanorods were investigated by x-ray diffraction (Siemens, D5000) using Cu Kα radiation and a nickel filter. When an x-ray beam strikes a crystal surface at some angle, a portion is scatted by the layer of atoms at the surface. For optical properties, photoluminescence measurement was performed by the excitation from 325 nm *He–Cd* laser at room temperature and 10 K. The chemical compositions were examined by x-ray photoelectron spectroscopys (XPS) after the samples were first sputtered for 90 s to remove the surface containment by Ar ion. Current-voltages (*I-V)* characteristics curve of the samples was measured by applying dc voltage to the device using a HP-4156 and each datum was averaged by measuring ten times. The electrical properties of the nitrogen-implanted ZnO films were investigated by van der Pauw method room temperature Hall measurements with nonsintered indium contacts and magnetic field of 0.315 T.

The precise electrical transport was measured by homemade transport system in Dr. Siegmar Roth's laboratory in Max-Planck Institute (Stuttgart, Germany). The main components of this system are a desktop computer equipped with a GPIB card and controlled by Labview software (written by Dr. Dirk Obergfell), two Keithely 2400 and one Keithely 230 (voltage source), and a preamplifier. The current is measured using the high sensitivity, low noise current preamplifier. The output voltage is amplified by a conversion factor μ and then read by Keithely 2000 (voltage meter). A RC low-pass filter with a time constant around 0.5 sec is added between gate and voltage source to prevent abrupt potential changes and allow consecutive potential modulation on the one-dimensional nanostructure. The voltage adder is designed to adjust the offset voltage from the preamplifier.

Chapter 3

Defects engineering on zinc oxide thin films

3.1 Introduction

It is well known that the ultraviolet (UV) emission of ZnO is attributed to exciton-related activities, but for the visible emissions, various mechanisms have been proposed including the involvement of zinc interstitials,**[79,80]** oxygen interstitials,**[81,82]** zinc vacancies**[83,84]** and oxygen vacancies.**[85,86]** In addition, it is known that the sintered ZnO is a nonstoichiometric oxide at room temperature, exhibiting an *n*-type electrical conductivity due to an excess of the zinc. The zinc excess gives origin to intrinsic donors in ZnO, which can be assigned either to the zinc interstitials (Frenkel defect) **[87]** or to the oxygen vacancies (Schottky defect) **[88]**. These two types of point defects have similar electrical properties, being difficult to distinguish between them. However, both point defects exhibit different defect reactions under different annealing temperature and atmosphere. Recently, it has been revealed that the dominant point defect may vary with the annealing temperatures **[89]**. During different annealing conditions, the crystalline characteristics of ZnO films would be changed to exhibit various point defects that would affect the luminescent properties.

3.2 Defects transition in high-orientated ZnO thin films

To understand the relation between intrinsic defects and crystallization in ZnO thin films system, we used different manufacturing conditions to figure the defects mechanism out.

Figure 3.1 shows the x-ray diffraction patterns of ZnO films sputtered at the OMR of 0%, 5%, 20%, 50% and 72%, and then annealed at 850˚C in N_2 and O_2. atmospheres. Only a sharp (002) diffraction peak at 2θ~34.4˚ can be detected for both atmospheres. It indicates that a well-defined and oriented ZnO film has been obtained. However, with an increase of the OMR ratio, the intensity of ZnO (002) diffraction peak was reduced. This reveals that the crystallinity of the ZnO films would be hindered at a high oxygen pressure. As shown in **Figure 3.1**, although the film crystallinity is not sensitive to the annealing atmosphere, the values (0.22˚, 0.18˚, 0.25˚, 0.28˚ and 0.5˚) of full-width at half maximum (FWHM) for ZnO (002) diffraction peak change with the OMR ratios of 0%, 5%, 20%, 50% and 72%, respectively. The best sputtered ZnO film appears at the OMR of 5% that is probably related to the relative ratio of Zn to ZnO as reported by Fujimura et al.**[90]** Therefore, the optimum sputtering atmosphere with the OMR of 5% will be used in this work to study the effect of annealing temperature on the film crystallinity unless otherwise noted.

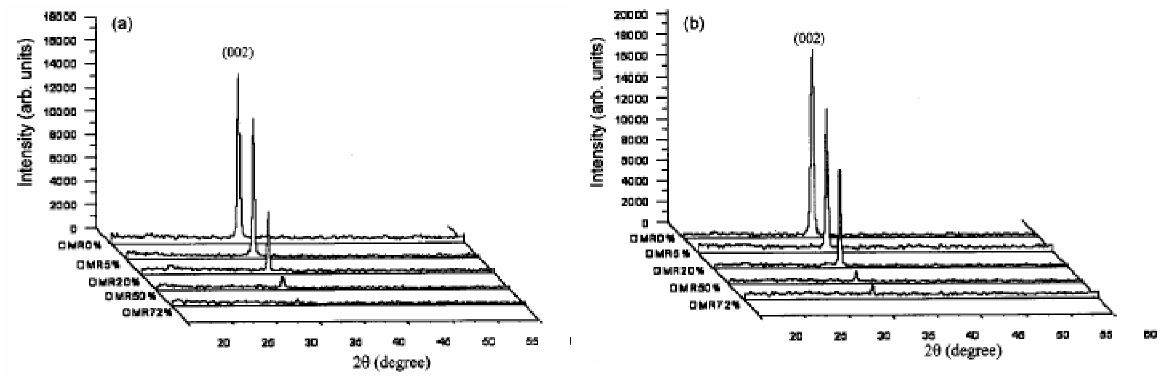

Figure 3.1: XRD patterns of ZnO films as function of OMR conditions after annealing at 850˚C in (a) nitrogen and (b) oxygen atmospheres.

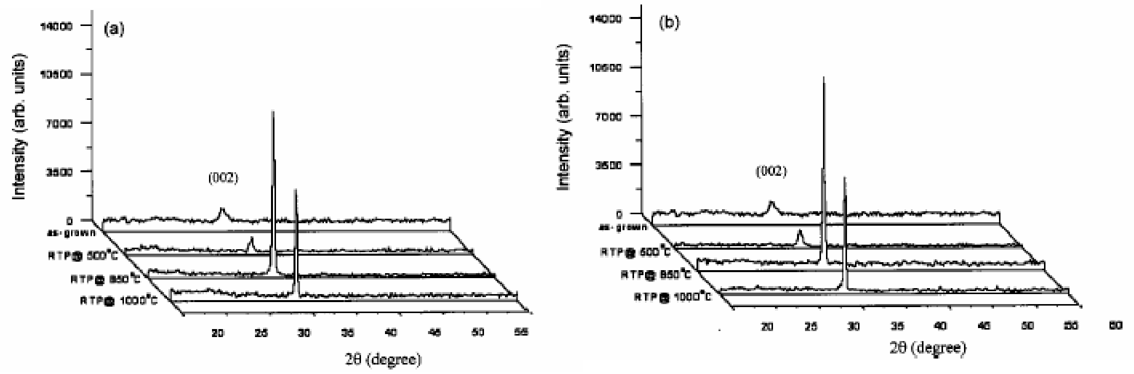

Figure 3.2: XRD patterns of ZnO films sputtered at OMR 5% and annealed at different temperatures in (a) nitrogen and (b) oxygen atmospheres.

Figure 3.2 illustrates that the intensity of the (002) diffraction peak varies with annealing temperature. When the sputtered ZnO films are annealed below 850˚C, it was found that (002) peak intensity increases with annealing temperature up to 850˚C in both N_2 and O_2 atmospheres because of the enhanced film crystallite and grain size. Above that (850˚C), it decreases. The smallest FWHM value in the ZnO films can be obtained at 850˚C. This indicates that although a higher annealing temperature can improve the crystallization of the as-grown ZnO films, as the annealing temperature exceeds 850˚C, especially above 1000˚C, the crystallinity of ZnO films may be deteriorated by either crystalline lattice defects **[91]** or thermal microstrain due to structure distortion. Therefore, the surface structure and grain morphology in ZnO films will be further modified as illustrated in **Figure 3.3**, where pill-like structure was formed. The formation of the pill-like structure may be related to the surface free energy and crystalline lattice defects because a large number of zinc element will be vaporized from the ZnO films at such a high annealing temperature. Therefore, in this condition, more point defects would be produced in the ZnO films. For the wide-gap semiconductors, PL emission is one of the most important properties of ZnO. **Figure**

3.4 shows the room-temperature PL spectra of the as-grown ZnO films sputtered at various OMR conditions. The peak intensity of the deep-level emission around ~600 nm changes with the OMR ratio and the weakest one appears at the OMR of 20%. It can be considered that some of point defects such as oxygen vacancies and zinc interstitials are compensated each other at a certain oxygen pressure. Furthermore, as one can see, along with the decrease in deep-level emission peaks, the peak intensity of the UV emission at ~382 nm increases.

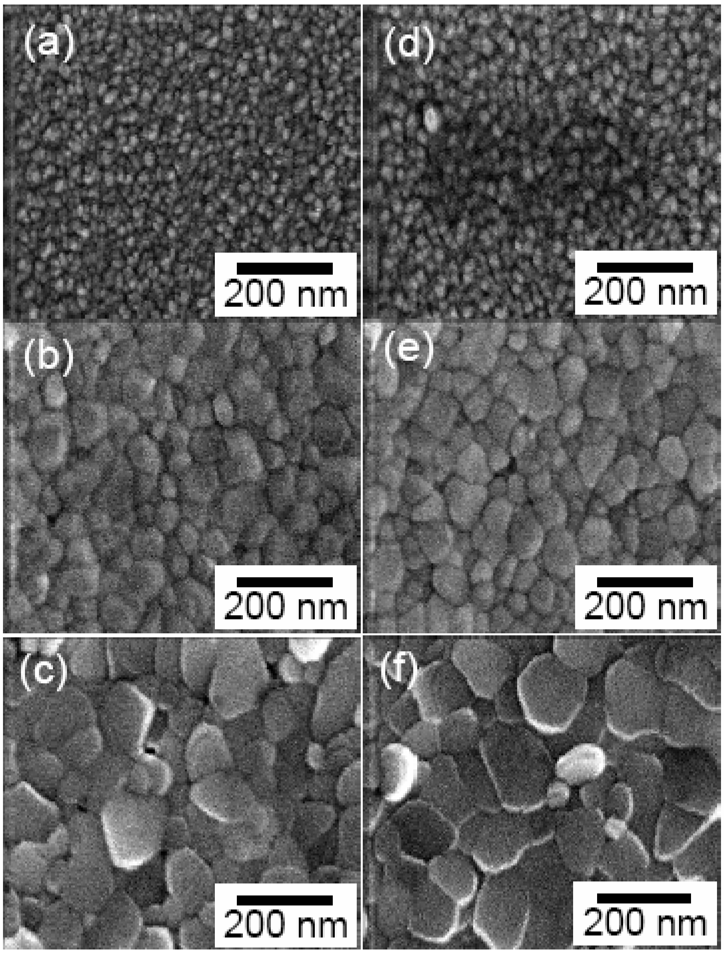

Figure 3.3: SEM surface morphology of OMR5%-treated ZnO films annealed various conditions: (a) 500˚C in N_2, (b) 850˚C in N_2, (c) 1000˚C in N_2, (d) 500˚C in O_2, (e) 850˚C in O_2, (f) 1000˚C in O_2.

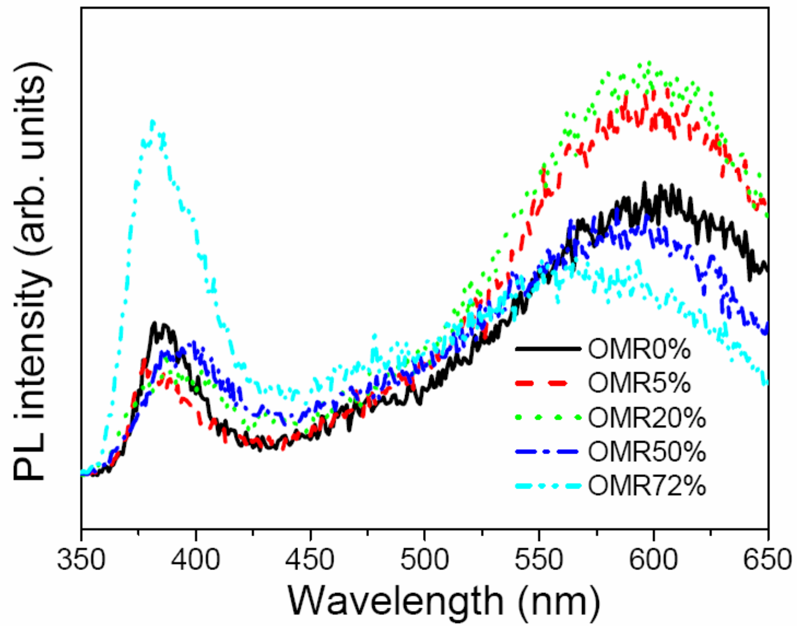

Figure 3.4: Room temperature PL spectra of the as-grown ZnO films at various OMR conditions.

Figure 3.5 shows the room-temperature PL spectra of the ZnO films sputtered at various OMR ratios and then annealed at 850˚C in N_2 and O_2 atmospheres. A strong PL emission peak corresponding to UV emission, in contrast to that of the as-grown films, appears around 378-382 nm that should be a near band edge emission of ZnO films due to an exciton-related activity.**[92]** As shown in **Figure 3.5(a)** for the films annealed in N_2 atmosphere, a very stronger UV peak and a relatively low deep-level emission (528 nm) shows up at the OMR of 5%. However, in this condition (annealed in N_2 atmosphere), as the ZnO film was sputtered at the OMR of 20%, the UV emission peak becomes weak and a broader deep-level emission appears around 533 nm as compared to that sputtered at other OMR ratios. On the other hand, as the sputtered ZnO films were annealed in O_2 atmosphere, **Figure 3.5(b)** shows that the UV peak not only becomes sharper at the OMR of 5% but also the deep-level emission at ~533 nm is almost barely detected at the OMR of 20%. This phenomenon reveals that the deep-level emission can be reduced by controlling the OMR ratio and annealing conditions. It is well known that ZnO films can display three major PL peaks, a UV (near-band-edge) emission peak, a green emission peak and a red emission peak. The green and red emissions are generally associated with zinc interstitials and oxygen vacancies in ZnO lattice. Several authors have reported that the green luminescence corresponds to a transition from $Zn^{\bullet}$ to $Zn^{\bullet\bullet}$ **[89]** but Riehl et al. attributed the green luminescence center to the oxygen vacancies ($Vo^{\bullet\bullet}$) **[93]**. However, in our work, it was found that the dominant defect varies with the annealing conditions. As annealed in nitrogen atmosphere, a deep-level emission peak around 2.06 eV was observed for both as-grown and 500˚C-annealed ZnO films as illustrated in the insert of **Figure 3.6**. With increasing annealing temperature, at 850˚C, the deep-level emission peak shifts to 2.35 eV, and then again decreases to 2.26 eV at 1000^{o}C. It indicates that the dominant point defects can be controlled by changing the annealing temperature. The temperature dependence of the predominant defect in ZnO films can be further elucidated as follows.

It is well known that the deep-level emission is influenced by the formation of point defects. In the case of ZnO, several reports suggested that the deep-level emission results from point defects such as the $Vo^{\bullet\bullet}$, $Zn_i^{\bullet\bullet}$, and $V_{Zn}^{''}$. For the as-grown ZnO films deposited by rf magnetron sputtering, the chemical component of ZnO films is usually nonstoichiometric with oxygen insufficient and Zn interstitials. However, in our case, the predominant point defects in the as-grown ZnO films is considered as the oxygen vacancies because the films were sputtered at the OMR of 5% (the chamber ambient is close to pure argon) and the energy level of 2.05 eV corresponds to the transition of oxygen vacancies**[89]**. For the samples annealed below 500˚C, a very weak emission was observed that was the same as the as-grown films because the structure characterization of ZnO film annealed below 500˚C is very similar to that of the as-grown one. Therefore, in this condition, the predominant point defects are still oxygen vacancies. However, with an increase of annealing temperature, some lattice and surface defects can be removed and the ZnO film may be rearranged into more perfect structure, indicating that the role of predominant point defects may be different.

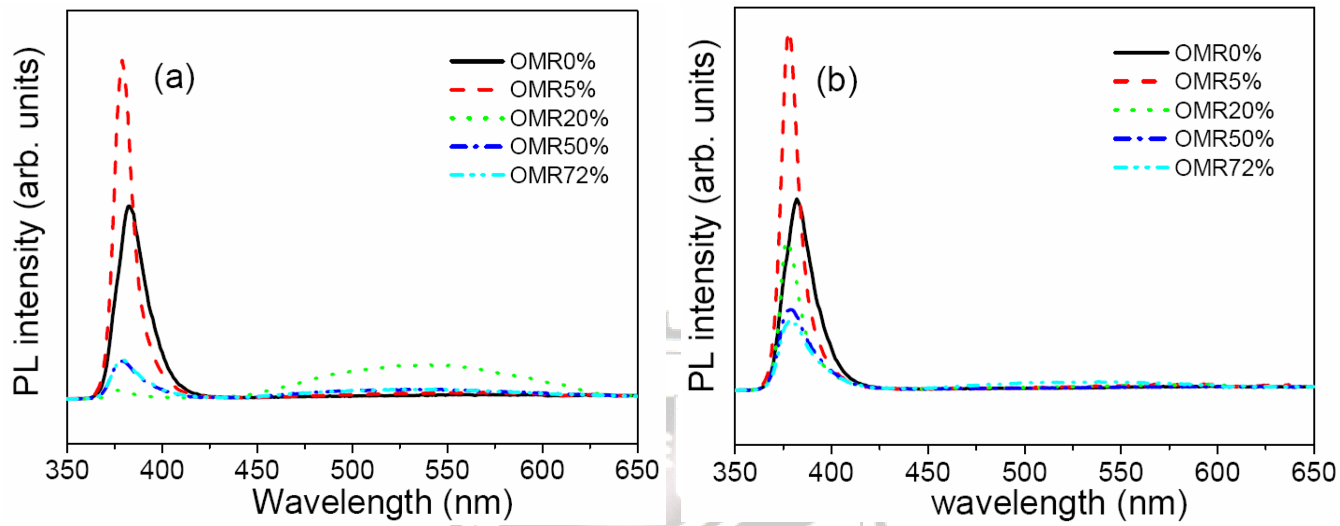

Figure 3.5: Room temperature PL spectra of ZnO films treated at different OMR conditions and annealed 850˚C in (a) N_2 and (b) O_2 atmospheres.

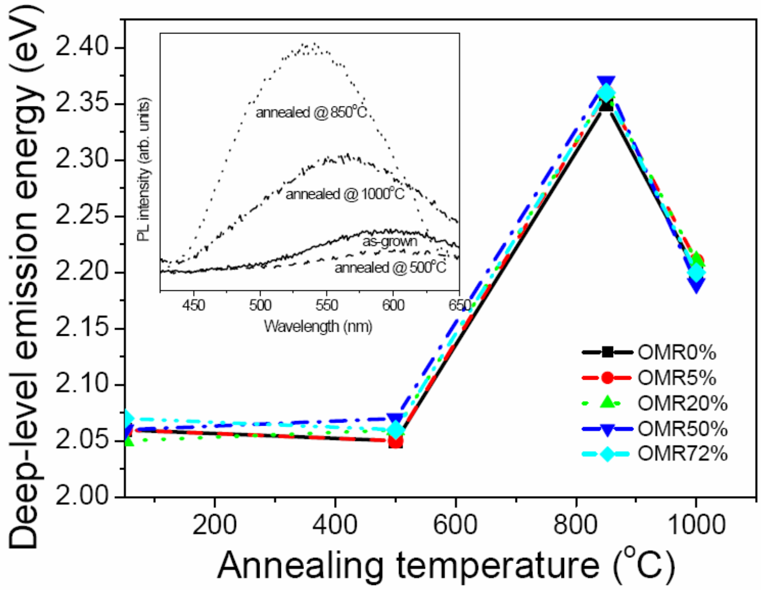

Figure 3.6: Defect transition of annealed ZnO films at various temperatures in N_2 atmosphere.

As the as-grown ZnO film was annealed at a high temperature in N_2 atmosphere, the nitrogen gas may be ionized as reported by Garces et al. and the nitrogen acceptor can be effectively formed in ZnO film by thermal annealing in N_2 atmosphere at temperatures range of 600-900°C**[94]**. If the nitrogen gas could be ionized and filled into the ZnO structure, the number of oxygen vacancies would be reduced. Furthermore, according to defect chemistry, the zinc interstitials come from the Frenkel reaction in the Zn sublattice, while the oxygen vacancy comes from the Schottky reaction and it is difficult to distinguish them experimentally. However, it was reported that the Frenkel defects predominate at lower temperatures during annealing treatment of ZnO and the Schottky defects becomes increasingly important at higher temperatures **[95]**. In other words, for the as-grown ZnO film prepared with an OMR of 5% and annealed at 850˚C in N_2 atmosphere, the zinc interstitials tend to form and become the predominant point defects. As evidenced from **Figure 3.6**, the deep-level emission at ~528 nm corresponds to 2.35 eV that is primarily characteristic of the dominance of zinc interstitials. However, when the films were annealed at a higher annealing temperature such as 1000˚C, a broader emission band appears around 560 nm and the deep-level emission peak shifts from 2.35 eV to 2.26 eV in comparison with that at 850°C. The role of dominant point defects becomes a little complication because a higher annealing temperature would induce the structure change and produce different types of point defects. According to the energy level, the dominant defect in the ZnO films is probable either oxygen vacancies or zinc interstitials depending on the competition with each other. To exactly determine the possible route of defects transition, the defect concentration in ZnO films can be calculated by comparing the relative PL intensity ratio of the UV emission to the deep-level emission. The PL intensity ratio changes with both OMR ratio and annealing temperatures. As illustrated in **Figure 3.7(a)** for the ZnO films annealed in

N_2 atmosphere, a maximum relative PL intensity ratio appears at 850˚C for the films sputtered at the OMR of 5%. The value of the relative PL ratio is more than 60, much larger than that obtained by MOCVD and MBE (~10) **[96]**. However, the relative PL value in other conditions is all below 15 except for the sample sputtered at the OMR of 0% and annealed at 850˚C. In contrast, the relative PL intensity ratio can be markedly enhanced by annealing in O_2 atmosphere as shown in **Figure 3.7(b)** because the formed oxygen vacancies in the ZnO films sputtered at a lower OMR can be further compensated in the oxygen annealing. Furthermore, the oxygen ions can combine with the zinc interstitials to form ZnO and thus, the deep-level emission can be depressed. Therefore, the defect concentration can be reduced and a sharp UV emission along with invisible deep-level peaks can be obtained for the films sputtered at the OMR of 5% and annealed at 850˚C in O_2 atmosphere. The relative PL intensity ratio of the UV emission to the deep-level emission can be improved up to 98, indicating that a high-quality ZnO film with lower defect concentration can be obtained in this work through the control of annealing treatment.

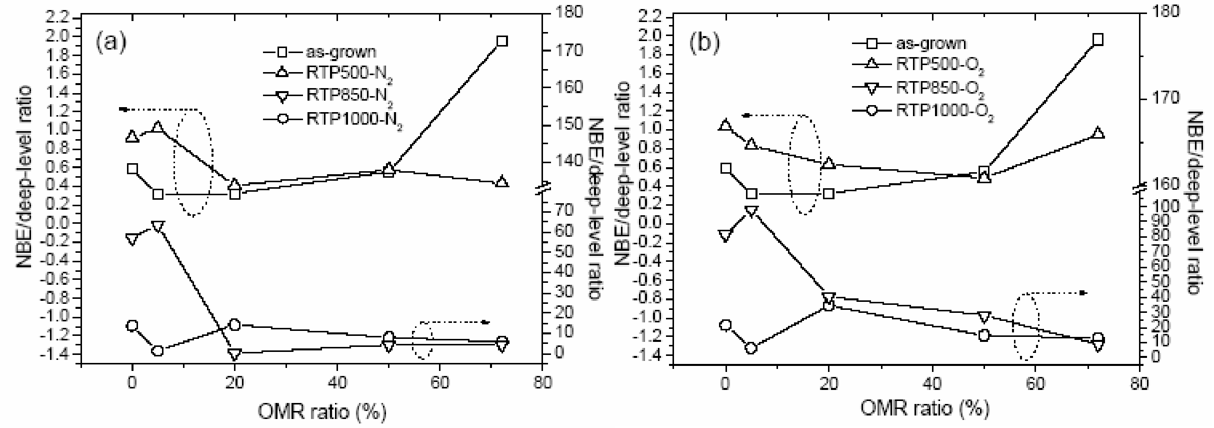

Figure 3.7: Relative PL intensity ratio of the UV emission to the deep-level emission for the ZnO films treated with various OMR conditions and annealed at different temperatures in (a) N_2 and (b) O_2 atmospheres.

3.3 Point defects controlled by buffer layers in ZnO thin films system

Recently, many studies have been focused on ZnO films deposited on silicon substrate because of the development for large-scale electronic integration device. However, a large lattice mismatch between Si and ZnO will affect the physical characteristics and emission properties of the ZnO films. Therefore, it is important to understand the substrate, especial interface microstructure, effect on defect transition and photoluminescence properties of ZnO films. **Figure 3.8** shows the X-ray diffraction patterns of ZnO films sputtered at Si, SiO_2/Si, and Si_3N_4/Si, and then annealed at 850˚C in O_2 atmosphere. Only a sharp diffraction peak of (002) at $2\theta = 34.5^\circ$ can be detected for all the films, indicating that well-defined and oriented ZnO films have been obtained. However, the peak intensity of ZnO film grown on SiO_2/Si substrate is much weaker compared with that on Si_3N_4/Si substrate. This reveals that the amorphous SiO_2 buffer layer has a strong negative affect on the crystalline characteristics of the ZnO films.

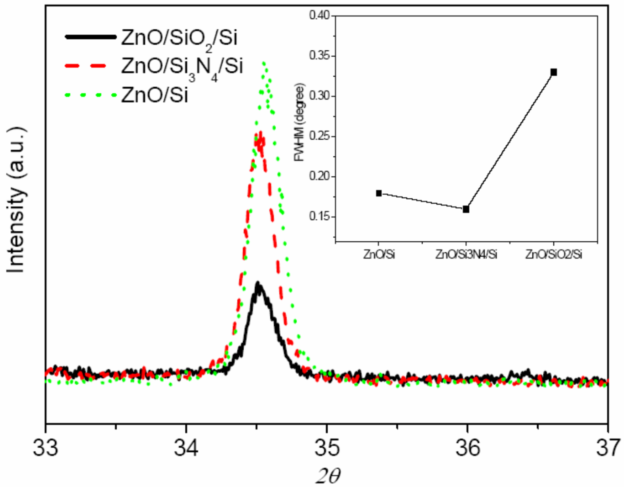

Figure 3.8: X-ray diffraction patterns and FWHM (inset) of ZnO films sputtered at Si, SiO_2/Si, and Si_3N_4/Si after annealing at 850˚C in oxygen atmospheres.

The values of full width at half maximum (FWHM) are 0.18°, 0.16°, and 0.33° for the ZnO films grown on Si, Si_3N_4/Si, and SiO_2/Si substrates, respectively. In addition, it was observed that the ZnO films annealed at 850°C in nitrogen (N_2) exhibit a similar trend to that annealed in O_2 atmosphere but the corresponding values (0.20°, 0.19°, and 0.45°) of FWHM are larger in N_2 atmosphere. It implies that O_2-annealing presents a positive effect on crystalline characteristics of ZnO films than N_2-annealing.

Figure 3.9 shows the bright-field transmission electron microscopy (TEM) images of the ZnO films deposited on various substrates and then annealed at 850 ^{o}C in O_2 atmosphere. The cross-sectional microstructure of all the ZnO films can be clearly divided into two regions: crystalline (columnar shape) and inter-layer (flat-belt). The columnar structure was grown along c-axis orientation but the inter-layer forms a disorder structure that may play a crucial important role in reducing the stress due to lattice mismatch between ZnO and Si substrate. Both ZnO films deposited on Si and Si_3N_4/Si substrates present similar cross-sectional microstructure as one can see **Figure 3.9(a)**. However, as the ZnO film was deposited on SiO_2/Si substrate, a large variation appears on the microstructure as shown in **Figure 3.9(b)**. A thicker disordered ZnO inter-layer with rougher interface was identified for ZnO film grown on SiO_2/Si compared to that on Si_3N_4/Si and Si. The formation of the thicker disordered ZnO inter-layer in ZnO/SiO_2/Si structure was believed to be strongly dependent on the crystal characteristics of SiO_2-buffered layer. Some researches reported that as the SiO_2 film was annealed at a high temperature (exceeding 700°C), many defects such as oxygen vacancies are easily produced and it becomes the non-stoichiometric composition **[97,98]**. As illustrated in **Figure 3.9(c)**, more oxygen vacancies are induced in the ZnO film deposited on SiO_2-buffered layer. Furthermore, it was well known that the diffusivity of the oxygen vacancies is faster than other defects in ceramic oxides. Therefore, in this condition, a thicker ZnO inter-layer was formed on SiO_2-buffered layer compared to Si_3N_4-buffered layer.

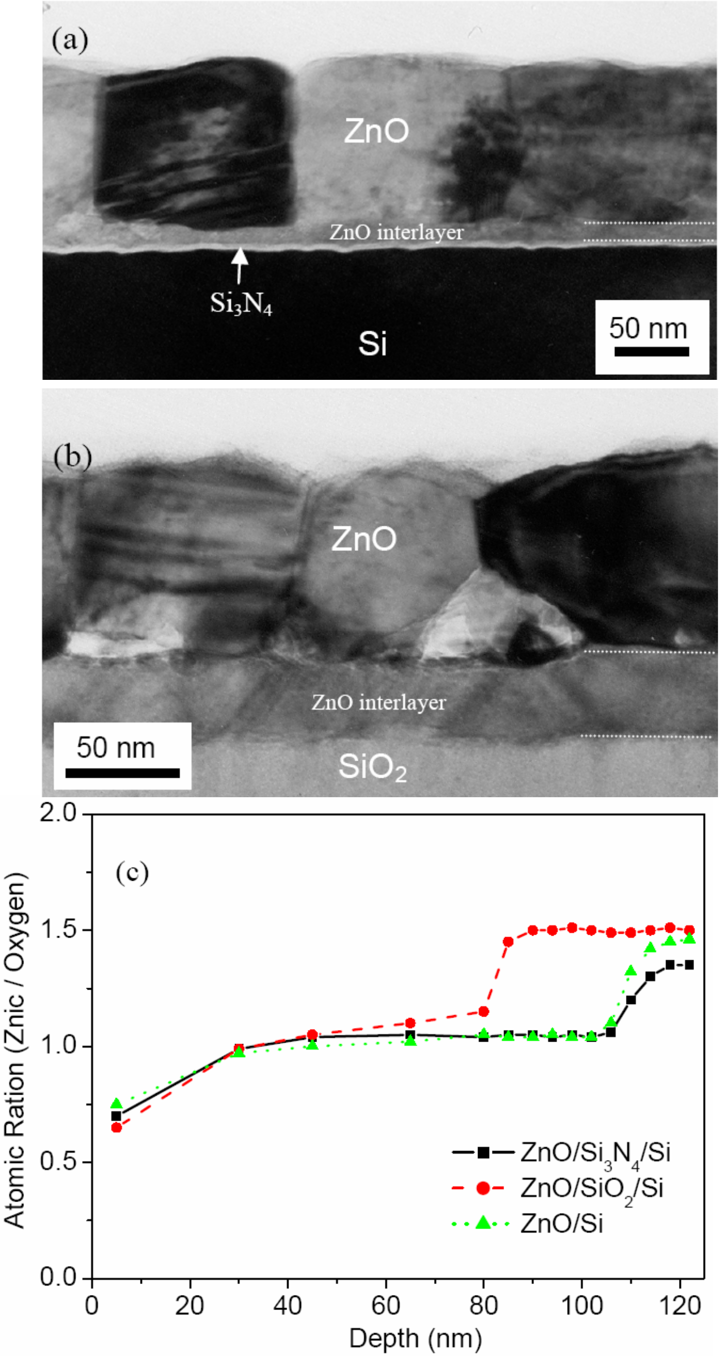

Figure 3.9: Cross-sectional transmission electron microscopy images of the ZnO grown on (a) Si_3N_4/Si, (b) SiO_2/Si substrates after annealing at 850˚C in oxygen atmospheres. (c) Atomic ratio of zinc and oxygen at different depths form the surface of the ZnO film on Si with various buffer-layer.

X-ray photoelectron spectroscopy (XPS) was further used to investigate the depth-profile of element composition from columnar ZnO shape through disordered ZnO inter-layer. As shown in **Figure 3.9(c)**, it was found that the relative Zn/O ratio obviously increases around the inter-layer ZnO region in all the cases, implying that the ZnO inter-layer (disordered layer) is non-stoichiometric and contains more oxygen vacancies ($Vo^{\bullet\bullet}$)**.** Moreover, it was found that the defect concentration of oxygen vacancy in $ZnO/SiO_2/Si$ films was apparently more than that in $ZnO/Si_3N_4/Si$ films as confirmed by XPS analysis O 1s peak at 531.25 ± 0.2 eV. In addition, a higher $Vo^{\bullet\bullet}$ concentration was also detected in $ZnO/SiO_2/Si$ films than that in ZnO/Si that could be due to the diffusion of more extra-defects (oxygen vacancies) from the SiO_2 buffered-layer into ZnO films during later thermal annealing. In contrast to SiO_2/Si and Si substrates, the diffusion of oxygen vacancies from Si_3N_4/Si into ZnO were almost undetected.

Figure 3.10 illustrates the room-temperature PL spectra of ZnO films deposited on various substrates and then annealed at 850 ^{o}C in O_2 atmosphere. From the spectra, it is noticed that the peak intensity of the UV emission depends markedly on the used substrates. The ZnO films deposited on Si substrate show a sharp free exciton peak around 379 nm and a broad peak in the visible region between 550 and 650 nm. The PL emission peak corresponding to the UV emission appears around 377-379 nm (3.29-3.27 eV) that should be a near band edge emission of ZnO films due to an exciton-related activity **[92]**. Concerning the visible emission, it should result from deep-level emission which is generally associated with zinc interstitials and oxygen vacancies in ZnO lattice. However, it was found that the PL spectra of ZnO deposited on SiO_2/Si substrate are apparently different from others. The PL spectra present two UV emissions peaked at 377 nm (3.29 eV) and 394 nm (3.15 eV). The former one is the normally observed UV peak and the latter one is very similar to the one (401 nm) reported by Jeong *et. al.* in low-temperature PL spectra of ZnO films grown on p-type Si under oxygen-rich conditions. According to the observation of Jeong *et. al.,* the emission band was assigned to the electron transition from the bottom of the conduction band to the zinc vacancies level **[99]**. However, in our case, it may suggest that the UV emission peak at 394 nm (3.15 eV) results from the variation in microstructure and is assigned to the transition form oxygen vacancy ($V_o^{\bullet}$) level to valence band, positioned approximately 0.20 eV below the conduction band edge **[100]**. In addition to the UV emission, the visible emission is also changed. The spectra corresponding to visible emission region also exhibit two broad peaks around 495 (~2.50 eV) and 605 nm (~2.05 eV). It implies that there may be two different defect transitions occurring at the same time. According to the defect model proposed by Lima,**[89]** the green luminescence (~2.5 eV) corresponds to a transition from $Zn^{\bullet}$ to $Zn^{\bullet\bullet}$ and the red luminescence (~2.0 eV) is attributed to the oxygen vacancies ($Vo^{\bullet\bullet}$). It was believed that the variation of PL spectra in $ZnO/SiO_2/Si$ was influenced by the change of crystal characteristics (thicker ZnO inter-layer and rough interface between columnar ZnO and ZnO inter-layer) and defect concentration (non-stoichiometric). According to the investigation of Zhao *et. al.* for asymmetric double GaAs/AlGaAs quantum well, it was reported that the peak splitting in the PL spectra may result from two transitions probably due to the geometric fluctuations (layer-thickness fluctuation) **[101]**. Therefore, a thicker ZnO inter-layer could effectively relieve the stress to assist the crystal growth but the disordered ZnO inter-layer may induce many defects to change the PL spectra. In contrast, $ZnO/Si_3N_4/Si$ structure does not exhibit those double emission peaks. In other words, only a strongly sharp UV peak centered at 377 nm (3.29 eV) was detected. It was believed that the ZnO film grown on Si_3N_4/Si substrate has improved stoichiometry with little oxygen vacancies and Zn interstitials concentration as shown in **Figure**

3.9(c) because the PL emission characteristics of ZnO films are strongly dependent on both the film stoichiometry and the crystal quality of the film. Especially, as the buffer layer (SiO_2) becomes thicker in $ZnO/SiO_2/Si$ structure, the physical and optical properties of ZnO films will become poor because a thicker SiO_2 layer will induce more “extra-defects” during annealing process. In contrast, in $ZnO/Si_3N_4/Si$ structure, a thicker buffer layer (Si_3N_4) will prevent the formation and diffusion of extra defects and thus, the film stoichiometry of ZnO will be improved. Therefore, ZnO films grown on Si_3N_4/Si substrate would present better physical and optical properties than that on other substrates.

Low-temperature PL measurement was performed for the more detailed investigation of the emission characteristics. As shown in **Figure 3.11**, the obtained PL spectra were measured at 10 ^oK from the same samples as shown in **Figure 3.10**. The ZnO films grown on Si_3N_4/Si substrate still show the strongest exciton-related emission peak at 374 nm (~3.32 eV) along with blue shift. On the other hand, for the ZnO film grown on SiO_2/Si, the PL peak centered at 394 nm becomes weak and more broadening (as compared with **Figure 3.10**) but the deep-level emission remains unchanged. In general, the lattice distance would be slightly compressed in low temperature environment and the local defect transition may be thermally quenched as evidenced from the variation in the emission peak at 394 nm. The double peaks in the ultraviolet region coexist in the whole temperature between 10 and 300 ^oK but show different intensity. This indicates that there are thermal transfer effects. It seems that the local defect transition may be thermally quenched at low temperature and a large amount of oxygen vacancies to induce defects transfer form oxygen vacancies ($V_o^{\bullet}$) level to valence band was confined due to microstructure fluctuations. Further investigations for the temperature dependence on PL are in progress and the results will be reported in the near future. Moreover, although all the specimens were n-type

ZnO films, it was found that the carrier concentration of ZnO/Si_3N_4/Si sample is very close to intrinsic ZnO (~1.40×10^{14} cm^{-3}) and can be increased by post-treatment. Thus, it may offer alternative route to develop p-type ZnO films on Si_3N_4/Si.

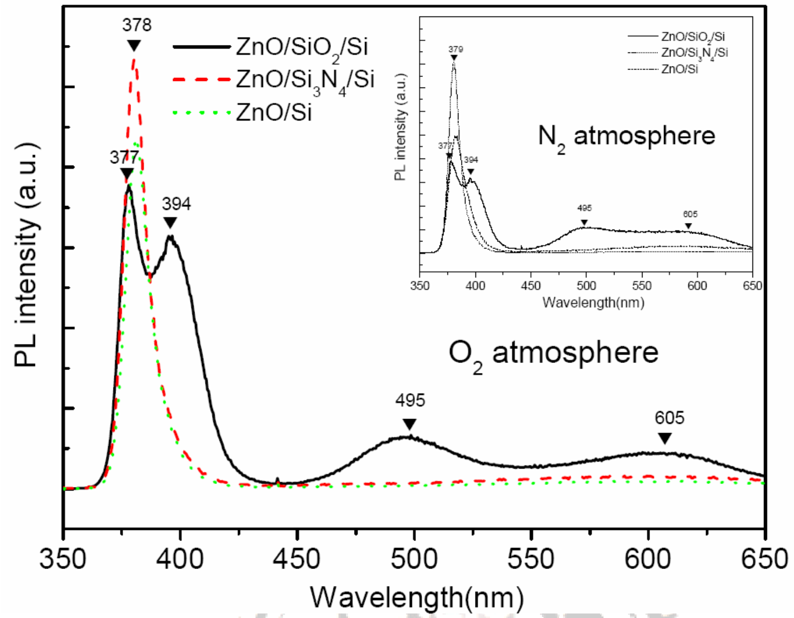

Figure 3.10: Room temperature PL spectra of the ZnO films deposited on various substrates after annealing at 850˚C in oxygen and nitrogen (inset) atmospheres.

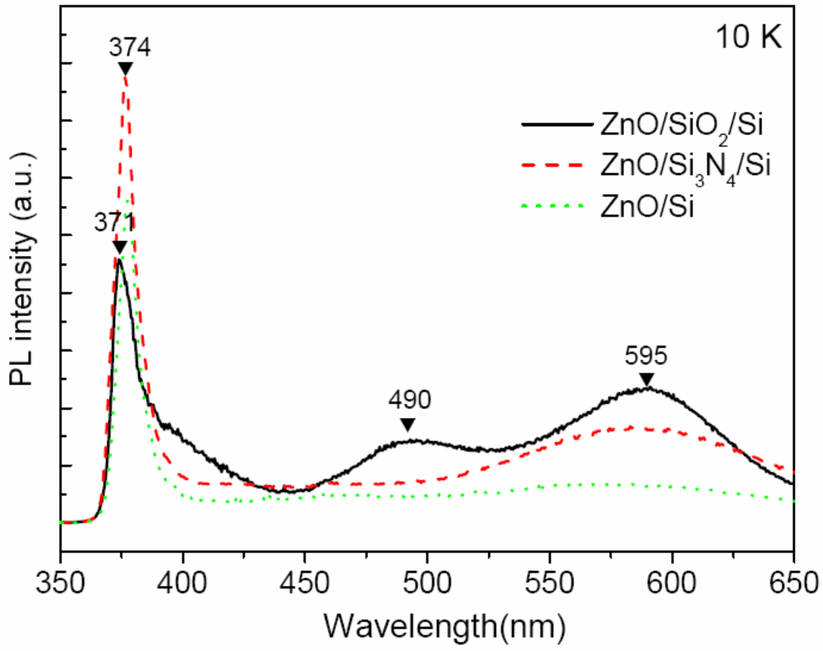

Figure 3.11: Low-temperature PL spectra measured at 10 K for the ZnO films grown at various substrates after annealing at 850˚C in oxygen atmospheres.

3.4 Summary

ZnO films have been grown on Si (001) substrates by radio-frequency magnetron sputtering. It was found the all ZnO films have strongly preferred-orientation (c-axis). Both defects of zinc interstitials and oxygen vacancies are intrinsic and hard to be removed during film growth. However, in this study, it has been demonstrated that it is possible to control the UV and deep-level emissions in the sputtered ZnO films by changing annealing temperatures and using different gas atmospheres. Therefore, a sharp UV emission with invisible deep-level peaks can be attained for the ZnO film sputtered at an OMR of 5 % and annealed at 850˚C in O_2 atmosphere. Moreover, we have also shown that the emission characteristics of ZnO films grown on Si by radio-frequency magnetron sputtering are strongly influenced by the buffer layer. Although all the ZnO films have strongly c-axis orientation and present similar columnar-like crystal structure, the PL results in this study apparently reveal that the buffer layer plays a crucial role in the crystal quality and film stoichiometry of the disordered ZnO inter-layer. If the ZnO film was grown on Si_3N_4/Si, a very strong UV along with invisible deep-level emission was detected because the Si_3N_4 can effectively improve film stoichiometry and reduce the defect formation of oxygen vacancies and Zn interstitials compared to SiO_2 on Si. Moreover, the carrier concentration of the ZnO/Si_3N_4/Si sample is very close to that of intrinsic ZnO ($\sim 1.40\times 10^{14}$ cm^{-3}) and can be increased by post-treatment.

Chapter 4

Doped ZnO thin films by ion implantation

4.1 Introduction

To develop ZnO-based optoelectronic devices, it is necessary to grow high-quality both *p*- and *n*-type ZnO thin films. The *n*-type ZnO is easily available even without any doping, while it has been recognized that it is very difficult to obtain *p*-type ZnO because ZnO is a natural *n*-type semiconductor and the acceptors may have a natural tendency to pair with native defects or background impurities to form electrically inactive complexes although high densities of holes could be achieved with nitrogen as the dopant along with other techniques. Furthermore, the presence of native defects, such as zinc interstitials and oxygen vacancies, causes a deviation from stoichiometry **[102]**. In order to overcome this problem, recently, several research groups proposed many methods to obtain *p*-type ZnO films **[103-105]**. Generally, choosing group V element to be a dopant material is a common agreement.

4.2 Phosphorous-implanted in ZnO thin films

So far, there have been several research groups proposed the formation of *p*-type ZnO by various dopants and doping method **[103,106]**. However, no detailed studies were made to investigate the effect of group V-dopants on the structural change and photoluminescence properties of ZnO films. **Figure 4.1** shows the XRD patterns of the phosphorous-implanted (fluence of 5×10^{12}, 1×10^{14}, and 5×10^{15} cm^{-2}) and non-implanted ZnO thin films annealed at 850˚C in nitrogen atmospheres. With an increase of phosphorus concentration, the (002)-peak intensity decreased obviously and a weak diffraction peak was observed at the fluence of 5×10^{15} cm^{-2} for the phosphorous-implanted ZnO films annealed at 850^{o}C in nitrogen. Similar behavior was also observed in the case of oxygen atmosphere. It was believed that the phenomenon is strongly dependent on the solubility limit of the implanted phosphorus in ZnO films. In addition, the (002) diffraction peak of the ZnO films was shifted towards the direction of smaller 2θ angle with the increase of fluence from 5×10^{12} to 5×10^{15} cm^{-2}. According to Bragg Law, the shift toward smaller 2θ direction indicates an increase of the lattice constant that was considered due to the incorporation of the phosphorus into ZnO matrix to form antisite P_{Zn} or phosphide (PO_4^-) compound. **Figure 4.2** shows the depth profile of phosphorus-implanted ZnO films with various fluences. As it can be seen, the secondary ion counts of phosphorus abruptly increase near the side of Si substrate regions. It was believed due to the original implanted phosphorus and incomplete diffusion in annealing process. This concentration corresponds to the solubility **[106]** of phosphorus in ZnO film that is determined as 2.5×10^{17}, 1.5×10^{18}, and 8.5×10^{19} ions/cm^3 for the fluence of 5×10^{12}, 1×10^{14}, and 5×10^{15} ions/cm^2, respectively.

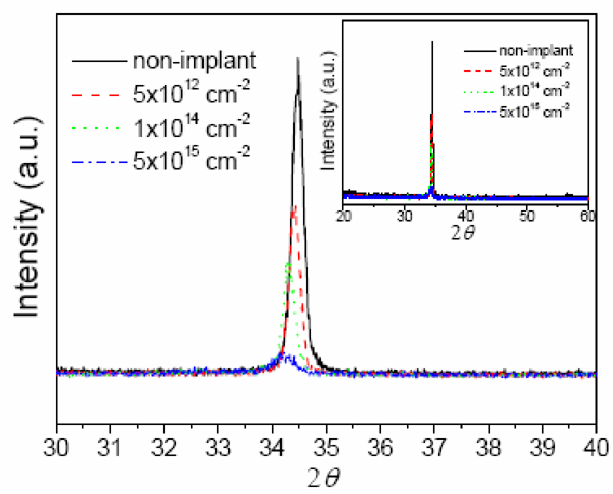

Figure 4.1: XRD patterns of ZnO films implanted with different phosphorus fluences and annealed at 850˚C in nitrogen.

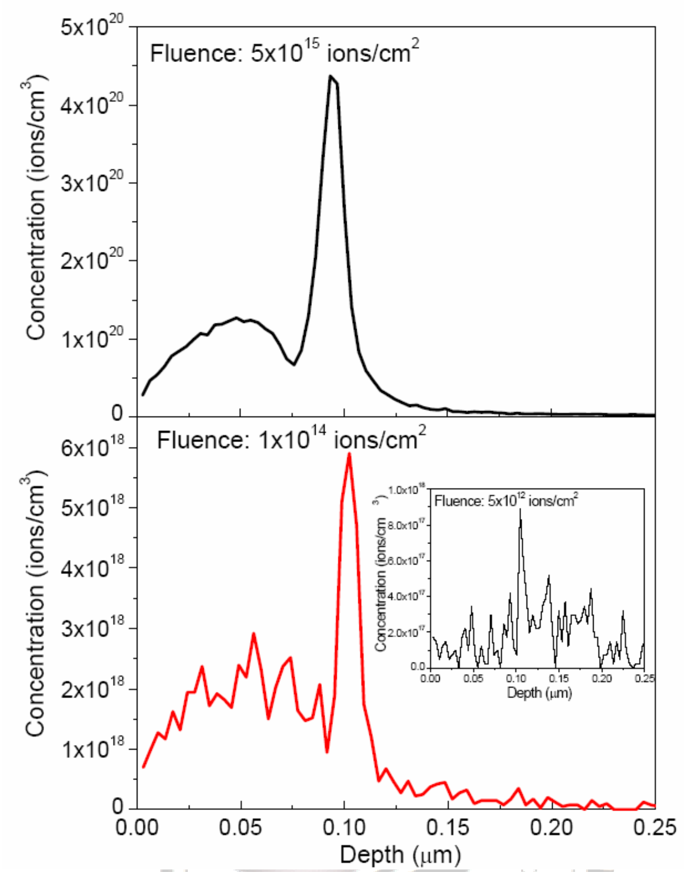

Figure 4.2: SIMS depth profile of ZnO films implanted with different phosphorus fluences after annealed at 850°C in nitrogen atmospheres.

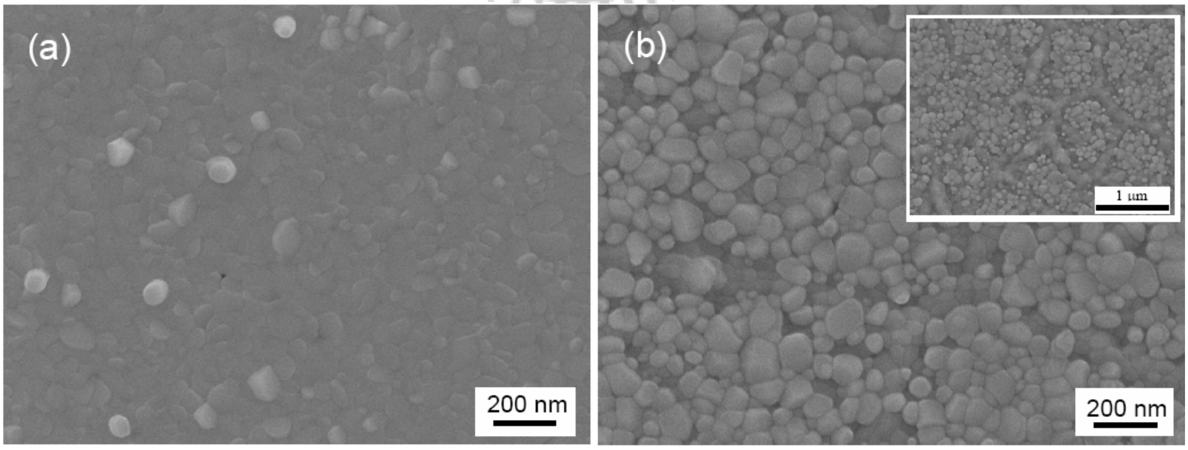

Figure 4.3: SEM images of ZnO films doped with phosphorus at fluences of (a) 5×10^{12} and (b) 5×10^{15} ions/cm^2 and then annealed at 850°C in nitrogen atmosphere.

Figure 4.3 shows the SEM images of ZnO films doped with phosphorus and then annealed at 850˚C in nitrogen atmosphere. As shown in **Figure 4.3(a)**, both ZnO films with non-implanted and implanted with 5×10^{12} ions/cm^2 exhibit similar surface morphology (r.m.s: ~2.5 nm). Above that concentration, i.e., 5×10^{15} ions/cm^2, **Figure 4.3(b)** illustrates that several ridge regions are formed in ZnO films (r.m.s.:~5.4 nm). It was postulated that the formation of the glass-like ridge structure may be related to the excess doping of phosphorus. In order to investigate the phosphorus doping effect on the crystalline of ZnO films, TEM analysis were performed. As shown in **Figure 4.4** for ZnO films annealed at 850˚C in nitrogen atmosphere, it was found that the cross-sectional microstructure was clearly divided into two regions: crystalline (columnar shape) and interlayer (flat-belt) structure. The interlayer could be considered as a buffer layer to reduce the stress due to lattice mismatch between ZnO and Si. However, for ZnO films with 1×10^{14} ions/cm^2 implanted, several small clusters were observed in the ZnO interlayer in **Figure 4.4(b)** as marked with arrows. According to energy-dispersive spectrometry (EDS) measurement, those clusters were primarily composed of phosphorus, zinc and oxygen elements that may be related to the formation of glass-like ridge structure. **Figure 4.5** shows the room-temperature PL spectra of non-implanted and phosphorus-implanted ZnO films annealed at 850˚C in nitrogen atmosphere The PL behavior for deep-level emission of ZnO films implanted with various fluences of phosphorus is also illustrated in the inset of **Figure 4.5** for comparison. The inset is the deep-level emission of ZnO films implanted with various fluences. It was observed that the peak intensity of the UV emission varies with the concentration of fluence. A very stronger UV peak (378 nm) and a relatively low deep-level emission (545 nm) were obtained for the non-implanted sample. However, as the ZnO films were implanted with different phosphorus fluences and annealed in nitrogen atmosphere, the UV emission peak of the ZnO films becomes weaker and presents slightly red shift as compared to the non-implanted one. This PL result along with the XRD analysis and surface morphology implies that there should be a solubility limit for phosphorus incorporated into ZnO films. If the implanted concentration is close to the solubility limit, both crystal structure and NBE emission would be strongly influenced and become poor.

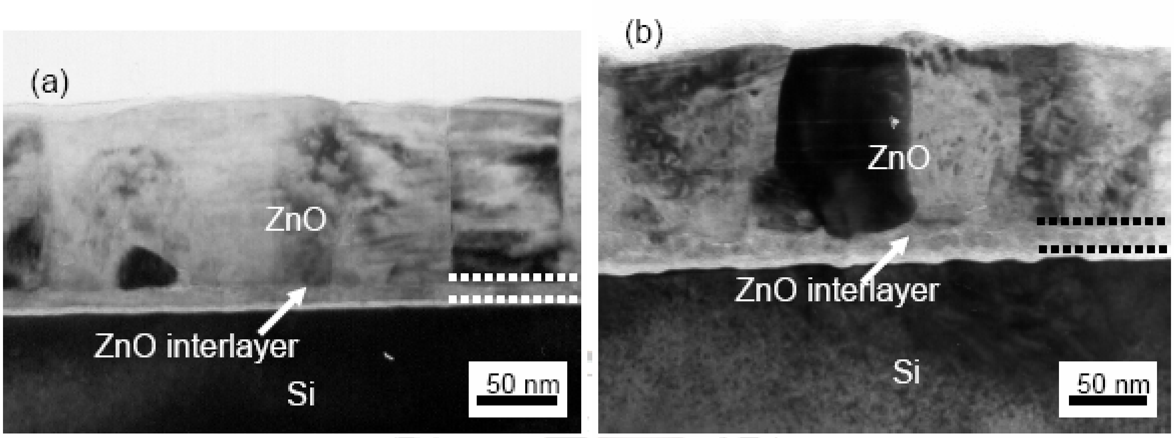

Figure 4.4: Cross-sectional TEM images of ZnO films annealed at 850˚C in nitrogen atmospheres. (a) without phosphorus-implanted, (b) with phosphorus-implanted (fluence: 1×10^{14} ions/cm^2).

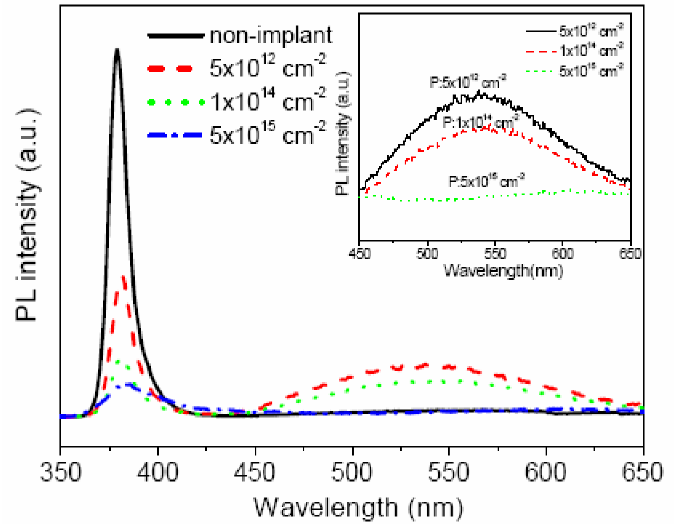

Figure 4.5: Dependence of fluences conditions on room temperature PL spectra for the phosphorus-implanted ZnO films annealed at 850˚C in nitrogen atmospheres. The inset is the deep-level emission of ZnO films implanted with various fluences of phosphorus.

On the other hand, as the phosphorus-implanted ZnO films were annealed in O_2 atmosphere (not shown here), the UV peak intensity was remarkably decreased compared to that annealed in N_2 atmosphere. In addition, with increasing phosphorus-implanted concentration up to 1×10^{14} fluence, a weaker UV peak accompanied with a stronger deep-level emission around 545 nm was detected in O_2 atmosphere than that in N_2 atmosphere. It implies that more defects were probably induced in ZnO film annealed in oxygen atmosphere than that annealed in nitrogen atmosphere. Therefore, according to above discussion, it was believed that the property deterioration in the phosphorus-implanted ZnO films is correlated closely with the formation of defects and some glassy phase (MPO_4^-) as evidenced from **Figure 4.4(b)** of TEM. In addition, the resistivity and carrier type of non-implanted and phosphorus-implanted ZnO films were further investigated by Hall measurement. The non-implanted ZnO film has the 52 Ωcm and exhibits n-type (-1.65×10^{16} cm^{-3}) characteristics. However, with phosphorus-implanted fluence of 5×10^{12} ions/cm^{-2}, the resistivity of phosphorus-doping ZnO films increases up to 256Ωcm but the carrier concentration approaches to 1.65×10^{15} cm^{-3}. Thus, the conversion of carrier type was never observed that is probably attributed to the formation of phosphide even though the phosphorus element was successfully incorporated into ZnO films.

4.3 Characterization of *p*-type ZnO films

Recently, several thin-film growers have demonstrated that nitrogen doping was an effective method to realize *p*-type ZnO films because N has the smallest ionization energy in group V-dopants and similar radii to that of oxygen atoms. In this session, we used nitrogen-implanted and Si_3N_4 buffer layer to fabricate *p*-type ZnO thin films.

Figure 4.6 shows the XRD pattern of nitrogen-implanted ZnO thin films on Si and Si_3N_4/Si, and then annealed at 850^{o}C in N_2 atmosphere. Only a sharp diffraction peak of (002) at $2\theta = 34.5^\circ$ can be detected for all the ZnO films, indicating that these ZnO films were highly c-axis oriented. However, as increasing the nitrogen-implanted concentration form 5×10^{12} to 5×10^{15} cm^{-2}, the intensity of the (002) XRD peak in ZnO films grown on Si substrate decreases as shown in inset of **Figure 4.6**. In contrast, when the ZnO films were grown on Si_3N_4/Si substrates, it was found that (002) diffraction peak becomes stronger with the increase of the implanted nitrogen ions from 5×10^{12} to 1×10^{14} cm^{-2} (**Figure 4.6**). This reveals that the occupation of the implanted nitrogen ions on oxygen vacancies can improve the crystallinity of ZnO films on Si_3N_4/Si can be improved. However, above that, the peak intensity was rapidly decreased, implying that more implanted nitrogen ions probably induces extra defects and this would lead to the lattice distortion.

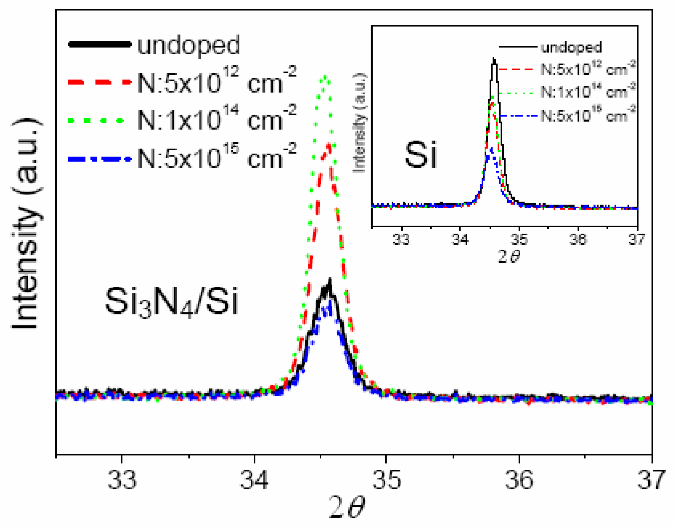

Figure 4.6: XRD of ZnO films sputtered at Si (inset), and Si_3N_4/Si substrates with or without nitrogen-implanted various doses.

The electrical conduction type of nitrogen-implanted ZnO films as a function of doping doses is shown in **Figure 4.7**. The nitrogen-implanted ZnO films on Si substrate show *n*-type conduction independent of the implanted nitrogen ions concentration. In sharp contrast, the nitrogen-implanted ZnO films on Si_3N_4/Si substrate exhibit *p*-type conduction and the carrier concentration increases up to 7.3×10^{17} cm^{-3} with an increase of nitrogen-implanted concentration from 5×10^{12} to 1×10^{14} cm^{-2}. According to our previous study, as the ZnO films were deposited on the Si_3N_4/Si structure, x-ray photoelectron spectroscopy analysis demonstrates that a lower oxygen vacancies concentration and thinner interface layer was detected for ZnO on Si_3N_4/Si structure compared to that on Si **[107]**. Furthermore, the film stoichiometry was improved because of the reduction in oxygen vacancies, indicating the ratio of Zn:O was decreased **[108]**. In this condition, the concentration of active acceptors may exceed the donor concentration so that the conduction type was changed from *n* to *p* type. The dependence of conduction type on the implanted nitrogen ions concentration in ZnO films in **Figure 4.7** suggests the nitrogen-implanted process can product more holelike carries to transform original conduction (compensate the native carriers). However, a further increase in the implanted dose of the nitrogen ions up to 5×10^{15} cm^{-2} leads to a decrease in hole concentration of *p*-ZnO and the conduction type of ZnO films would approach the intrinsic conductor.

Resistivity and Hall mobility as a function of implanted nitrogen ions doses were measured and are shown in **Figure 4.8** for *p*-type conduction ZnO films. As increasing nitrogen ions doses from 5×10^{12} to 1×10^{14} cm^{-2}, both hole concentration and Hall mobility increase, but the resistivity decreases. The *p*-type ZnO films grown on Si_3N_4/Si show a hole concentration of 7.3×10^{17} cm^{-3}, a mobility of 6.02 cm^2/Vs, and a low resisitivity of 10.3 Ω cm. Above that (1×10^{14} cm^{-2}), both hole concentration and Hall mobility decreases, but an increase in resistivity was observed. The initial increase in the hole concentration is due to a decrease in oxygen vacancy as the implanted nitrogen ions doses increase. The decrease in hole concentration after the maximum value is caused by the formation of more defects due to excess nitrogen ions that can compensate for a hole carrier which may correspond to the degradation of the crystal quality in *p*-type ZnO films as supported by the decrease in the peak intensity of (002) XRD peak in **Figure 4.6** for the nitrogen-implanted ZnO film with the dose of 5×10^{15} cm^{-2}.

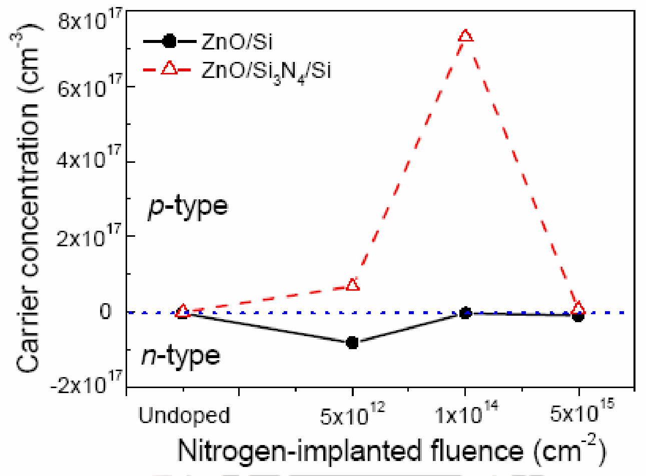

Figure 4.7: Electrical conduction type of nitrogen-implanted ZnO films as a function of various doses.

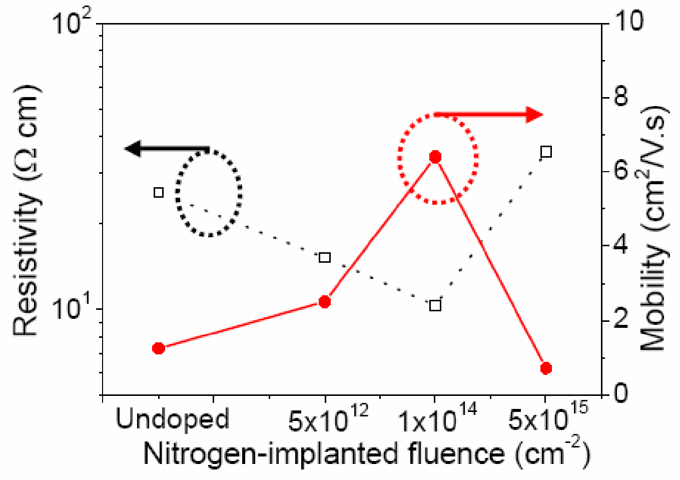

Figure 4.8: Variation of resistivity and Hall mobility as a function of different nitrogen-implanted doses.

Recently, many research groups announced that *p*-type ZnO were fabricated by doping group-V elements and proposed a reasonable explanation for the mechanism of atom substitution in crystal structure, such as N_O. However, almost no evidence was presented for the behavior of atom occupation in *p*-type ZnO fine structure. Therefore, in order to further understand the local structure of *p*-type ZnO films, the extended x-ray absorption fine structure was investigated. **Figure 4.9** shows the pseudoradial distribution functions obtained from the k^3-weighted Fourier transforms at Zn *K* edge for the nonimplanted and nitrogen-implanted ZnO films on a Si_3N_4/Si structure, where pure ZnO powder was used as standards for comparison. The first peak in the Fourier transforms corresponds to the nearest-neighbor distance around zinc atoms. The peak position of zinc to oxygen for both bulk powder standards (ZnO: 99.999%) and nonimplanted ZnO thin films is equal to 0.1945 nm. For the ZnO film implanted with 1×10^{14} cm^{-2} N^+ dose, the Zn-O bond length in ZnO/Si_3N_4/Si is very similar to that of nonimplanted ZnO films and bulk powder standards. However, for the second nearest-neighbor distance around Zn^{2+}, it was found that the Zn-Zn bond length for nonimplanted ZnO films is shorter than that of nitrogen-implanted ZnO films. It could be due to the existence of oxygen vacancies in the ZnO lattice matrix that causes the secondary nearest-neighbor distance to become shorter. In comparison with bulk powder standards (0.327 nm), a little larger Zn-Zn bond length (3.28Å) was also detected for N^+-implanted ZnO films**.** These observations suggest that the implantation of nitrogen ions into ZnO films could affect the local structure of ZnO film, such as bond distance, but a limited range of 1×10^{14} cm^{-2} nitrogen ions dose can effectively improve the crystal quality of ZnO films.

Figure 4.10 illustrates the room-temperature PL spectrum of ZnO films implanted with various nitrogen ions doses on Si_3N_4/Si substrates. UV emission with peaks at 3.31, 3.28, 3.29, and 3.30 eV is dominantly observed for the ZnO films implanted with 0, 5×10^{12}, 1×10^{14}, and 5×10^{15} cm^{-2} nitrogen ions dose, respectively. According to the spectrum, it is noticed that the peak intensity of the UV emission depends markedly on the nitrogen-implanted dose. The ZnO film implanted with a 1×10^{14} cm^{-2} nitrogen ions dose not only shows a stronger peak intensity but also has a narrower full width at half maximum of 95 meV than that (110 meV) of nonimplanted ZnO films. Furthermore, the relative intensity ratio of UV emission (I_{UV}) to that of deep-level emission (I_{DLE}) are measured about 13(nonimplanted sample), 55-56 (implanted with 5×10^{12}-1×10^{14} cm^{-2} nitrogen ions dose), and 25(implanted with 5×10^{15} cm^{-2} nitrogen ions dose), at room temperature, respectively. This high ratio implies that the nitrogen-implanted ZnO film is of high optical quality.

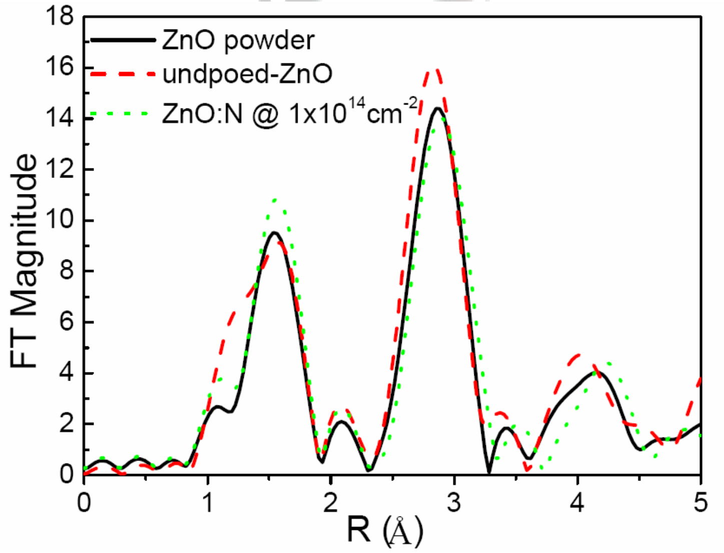

Figure 4.9: Fourier transforms at Zn *K*-edge for the ZnO powder standards, non-implanted, and nitrogen-implanted ZnO/Si_3N_4/Si samples.

4.4 Summary

Phosphorus-implanted in ZnO films tends to react with zinc and oxygen elements to form the clusters and this would induce defects as revealed from PL spectra. Moreover, both the crystalline quality and optical property will be deteriorated due to the formation of phosphide compounds. Therefore, in this condition, high resistive but not p-type ZnO film is obtained by phosphorus doping.

However, in another study, we have fabricated the reproducible *p*-type ZnO films grown on Si_3N_4/Si by rf magnetron sputtering, implanted with 5×10^{12}-1×10^{14} cm^{-2} nitrogen ions dose and then annealed at 850 ^{o}C in N_2 ambient. The EXAFS analysis reveals the local structural variation of the *p*-type ZnO films due to the substitution of nitrogen ions for oxygen ions in *p*-type ZnO films. The hole concentration, carrier mobility, and resistivity of *p*-type ZnO films were 5.0×10^{16}-7.3×10^{17} cm^{-3}, 2.51-6.02 cm^{-2}Vs, and 10.11-15.3 Ωcm, respectively. PL spectra of the nitrogen-implanted ZnO/Si_3N_4/Si showed a sharp UV emission and invisible deep-level transition at room-temperature measurement. The high value of I_{UV}/I_{DLE} in nitrogen-implanted ZnO/Si_3N_4/Si also shows better optical quality relative to nonimplanted and nitrogen-implanted into ZnO/Si samples. These results suggest that nitrogen-implanted ZnO films deposited on a Si buffer with Si_3N_4 show electrical and optical behaviors that make them excellent candidates for a good *p*-type layer for ZnO-based optoelectronic device on a Si-based substrate.

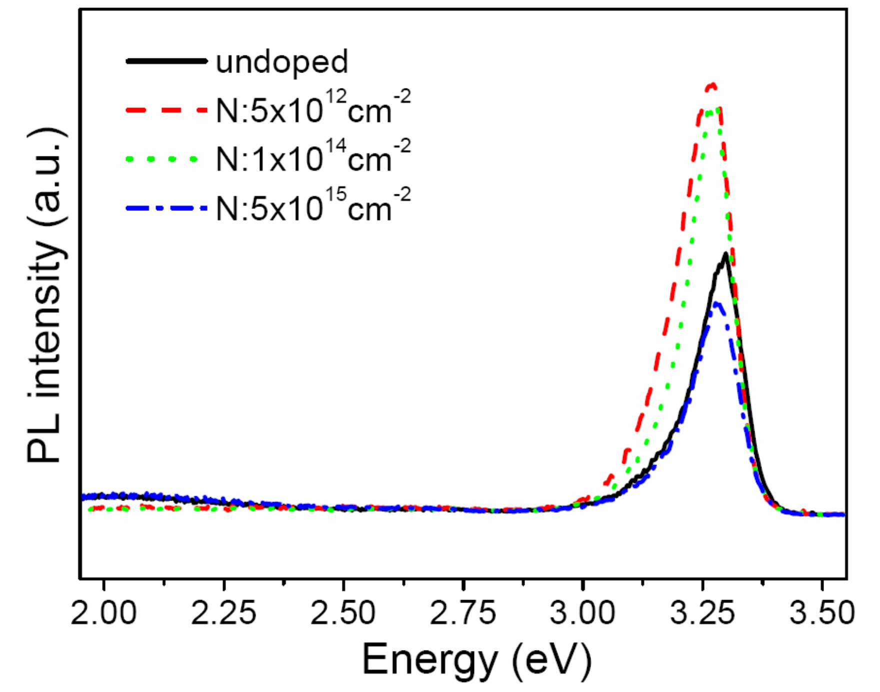

Figure 4.10: Room-temperature PL spectra of non-implanted and nitrogen-implanted ZnO/Si_3N_4/Si samples.

Chapter 5

Physical characteristics of ZnO nanorods via soft chemical process

5.1 Introduction

The ZnO nanorods have been thought to be the most suitable for ultraviolet (UV) laser device because of its large exciton binding energy of 60 meV compared to that (26 meV) of GaN at room temperature. Furthermore, many reports in the related literature have demonstrated that directionally grown ZnO nanorods can effectively decrease the threshold power to achieve the UV lasing emission at room-temperature. Strong efforts have been made to fabricate one-dimensional ZnO, including thermal decomposition**[109]**, hydrothermal synthesis**[110]**, vapor phase transport**[111]**, and metal-organic chemical vapor deposition (MOCVD) **[112]**. Recently, many wet-chemical approaches have been used for large oriented arrays of ZnO nanorods on polycrystalline (or single-crystalline) substrates from aqueous solutions **[113,114]**. However, it is worth noting that without suitable treatment on the substrates, highly oriented ZnO nanorods grown on a Si wafer has been rarely achieved.

5.2 ZnO nanorods array on organic substrate

Recently, many research groups used ZnO nanoparticles as seeds to grow the large-scale and well-oriented ZnO nanorods on Si substrates via low temperature process **[115]**. However, it is potentially more important to synthesize 1D nanoscale materials on organic substrates for the applications of flexible display and photoelectronic devices. Therefore, we wanted to investigate the nucleation and growth behavior of ZnO nanorods on organic substrates in aqueous solutions. **Figure 5.1(a)** shows the surface images of large-scale arrayed ZnO nanorods grown on polystyrene (PS)/polycarbonate (PC) substrates. It was found that the ZnO nanorods have a well-defined hexagonal plane with a homogeneous diameter of approximately ~60 nm due to uniform growth rate. The cross-sectional SEM image in **Figure 5.1(b)** shows that the ZnO nanorods are directionally and densely grown over the entire PS surface of the substrates. Furthermore, it was noted that the well-aligned ZnO nanorods (**Figure 5.1(c)**) can be developed after the removal of the PS beads from the specimen fabricated using the same conditions as **Figure 5.1(b)**. It implies that the PS layer can supply the appropriate environment to increase the nucleation sites for ZnO nanorods.

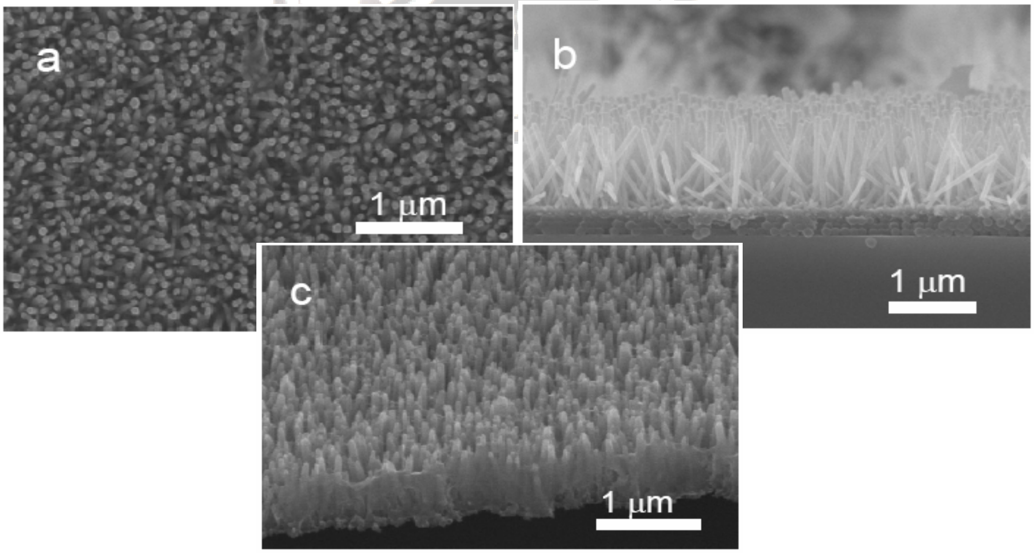

Figure 5.1: SEM images of large arrays of oriented ZnO nanorods grown on polystyrene (PS)/polycarbonate (PC) substrates for 8 h. (a) Low magnification, face-on view. (b) Cross-sectional SEM image of ZnO nanorods grown on PS/PC substrates. (c) SEM image of ZnO nanorods grown on PS/PC substrates after removing the PS beads.

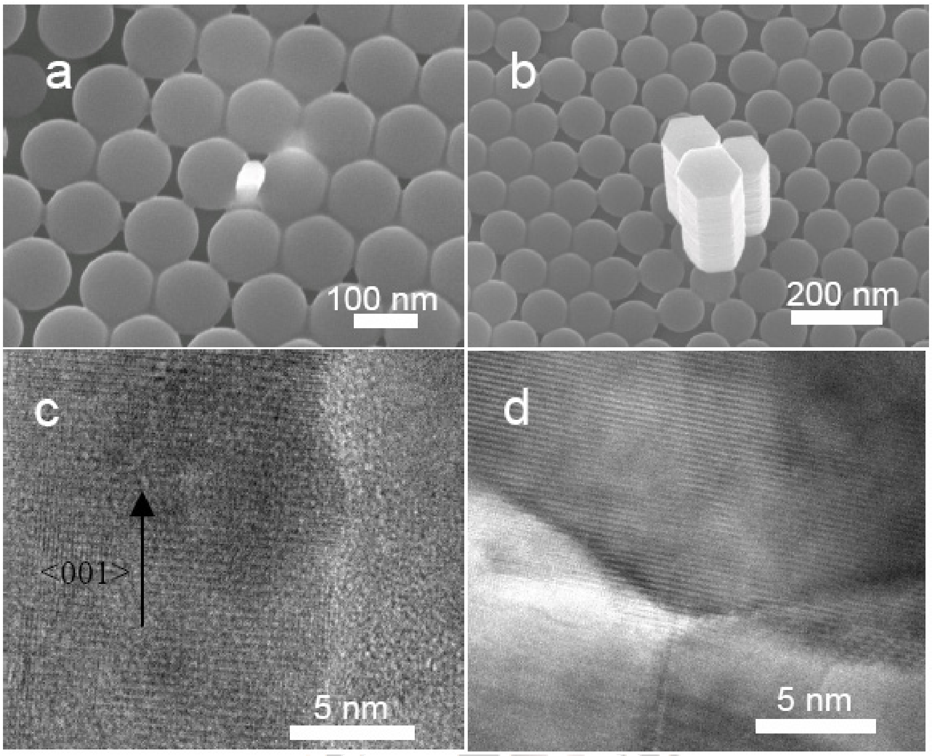

Figure 5.2: SEM images of ZnO nanorods grown on PS/PC substrates as a function of reaction time at 75^{o}C. (a)1 h, and (b) 5 h. (c) High-resolution TEM image of ZnO nanorods grown on organic substrates. (d) High-resolution TEM image of the interface region between ZnO nanorods and ultra-thin ZnO monolayer/ PC.

To understand how the well-aligned ZnO nanorods were developed on the organic substrates, the sample was subjected to grow at 75^{o}C in a variety of time. The first initial stage (t < 0.5 h) can be considered as the induction time, during which an ultra-thin monolayer was slowly generated under the PS beads in the solution. It is difficult to observe the ultra-thin monolayer by SEM, but this layer can be justified to be ZnO by chemical analysis such as x-ray photon spectroscopy after removing the PS beads. Later, in the second stage, the ZnO nanorods start to nucleate from the concave regions of PS layers as evidenced from **Figure 5.2(a)**. It was believed that the promotion of heterogeneous nucleation on the concave regions is ascribed to the high affinity of the ZnO nuclei to the ZnO layer under PS beads. To investigate the nucleation behavior of the aligned ZnO nanorods, HRTEM was used to study the interface between ZnO nanorods and ZnO monolayer (~5 nm thicker) shown in **Figure 5.2(d)**after removing the PS beads. It was observed that the well-aligned ZnO nanorods are preferentially nucleated from the concave region in ZnO monolayer. Recently, it was also reported that the aligned ZnO nanorods can be grown on the Si substrates with ZnO nanoparticles or crystalline films as buffered layers **[115]**. After nucleation, in the third period, a preferential growth along longitudinal direction (c-axis) for the oriented ZnO nanorods was expected because the growth in width (or lateral) direction is suppressed due to the size of concave shape in PS layers as shown in **Figure 5.2(b)**. The high resolution TEM image of the well-aligned ZnO nanorods in **Figure 5.2(c)** demonstrates that <001> direction is the preferred growth direction for the well-aligned ZnO nanorods grown on PS/PC substrates. It indicates that the lattice fringes are perpendicular to the longitude direction of the ZnO nanorods, and the singular fringe spacing is about 0.51nm, which is nearly consistent with the *c*-axis parameter in hexagonal ZnO structure (*c*= 0.521nm in Wurtzite ZnO). A detail investigation for the growth behavior of ZnO nanorods grown on inorganic substrates (Si) with ZnO coated can be referred to our previous study **[116]**. This demonstrates that the well-aligned ZnO nanorods can be grown at a lower temperature from aqueous solutions on both organic and inorganic substrates.

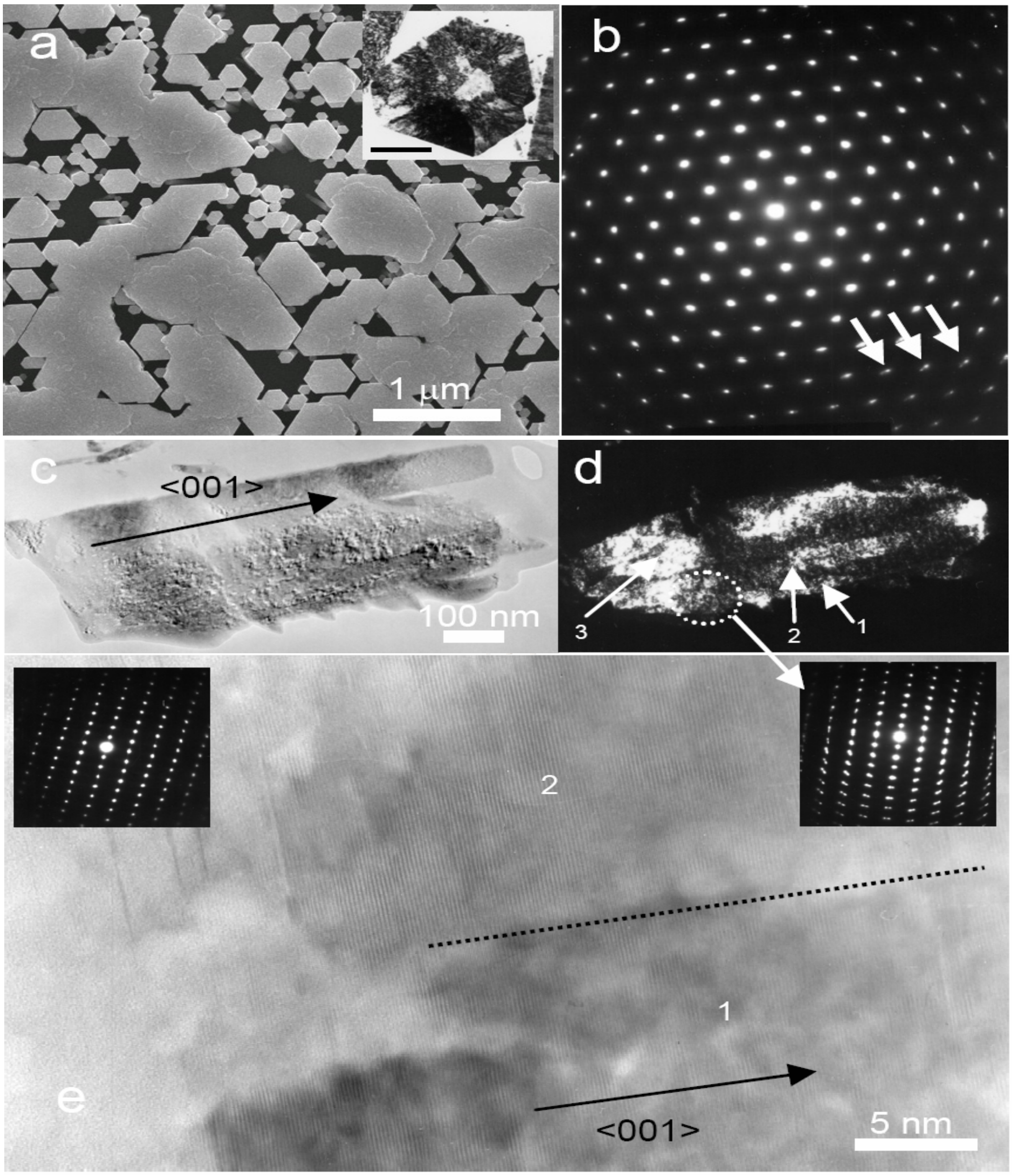

Figure 5.3: (a) Face-on view SEM image of well-aligned ZnO nanorods grown on PS/PC substrates for long-term growth (24 h). A <001> zone-axis TEM bright-field (BF) image of the coalescent ZnO nanorods (its scale bar is 100 nm in the inset), and (b) a corresponding diffraction pattern for the inset of Fig. 3a. (c) Cross-sectional TEM (BF) and (d) dark-field (DF) images of the coalescent ZnO nanorods. (e) A high magnification BF TEM image of (c), showing the interface (marked with dash line) of the coalescent couple ZnO nanorods.

After long-term growth, i.e., 24h, the SEM surface image of ZnO nanorods in **Figure 5.3(a)** reveals that the ZnO nanorods have started on coalescence process with other adjacent nanorods. As compared with **Figure 5.1(a)**, the ZnO rods become much thicker (more than 0.5 μm) in diameter but no more grow longer (about 1.7 μm) in length. Therefore, in this condition, the growth rate of ZnO nanorods in the <001> orientation would obviously decrease. The TEM bright-field (BF) image (inset in **Figure 5.3(a)**) of the (cross-sectional) ZnO nanorods clearly demonstrates the merged grains with side crystal plane attached that can be further confirmed by the <001> zone-axis selected-area electron diffraction (SAED) pattern of ZnO nanorods in **Figure 5.3(b)**. The split diffraction spots in the edge region (marked with arrows) of the SAED pattern suggest that the merged ZnO nanords are not perfectly aligned in both *a* and *b* directions. The TEM BF and dark-field (DF) images of the merged ZnO nanorods in **Figure 5.3(c)** and **(d)**, respectively, clearly shows that more than two ZnO nanorods were aggregated in a coplanar manner using their side planes to form a larger ZnO nanorod. A magnified picture of **Figure 5.3(c)** was illustrated in **Figure 5.3(e)** where the SAED patterns of single and coalescent nanorods are also shown in the left and right insets, respectively. This further explains the coalescence of ZnO nanorods with a slight misalignment between nanorods. Therefore, the growth behavior of the ZnO nanorods in the later long-term growth stage can be considered as a direct combination of a small number of individual nanorods that was similar to oriented attachment **[117]**.

Figure 5.4 illustrates the room-temperature photoluminescence (PL) spectra of the ZnO nanorods grown on PS/PC substrates. For ZnO nanorods grown with a short period of time, i.e. 0.5 h, only a weak PL peak around 378 nm is detected which can be connected to the ultraviolet (UV) emission of ZnO with a bandgap of 3.27 eV. As the ZnO nanorods were grown for 5 h (spectrum b), a strong PL emission at 380 nm, corresponding to the 3.26 eV bandgap transition of ZnO, was detected. However, a broad yellow emission around 575 nm was also observed that is due to the deep levels. The value of the relative PL ratio (Ultraviolet (UV) emission (I_{UV}) to that of deep level emission (I_{DLE})) is estimated to be about ~ 5.1. Generally, the UV emission peak of ZnO is generally attributed to an exciton-related activity **[50,51]**, and the deep level emission may be due to the transitions of native defects such as oxygen vacancies and zinc interstitials **[54,55]**. It is well understood that PL spectra depend on the stoichiometry and the microstructure defects of the materials. As confirmed and reported in our previous results **[117]**, the ZnO nanorods grown in the aqueous solution at a lower temperature may induce unstable surface status to trap impurities and further damage the optical properties. Especially for the ZnO nanorods with a long-term growth, i.e. 24 h, it was observed that the broad orange emission in spectrum c becomes stronger compared to that of ZnO nanorods grown for 5 h (spectrum b). The relative PL ratio ((I_{UV}) / (I_{DLE})) is reduced from 5.1 to 1.2. It is suggested that the native defects due to imperfect boundaries and misalignment between ZnO nanorods were increased for the merged ZnO nanorods. Therefore, it implies that both native defects and optical quality of ZnO nanorods grown on a flexible substrate could be controlled by changing growth conditions.

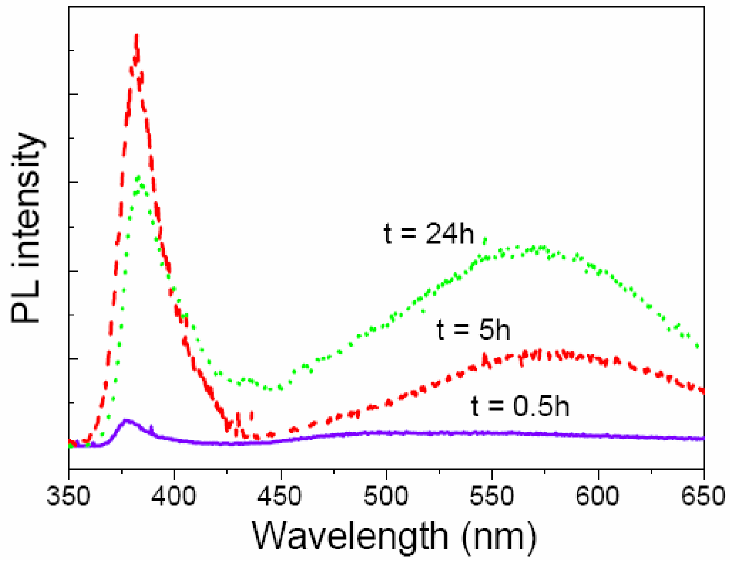

Figure 5.4: Room-temperature PL spectra of ZnO nanorods grown on PS/PC substrates for growth time at 0.5, 5, and 24 h.

5.3 Post-annealing effects on ZnO nanorods

It is well known that both physical characterization and optoelectronic properties are strongly influenced by the defect concentration of native defect in ZnO and this can be modified via thermal treatment under different atmospheres and annealing conditions **[118]**. Therefore, it is important to investigate the effect of post-annealing on the crystallinity and optical properties of ZnO nanorods. The variation of structural and optical properties of ZnO nanorods with thermal annealing conditions will be detailed discussed in this work. **Figure 5.5** plots the room-temperature photoluminescence spectra of the ZnO nanorods annealed under various conditions. Only two emission peaks at 377nm (UV emission) and 595 nm (visible emission) were observed. It was found that UV emission intensities increase with annealing temperature, but the visible emission in post-annealed samples tends to disappear, suggesting that the native defects or non-radiative recombination can be reduced by post-annealing treatment in O_2 and N_2 atmospheres as shown in **Figure 5.5(a)** and **(b)**. However, the ZnO nanorods annealed in N_2 show stronger visible emission peaks compared to that annealed in oxygen atmosphere because the oxygen vacancies become the predominant point defects in N_2 atmosphere. In addition, a unique phenomenon was observed for the sample annealed in H_2/N_2 atmosphere, as presented in **Figure 5.5(c)**. An optimal UV emission occurs at the 600^{o}C. It was believed that H_2/N_2 treatment is able to passivate native defects or impurities that contribute to visible transition, because the hydrogen atoms can be situated in various lattice positions. However, when the sample was exposed to H_2/N_2 at 800^{o}C, the UV emission almost disappeared. This marked change can be attributed to the fact that a high-temperature reduction environment of H_2/N_2 could damage the crystal structure of the ZnO nanorods by surface etching **[119]**. It was also observed that the peak position of the longer-wavelength visible emission band shifts with different treatments. The peak position of the visible (deep-level) emission is related to the predominant defects in the ZnO nanorods and both defects of zinc interstitials and oxygen vacancies are strongly modified by changing annealing temperature and using different atmospheres **[120]**. The relative PL ratios (I_{UV}/I_{DLE}) of the samples as a function of various atmospheres can be further summarized and presented in **Figure 5.6**, revealing that the improvement in the optical quality of post-annealed ZnO nanorods is not only dominated by the annealing temperature but also the annealing atmosphere.

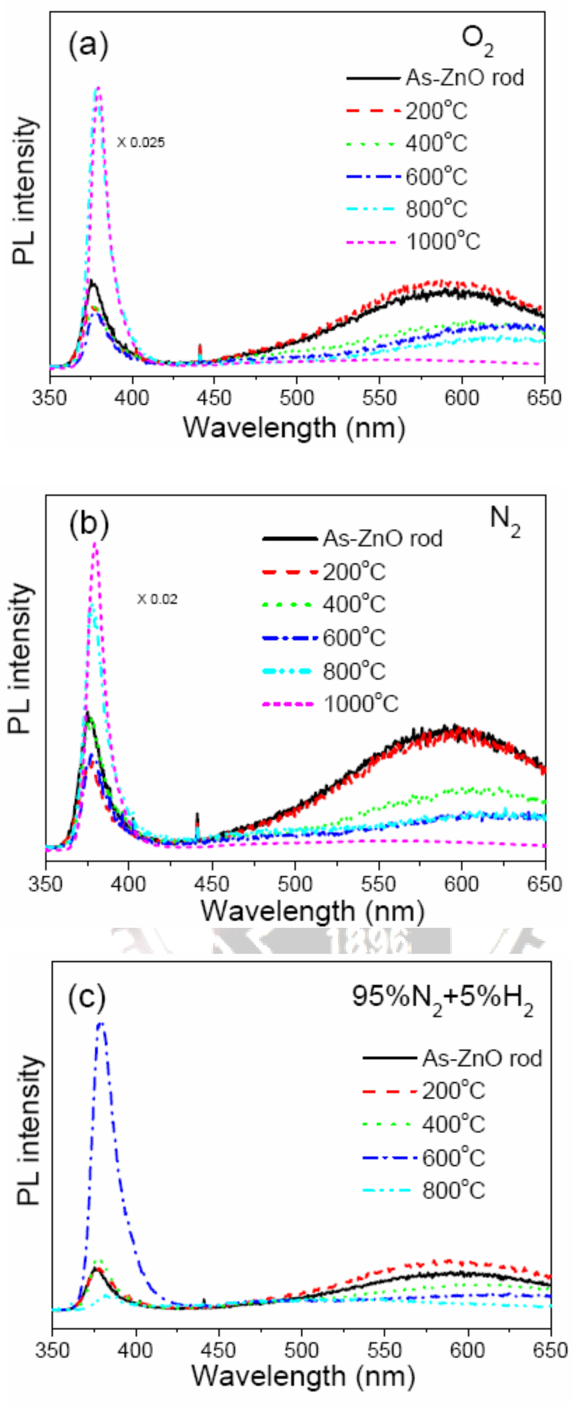

Figure 5.5: Room-temperature PL spectra of ZnO nanorods annealed at various temperatures in (a) O_2, (b) N_2 and (c) H_2/N_2 atmospheres.

Figure 5.7(a) shows that the as-grown ZnO nanorods are perpendicular to the substrate with a uniform length of 900-950 nm. As annealed at 600°C in H_2/N_2, the cross-sectional morphology of the annealed ZnO nanorods in **Figure 5.7(b)** is slightly different from that of the as-grown ZnO nanorods. It was found that the diameter of the annealed ZnO nanorods was locally necked, as shown in the set of **Figure 5.7(b)**. When the ZnO nanorods were annealed at 800˚C in H_2/N_2, the surface image in **Figure 5.7(c)** shows that all the ZnO nanorods were collapsed on the substrate, probably because of surface etching. These results may elucidate why the UV peak was rapidly and suddenly disappeared at 800˚C in **Figure 5.5(c)**. In contrast, as the ZnO nanorods were annealed at 800°C in both O_2 and N_2 atmospheres, the morphology of the ZnO nanorods almost remain unchanged as compared to that of the as-grown ZnO nanorods (**Figure 5.8(a)** and **(c)**). At 1000°C in N_2 and O_2, the surface morphology of ZnO nanorods was changed from "rod-like" to irregular shape as shown in **Figure 5.8(b)** and **(d)**, perhaps because of the melting and re-growth of the nanorods.

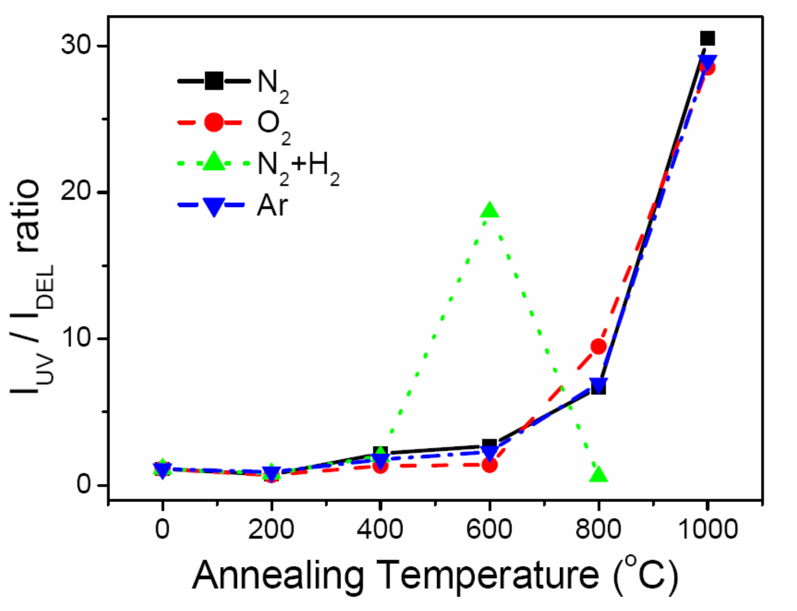

Figure 5.6: I_{UV}/I_{DEL} of the annealed ZnO nanorods dependent on various annealing conditions.

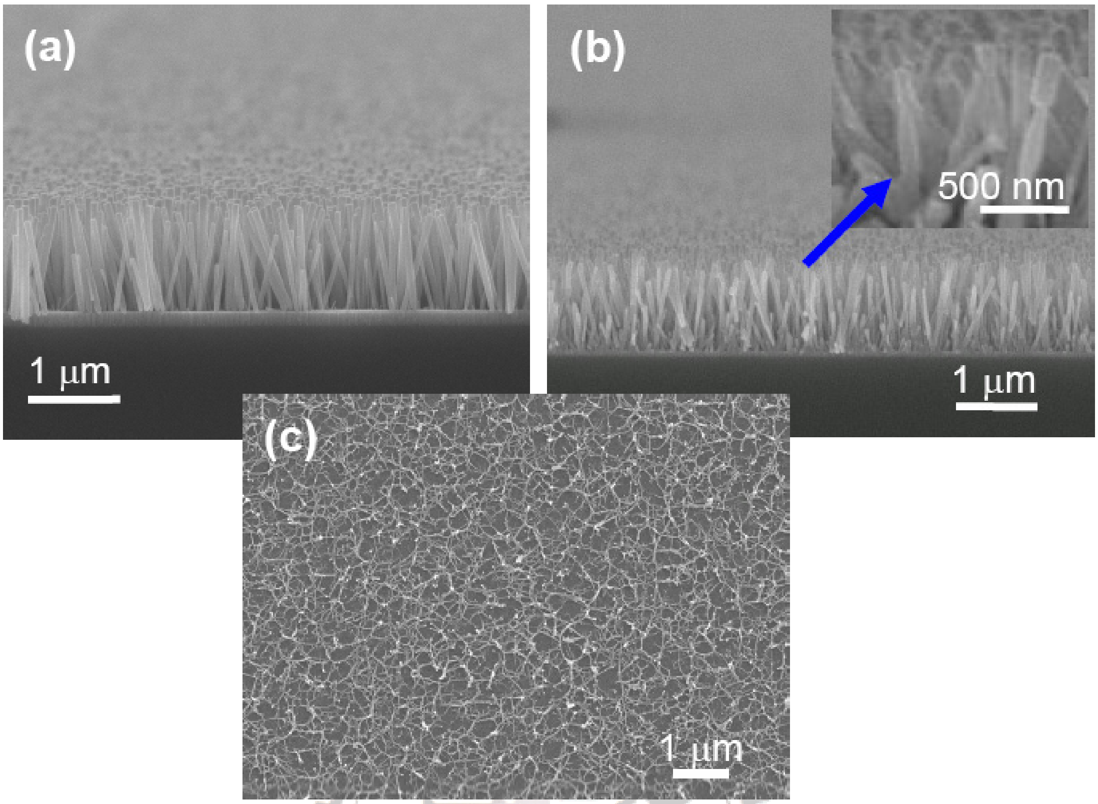

Figure 5.7: SEM images of (a) the as-grown ZnO and annealed ZnO nanorods at (b) 600 °C, (c) 800 °C in H_2/N_2. The inset in Figure 5.7(b) showing the ZnO nanorods become locally necking.

HR-TEM was further used to study the ZnO nanorods annealed at 1000°C in N_2 to elucidate the variation in the local structure. **Figure 5.9(a)** reveals that the ZnO nanorods were shortened to 300-400 nm, and became partially joined to their neighbors. The split diffraction spots in the central region of the SAED pattern suggest that the merged ZnO nanorods are not perfectly aligned in either the *a* (or *b*) and *c* directions, as presented in the inset of **Figure 5.9(b)**. Moreover, HR-TEM images of the ZnO nanorods in **Figure 5.9(c)** demonstrate that partial amorphous was formed in the single-crystal ZnO nanorod. In addition, several lattice fringes (marked with arrows) appear in the edge of the ZnO nanorod in **Figure 5.9(d)**. Furthermore, according to X-ray photoelectron spectroscopy (XPS) analysis, the atomic ratio of O to Zn was approximately to 0.9 for the nanorods and the single of O^{2-} ions in the oxygen-deficient regions were almost covered by the background signal, this indicating these amorphous regions appeared to contain some structural defects. The primary defect type in the region may be considered as oxygen vacancies as evidenced by PL spectra.

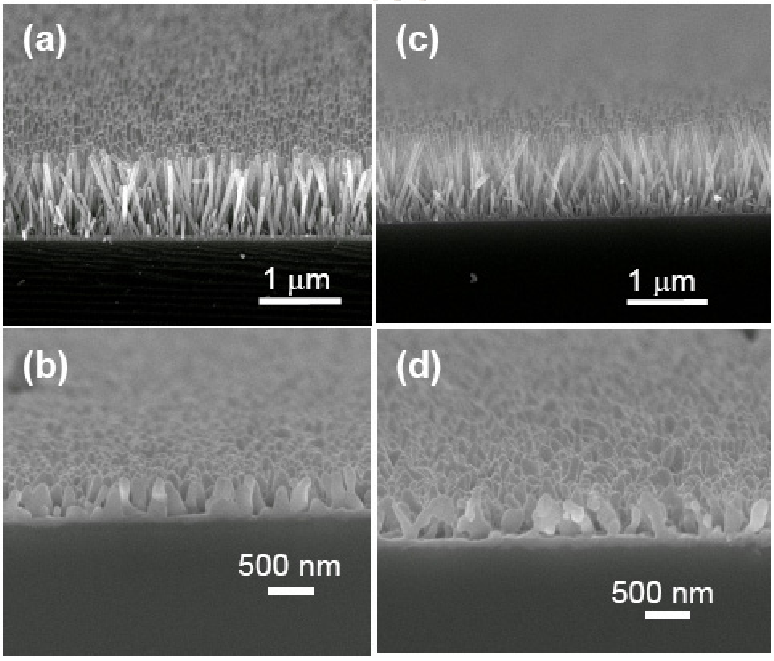

Figure 5.8: SEM images of the annealed ZnO nanorods at (a) 800°C, (b) 1000°C in O_2, and (c) 800°C, (d) 1000°C in N_2.

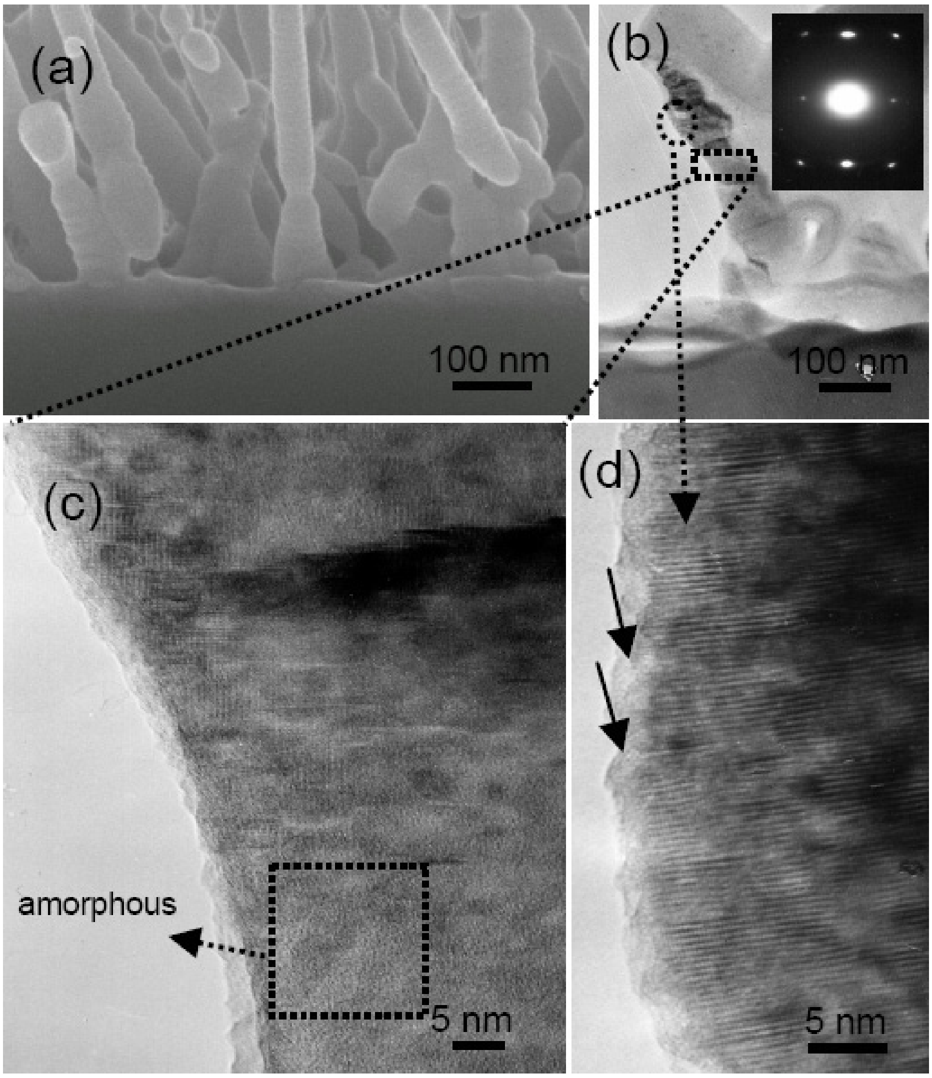

Figure 5.9: (a) High-magnification SEM and (b) low-magnification TEM images of ZnO nanorods annealed at 1000°C in N_2 ambient with a corresponding diffraction pattern in the inset. A high-resolution TEM image of (b), showing the selected area in the (c) neck and (d) top of the ZnO nanorod.

5.4 Summary

We have developed a low-temperature synthetic route to prepare well-aligned arrays of oriented ZnO nanorods in the diameter of ~60 nm on the organic substrates without any extra buffered layer in aqueous solution. HRTEM analysis demonstrates that well-aligned ZnO nanorods are preferentially nucleated from the ZnO monolayer under the concave regions of PS layers. The optical quality of ZnO nanorods grown on a flexible substrate could be improved by controlling growth conditions. This simple approach shows great potential for optoelectronic devices because it can produce large-scale highly well-aligned ZnO nanorods on flexible organic substrates.

In addition, photoluminescence spectra indicate that the optical quality of the ZnO nanorods can be changed and controlled by annealing the ZnO nanorods in various atmospheres at different temperatures. For the sample annealed in both O_2 and N_2 atmospheres, the room-temperature UV emission of the ZnO nanorods increases with the increase of temperature due to the reduction of structure defects. In contrast, in H_2/N_2 atmosphere, a stronger UV emission occurs at 600°C, above that the ZnO nanorods would be collapsed on the substrate and their optical property would be deteriorated by H_2 etching process during a higher temperature annealing treatment. The above-mentioned results may suggest that the crystallinity and optical properties of the ZnO nanorods can be improved by post-annealing treatment.

Chapter 6

Plasma treatment on ZnO nanorods

6.1 Introduction

Although ZnO was reported to be the most potential material to realize the next generation in UV semiconductor laser, most of the ZnO crystal is an *n*-type because it contains significant concentrations of shallow donors and native defects (Zn interstitials, O vacancies). Therefore, the control of defect states becomes an important issue for improvement of emission efficiency. However, unfortunately, most 1D nanomaterials (nanowires or nanorods) have been paraded as “perfect-like” or “defects-free” nanocrystals so that there are rarely efficient methods to fabricate high-quality ZnO nano-scale nanostructures via doping the grown ZnO nanorods at lower temperatures because of no suitable diffusion paths except for in-situ growth of doped-ZnO via vapor-liquid-solid (VLS) process which usually takes place at high temperatures **[121,122]**. But, in our previous studies reveal that the single crystalline ZnO nanorods grown from aqueous solution contain many defects which can provide for the doping or incorporation of impurities into ZnO nanorods **[123]**. Therefore, in this chapter, the reaction between the plasma gas and ZnO nanorods will be discussed.

6.2 High conductivity ZnO nanorods in hydrogen-plasma

Numerous prior investigations have reported that hydrogen ions not only could be more easily diffused into ZnO in the plasma-treated process and combine with other defects to form a shallow donor in ZnO, but also can increase the free electron concentration of ZnO to improve conductivity and strongly passivate the deep level emission to enhance the band edge luminescence. Therefore, in this work, a simple method by combining the aqueous solution process with hydrogen plasma treatment was proposed to develop high-quality well-aligned arrays of ZnO nanorods on organic substrates. **Figure 6.1** shows the SEM images taken from several samples with highly uniform and densely packed arrays of ZnO nanorods grown on flexible four-inch PC substrate (**Figure 6.1(a)**). The ZnO nanorods in **Figure 6.1(b)** present a well-defined hexagonal shape with a homogeneous diameter of approximately ~70 nm. The cross-sectional SEM image in **Figure 6.1(c)** demonstrates that the highly oriented ZnO nanorods with a uniform length of 500-520 nm are perpendicularly grown to the PC substrate. **Figure 6.1(d)** shows the high resolution TEM (HRTEM) image of the well-aligned ZnO nanorods grown on PC substrates with the corresponding selected area electron diffraction pattern shown in the inset. The fringe spacing between two adjacent lattice planes is about 0.52 nm which is nearly consistent with the *c*-axis parameter in hexagonal ZnO structure (c = 0.521 nm in ZnO wurtzite structure), indicating that <001> is the preferred growth direction for the ZnO nanorods. In addition, some stacking faults are also observed (marked with arrows) and these stacking faults seem not to affect the crystal quality of ZnO nanorods because the selected-area electron diffraction pattern in the inset of **Figure 6.1(d)** reveals that the ZnO nanorods still exhibit single crystalline structure.

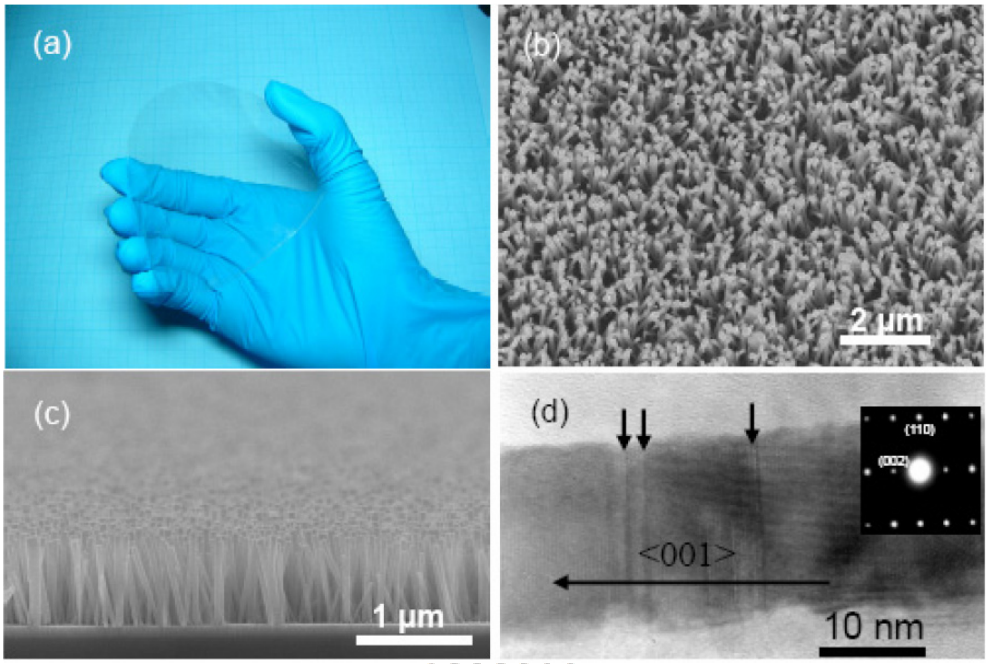

Figure 6.1: SEM images of large arrays of oriented ZnO nanorods grown on polycarbonate (PC) substrates for 8 h. (a) Photograph of the flexible PC grown with arrayed ZnO nanorods. (b) Low magnified top view image of ZnO nanorods. (c) Cross-sectional SEM image of ZnO nanorods grown on PC substrates. (d) High-resolution electron micrograph of ZnO nanorods with the SAED pattern shown in the inset.

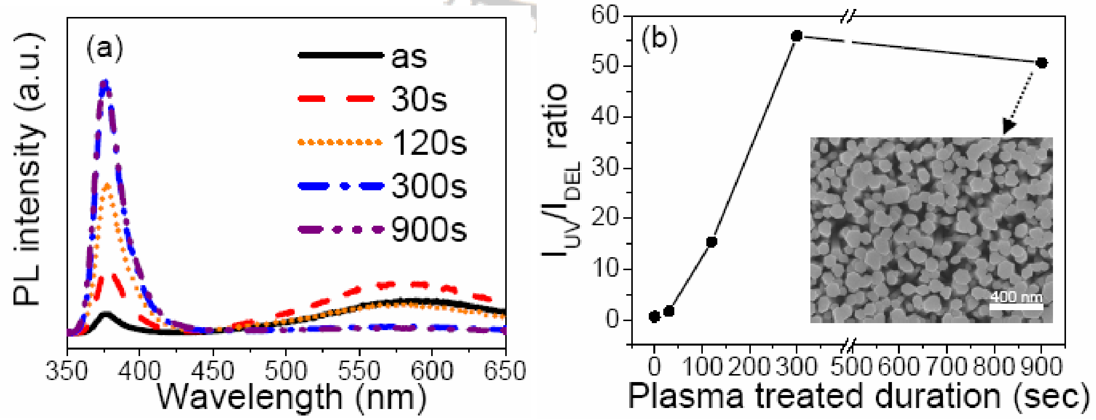

Figure 6.2: (a) PL spectra and (b) I_{UV}/I_{DEL} of ZnO nanorods with and without hydrogen plasma treatment at room temperature. The inset image of (b) shows the FESEM surface morphology of ZnO nanorods with hydrogen plasma treatment of t =900 sec.

Figure 6.2 illustrates the photoluminescence (PL) property of ZnO nanorods at room temperature. As shown in **Figure 6.2(a)**, the PL spectrum of non-plasma ZnO nanorods presents a weak ultraviolet (UV) emission peak at 3.28 eV and a relatively strong deep-level emission peak at 2.10 eV. Similar phenomena are also reported in the related literature **[109,110]**. The UV emission peak of ZnO is generally attributed to the exciton-related activity, and the deep level emission may be due to the transitions of native defects such as oxygen vacancies and zinc interstitials **[54,55]**. In addition, the imperfect boundaries and stacking faults of ZnO nanorods would cause the unstable surface status to trap impurities and further damage the optical property, especially as the diameter of ZnO nanorods was down to nano-scale. It was believed that those induced defects are probably related to the fast growth of the ZnO nanorods in the aqueous solution. In contrast, with the hydrogen plasma treatment, all the ZnO nanorods show much better PL property than that of non-plasma sample and the deep level emission was almost covered by the background signal in all plasma-treated samples. It was believed that the native defects or impurities contributing to visible transition can be passivated by H_2 plasma treatment, because the hydrogen atoms can be situated in various lattices positions and the most presumably stable position is the H configured at Zn-O bond center, which acts as a shallow donor.**[ref-22]** Similar observations for the passivation of hydrogen plasma treatment on the visible emission of ZnO are also reported **[124]**. **Figure 6.2(b)** illustrates the ratio of peak intensity of Ultraviolet (UV) emission (I_{UV}) to that of deep level emission (I_{DLE}). The value of the relative PL ratio increases with the increase of plasma treatment duration up to 300 sec in all the samples and then becomes slightly decreased. A higher PL ratio implies that the plasma-treated ZnO nanorods exhibit higher optical quality. Moreover, it can be clearly observed that the crystal morphology of vertically well-aligned ZnO nanorods seems not to be affected by a lengthy plasma treatment even at 900 sec as revealed by the SEM images in the set of **Figure 6.2(b)**.

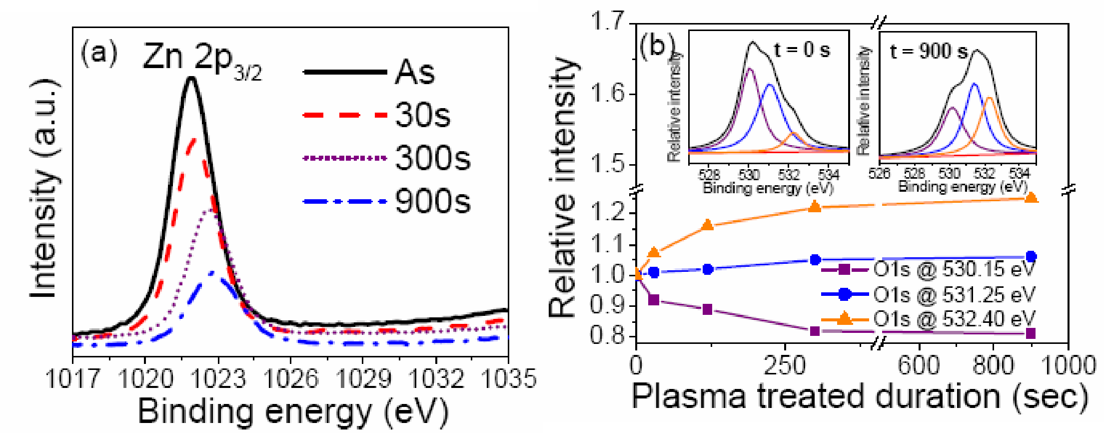

Figure 6.3: (a) Zn 2p spectra obtained from the ZnO nanorods with and without hydrogen plasma treatment. (b) Dependence of relative intensity ratio (O1s) of three fitted components centered at 530.15, 531.25, and 532.40 eV for the ZnO nanorods with and without hydrogen plasma treatment.

Figure 6.3 shows the XPS core level spectra taken from the ZnO nanorods surface after the plasma treatment in H_2. As compared with the non-plasma sample, **Figure 6.3 (a)** illustrates that the peak shift of 0.2-0.3 eV toward higher binding energies was observed in Zn 2p spectrum for H_2 plasma-treated ZnO nanorods. This peak shift indicates the reduction of the surface band bending and this may be related to the doping or incorporation of H ions into ZnO nanorods **[125]**. Thus, the H_2 plasma treatment seems to partially recover or reduce surface defects, leading to the decrease of densities of surface states on ZnO nanorods. However, as the ZnO nanorods were treated with H_2-plasma duration more than 300 sec, the Zn 2p peak is shifted toward a higher binding energy around 0.5-0.8 eV. This phenomenon reveals that the surface band bending of ZnO nanorods was slightly changed by H_2 plasma treatment. Moreover, in comparison with non-plasma sample, the intensity of Zn 2p peak would decrease with the increase of the plasma duration. It might imply that local fine structure of ZnO nanorods could be changed and thus, more native defects were induced to raise the intensity of deep level emission. However, this phenomenon was not observed in our study. Therefore, it can be inferred that hydrogen plasma treatment might passivate these defect centers to suppress the deep level emission.

In addition, the O1s peak presents different feature for the samples treated with various duration of hydrogen plasma as one can see in **Figure 6.3 (b)**. The typical O1s peak can be consistently fitted by three nearly Gaussian, centered at 530.15, 531.25, and 532.40 eV, respectively. Generally, the high binding energy component located at 532.40 is usually attributed to O-H bonds **[126]** which could be attributed to the absorbed hydrogen ions during the plasma treatment of ZnO nanorods. Furthermore, it can be observed that the peak intensity at high binding energy would increase as increasing plasma duration up to 300s and then it gets saturated. It indicates that hydrogen plasma treatment could efficiently modify the surface states of ZnO nanorods by absorbing the hydrogen ions to reduce the unstable dangling bonds on the surface region of ZnO nanorods. **Figure 6.3(b)** also shows the variation of the medium binding energy component of O1s peak (centered at 531.25 eV) with plasma duration. The peak is generally associated with O^{2-} ions in oxygen deficient regions within the matrix of ZnO. It was observed that the peak intensity of this component does not obviously change with hydrogen plasma treatment. This indicates that the oxygen vacancies can not be reduced by H_2-plasma treatment to improve the optical properties in ZnO nanorods. To further understand the importance of hydrogen plasma treatment on the passivation effects of ZnO nanorods, the H_2-plasma samples were further annealed at various temperatures in nitrogen atmosphere. (Note: the post-annealed specimen were grown on Si substrate and then treated by hydrogen plasma at the same conditions as that grown on the flexible substrates.) It was found that the relative PL ratio would decrease drastically while the samples were annealed more than 400^{o}C, as shown in **Figure 6.4**. Furthermore, the PL spectrum of the post-annealed ZnO nanorods was almost restored to that of original ZnO nanorods (ZnO nanorods without H_2 plasma treated). This implies that surface absorption and doping effects of hydrogen ions on ZnO nanorods can be recovered by thermal annealing process. Therefore, it can be concluded that both defect passivation and modification of surface state on hydrogen-plasma ZnO nanorods are responsible for the enhanced optical properties.

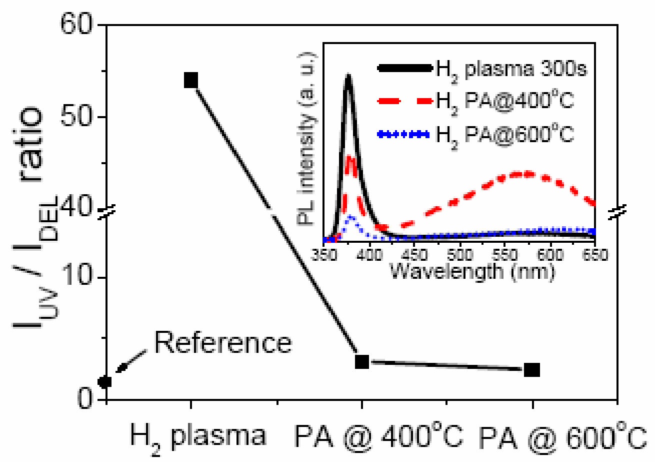

Figure 6.4: I_{UV}/I_{DEL} of ZnO nanorods (grown on ZnO film/ Si substrate) with hydrogen-plasma for 300 sec and then annealed at 400, and 600°C (PA@400 and PA@600 °C). The corresponding PL spectra of ZnO nanorods were shown in the inset.

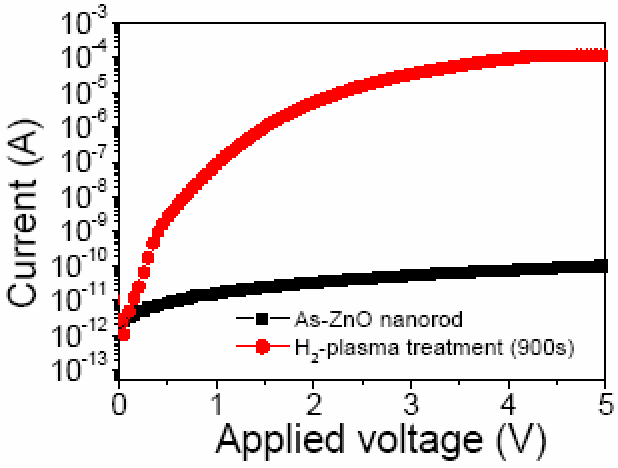

Figure 6.5: Comparison of *I-V* curves for the ZnO nanorods with and without H_2-plasma treated.

Figure 6.5 shows the *I-V* curve for a homojunction of *n*-type ZnO nanorods (treated by H_2 plasma duration of 900 sec) on n-type ZnO films. The structure of In metal/ZnO nanorods/ZnO films/In metal/PC substrate was used for the I-V measurement of ZnO nanorods. It was found that the non-plasma ZnO nanorods present a higher resistivity about hundreds of MΩ, which is about 2 orders of magnitude larger than that reported in the literature for the naked single ZnO nanowire (above 3.5 MΩ). In contrast, when the ZnO nanorods undergo hydrogen plasma treatment over than 300 sec, the resistivity of ZnO nanorods decrease by typically 5-6 orders of magnitude. It suggests that hydrogen plasma can efficiently raise the free electron concentration and increase the conductivity of ZnO nanorods. The above results reveal that with the H_2–plasma treatment on ZnO nanorods, both optical and electrical properties could be substantially improved and increased. This implies that incorporating hydrogen into ZnO nanorods not only passivates the native defects but also acts as a shallow donor to improve the conductivity.

6.3 Rectifying behavior of ZnO nanorods by ammonia-plasma

The ZnO nanorods present single crystalline structure and a well-defined hexagonal plane with a homogeneous diameter of approximately 60-70 nm. The cross-sectional scanning electron microcopy (SEM) image in **Figure 6.6(a)** shows that the highly oriented ZnO nanorods with a uniform length of 500-520 nm are perpendicularly grown to the substrate. In addition, it was found that by controlling the experimental conditions, highly arrayed ZnO nanorods or nanowires with different aspect ratios can be grown from the chemical aqueous solution **[116]**. A close observation on the microstructure of the ZnO nanorods, as show in **Figure 6.6(b)**, reveals that the surface morphology of ZnO nanorods shows a waved shape structure with 0.5 ~ 1 nm roughnesses. In addition, some stacking faults are also observed (marked with arrows). However, these small surface roughness and stacking faults seem not to affect the crystal quality of ZnO nanorods because the selected-area electron diffraction pattern in the inset of **Figure 6.6(b)** reveals that the ZnO nanorods still exhibit a single crystalline structure. **Figure 6.6(b)** clearly describes the perpendicular directional growth of the ZnO nanorods where the singular fringes spacing is about 0.51nm, which is nearly consistent with the *c*-axis parameter in hexagonal ZnO structure (c = 0.521 nm in ZnO wurtzite structure), indicating that <001> is the preferred growth direction for the ZnO nanorods, in consistence with XRD patterns that shows a single strong ZnO (002) peak at $2\theta = 34.4^{o}$ **(not shown here)**.

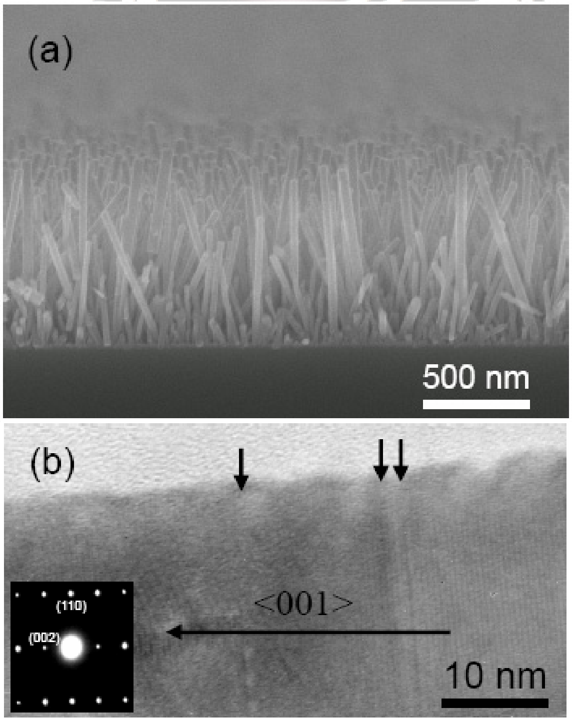

Figure 6.6: Cross-sectional scanning electron microcopy (SEM) micrograph of (a) ZnO nanorods/ZnO film/Si, (b) surface microstructure and stacking faults (marked with arrows) of ZnO nanorods. The inset image of (b) displays SAED pattern.

Figure 6.7(a) illustrates the photoluminescence (PL) property of ZnO nanorods at room temperature. The PL spectrum of non-plasma ZnO nanorods presents a weak ultraviolet (UV) emission peak at 3.28 eV and a relatively strong deep-level emission peak at 2.10 eV. The UV emission peak of ZnO is generally attributed to an exciton-related activity **[1]**, and the deep level emission may be due to the transitions of native defects such as oxygen vacancies and zinc interstitials. In addition, the imperfect boundaries in ZnO nanorods would cause the unstable surface status to trap impurities and further damage the optical property, especially for the nano-scale ZnO nanorods. In contrast, it was found that the peak intensity of the UV emission increases with the plasma duration up to 90 sec but the deep level emission in all plasma-treated samples tends to disappear, indicating that the native defects or impurities, contributing to visible transition, can be much reduced by NH_3 plasma treatment. As shown in **Figure 6.7(b)**, a maximum relative PL ratio (peak intensity of ultraviolet emission (I_{UV}) to that of deep level emission (I_{DLE})) shows up around 90-120 sec, implying that the plasma-treated ZnO nanorods exhibit much better PL properties than that of non-plasma sample. The improvement in the optical properties of ZnO nanorods with the plasma treatment may be attributed to the reduction of the defect concentration due to the occupation of N ions on the defect sites, i.e., oxygen vacancies, which will be further elucidated later. However, a further increase in plasma duration such as 180 sec would result in the decrease in the relative PL ratio that is probably related to the plasma etching as revealed by the SEM image in **Figure 6.7(c)** where the ZnO nanorods were deteriorated that is in contrast to the ZnO nanorods with the plasma-treated duration less than 90 sec, well-aligned ZnO nanorods with well-defined hexagonal plane remains unchanged with an average length of 500 nm, similar to that without NH_3 plasma treatment.

Figure 6.8 shows the relative intensity ratio of internal N (N_i) to surface N (N_f)

dependent on etching time for the ZnO nanorods with NH_3 plasma treatment. No nitrogen signal was detected in the reference sample [see the inset of **Figure 6.8(a)**] but the N1s peak could be detected in plasma-treated ZnO nanorods from surface to internal region for the ZnO nanorods (duration at 90 sec). **(**Note: The N1s (~401 eV) internal signal was obtained by following the measurement steps. Firstly, ZnO nanorods were etched by Ar ion source and then the N1s signal of the etched ZnO nanorods can be detected. Next, both intensities of N1s signal (401 eV) for etched and non-etched nanorods were compared and considered as the internal and surface signals, respectively.) In addition, **Figure 6.8 (b)** illustrates the peak shift of 0.2-0.6 eV toward higher binding energies in Zn 2p spectrum for NH_3 plasma-treated ZnO nanorods as compared to that of the reference sample. This peak shift indicates the reduction of the surface band bending **[125]** and this may be related to the doping or incorporation of N ions into ZnO nanorods. The doped N atom could have the probability to occupy O sites to form the acceptor (N_O) in ZnO nanorods. Thus, the NH_3 plasma treatment seems to reduce the densities of the surface defects (**Figure 6.6(b)**) on ZnO nanorods. However, it was also observed in the inset of **Figure 6.8(b)** that as the ZnO nanorods were NH_3-plasma treated more than 180 sec, the Zn 2p peak is shifted toward a higher binding energy around 4-5 eV. This phenomenon implies that the surface band bending of the ZnO nanorods was strongly influenced by NH_3 plasma treatment and therefore, the structure morphology of ZnO nanorods would be probably changed as shown in **Figure 6.7(c)**.

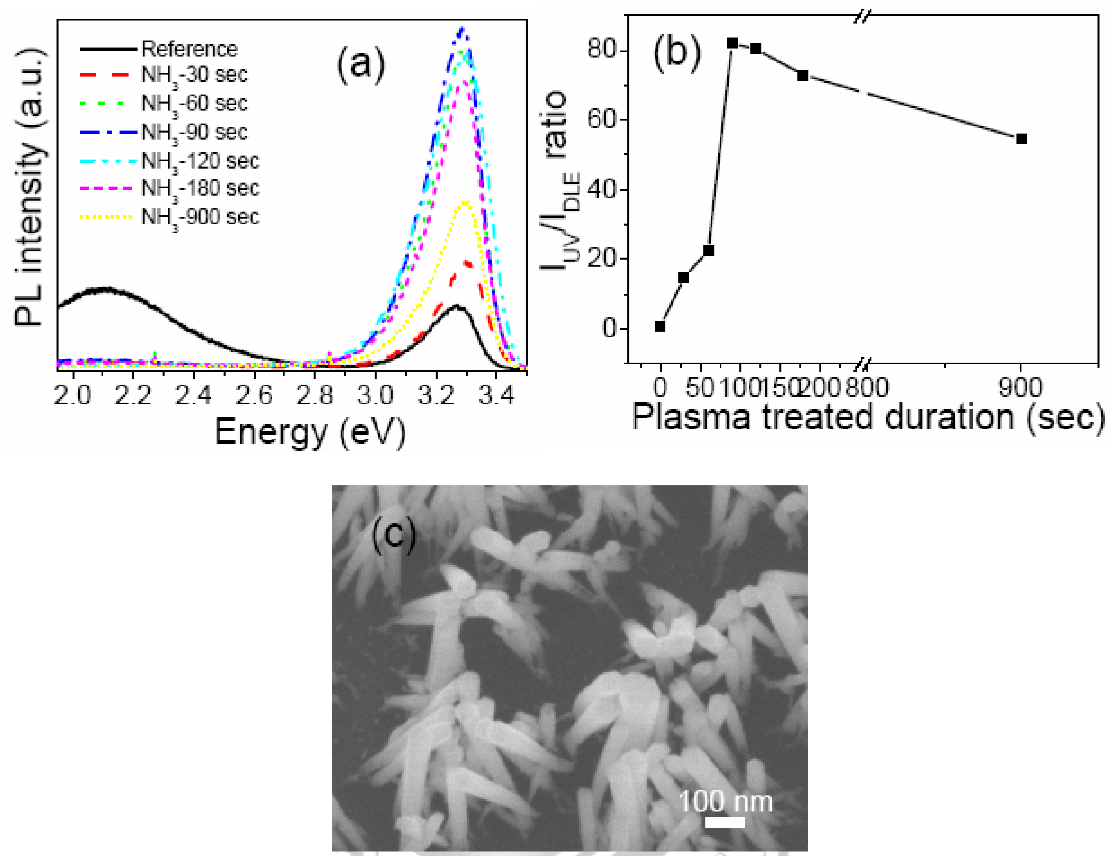

Figure 6.7: (a) Room-temperature PL spectra and (b) PL ratio of I_{UV}/I_{DEL} for ZnO nanorods with and without NH_3 plasma treatment. (c) The FESEM surface morphology of ZnO nanorods with NH_3 plasma treatment of t =180 sec.

Based on the above discussion, a mechanism for the formation of p-type ZnO nanorods under NH_3-plasma treatment is tentatively proposed as follows. As we can see in **Figure 6.6(b)**, imperfect boundaries (surface roughness) and many defects (stacking faults) were observed in the ZnO nanorods where N and H radicals (ions) can be easily doped into ZnO nanorods by thermal diffusion via the nature defect routes. In general, the H ions are more easily diffused into ZnO than N ions in the plasma-treated process and can combine with other defects to form a shallow donor in ZnO. However, according to the PL analysis, it was found that the luminescence properties were enhanced with the increase of plasma-treated duration up to 90 sec, indicating that the incorporation of H into ZnO nanorods does not show negative influence on the optical properties of ZnO nanorods in such short plasma duration. In other words, the improvement in optical property of ZnO nanorods can be primarily attributed to the reduction in surface defects and defect concentration of ZnO nanorods due to the occupation of N ions on the defect sites **[127]**. However, a long NH_3-Plasma treatment over 180 sec not only causes the plasma etching but also promotes the diffusion of H ions into the ZnO nanorods as well as increases the concentration of shallow donors to restrict the formation of p-type ZnO.

Figure 6.9 shows the I-V curve for a homojunction of *p*-type ZnO nanorods (treated by NH_3 plasma duration of 90 sec) on *n*-type ZnO films. The graph in the inset of **Figure 6.9** shows surface I-V characteristics using In and Au/In electrodes on both *n*- and *p*-type ZnO. For the linear dependences of I-V characteristics, the ohmic contacts are fairly confirmed. Rectification by *p*-*n* junction is clearly displayed. The threshold voltage appears at 1.5 V under forward bias and it is almost half of the band gap energy of ZnO. It was also found that the I-V curve presents a little leakage current in reverse bias and this could be due to incomplete contact between some nanorods and contact metal electrode. Further experiments are required to understand the possible origin of the rectifying behavior with such a smaller threshold voltage. Nevertheless, the I-V characteristics of nitrogen-doped ZnO nanorods supports that the current approach is a valuable one to fabricate ZnO nanorods for *p*-*n* junction device application.

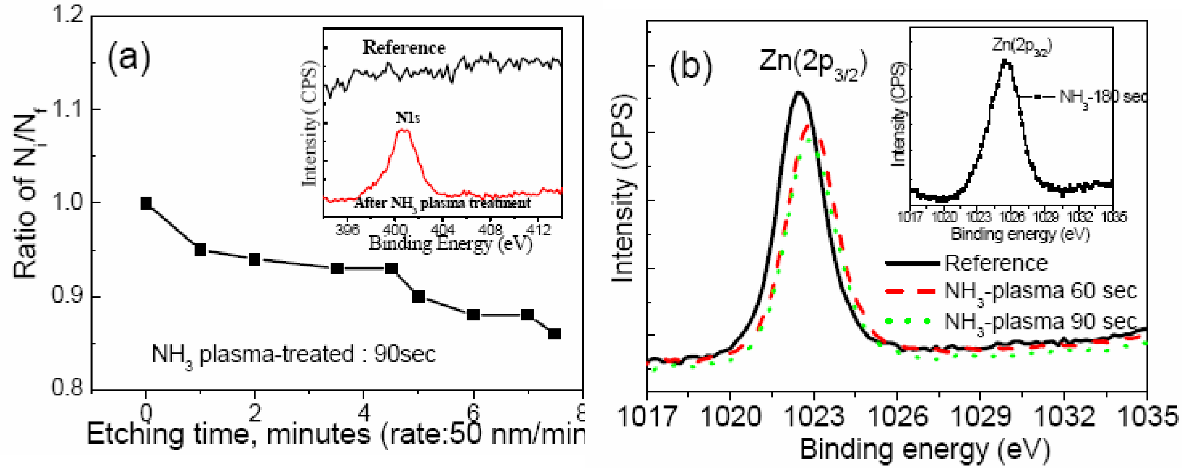

Figure 6.8: (a) Dependence of relative intensity ratio of internal N (N_i) to surface N (N_f) on etching time for the ZnO nanorods with the inset showing the N1s spectra obtained from the ZnO nanorods with and without NH_3 plasma treatment (t= 90 sec). (b) Zn 2p spectra obtained from the ZnO nanorods with and without NH_3 plasma treatment. The inset shows the Zn 2p3/2 spectra of ZnO nanorods with NH_3 plasma treatment of t=180 sec.

6.4 Summary

We have developed well-aligned arrays ZnO nanorods on four-inch PC organic substrates buffered with ZnO film by combining a simple chemical solution at low temperatures with H_2 plasma treatment. The photoluminescence spectra indicate that the optical quality of the ZnO nanorods can be much improved by H_2 plasma treatment as evidenced by the remarkable increase in the ultraviolet emission intensity. The I-V results suggest that *n*-type ZnO nanorods with a higher conductivity can be obtained by combining the chemical solution process with hydrogen plasma treatment.

The XPS analysis shows that the nitrogen ions can be doped into ZnO nanorods through surface adsorption or defect routes under NH_3 plasma treatment. The native defects of the ZnO nanorods can be effectively reduced and the optical property can be much improved. Moreover, the electrical transport data reveal that *p*-type ZnO nanorods with a smaller threshold voltage of 1.5 V can be obtained by combining the chemical solution process with NH_3 plasma treatment.

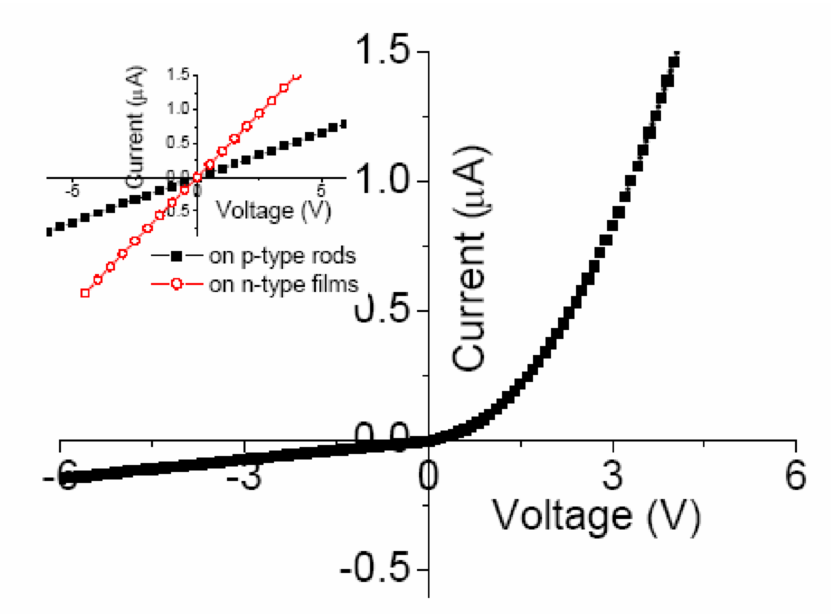

Figure 6.9: I-V curves for a *p*-*n* homojunction formed by *p*-type ZnO nanorods grown on *n*-type ZnO films. Inset show the Ohmic contacts on *n*-type and *p*-type ZnO.

Chapter 7

One dimensional ZnO and carbon nanotube (CNT) composite

7.1 Introduction

Semiconductor nanoparticles have been widely investigated from fundamental and applied research viewpoints, owing to their potential in photocatalysis, solar energy conversion, and optoelectronic applications **[128-135]**. The assembly of isotropic nanoparticles onto one-dimensional architecture represents an important step towards the integration of nanoparticles into nanodevices **[136]**. Particularly, nanoparticles can be assembled on 1D nanostructure of a different material to form novel and interesting composite nanomaterial system **[137]**. Single-walled carbon nanotubes (SWNTs), due to their excellent structural and electronic properties, is the one of the most potential 1D nanostructures in the past few years **[138,139]**. To achieve multifunctional nanodevices, many research groups have developed several methods to coat metal and semiconductor nanoparticles, such as Au, Ag, SnO_2, TiO_2, SiO_2, and Al_2O_3, on carbon nanotubes (CNTs) **[140-145]**. Moreover, some of coated CNT composite system have been demonstrated that their original physical properties would be improved after coating specific nanoparticles **[146,147]**. Zinc oxide (ZnO), wide band-gap semiconductor (3.4 eV) with a large exciton binding energy (60 meV), has been extensively investigated because of its excellent performance in sensors and optoelectronics systems **[15,72]**. There are several methods to fabricate ZnO clusters and nanoparticles on nanostructures **[148,149]**. To date, there are few reports on assembling the composite from CNTs and ZnO. Zhu et al **[150]**. and Ravindran et al **[151]**. have reported the coating of ZnO nanoparticles on multi-walled carbon nanotubes (MWCNTs) by sputtering and electrostatic coordination approach, respectively. However, form above results showed it is difficult to form a continuous layer on CNTs, even in MWCNTs. Hence, the coating behaviors and mechanisms on CNTs need to be further investigated.

In this chapter, we will present the fabrication of ZnO-coated SWNTs either as buckypaper or as individual tubes at low temperature via ultrasound irradiation of oxidative SWNTs, zinc acetate, and triethanolamin in aqueous solution. The successful formation of ZnO layer on SWNTs has been confirmed using atomic force microscopy (AFM), scanning transmission electron microscopy (STEM), and electron transport measurement. Finally, we will show the photoconductivity properties of individual ZnO nanorod device to compare with composite materials.

7.2 Synthesis and characterization of ZnO-SWNT composite

SWNTs produced by Hipco method were obtained from Rice University. These nanotubes were sonicated in nitride acid (HNO_3) for 10 min. This treatment is known to produce shortened nanotubes and to also create defects on side-walls, both of which are capable of being terminated by carboxyl and hydroxyl groups in the presence of oxidizing acid. The schematic representation for the fabrication of SWNTs and ZnO composite is shown in **Figure 7.1**. After oxidizing treatment, the SWNTs were dispersed into 20 mL aqueous solution; then the solution containing SWNTs was heat to 95°C with intense ultrasonic waves. And then, 0.005 mol/L zinc acetate and 1.5 mol/L triethanolamine (TEOH) were dropped smoothly into the SWNTs aqueous solution. In typical experiment, the system was continuously stirred with ultrasonic waves for 2 h at 95°C. The thickness of the coating can be adjusted by changing the reaction time and the concentration of zinc acetate. For the transport measurement, individual SWNT and SWNT@ZnO were positioned on top to bridge two noble metal electrodes (Au-Pd), which acts as the source and drain. The electrodes were deposited on top of a SiO2 layer on a silicon substrate, and the silicon was used as the gate.

According to our pervious study, the average diameter of pristine SWNTs was about 1.2 nm. After coating process, the average height of SWNTs increased to 8 nm, which means there could be a ZnO layer about 7 nm thick on SWNTs. To confirm the ZnO layer was around on SWNTs, the chip was heated at 500 and 600°C in air for 30 min. Generally, pristine SWNTs will be burned out and disappeared. In AFM image (**Figure 7.2**), it was found that the same area reveals linear features formed at the positions of SWNTs after the chip was burned. The insert image shows that surface morphology of coating SWNTs after 500°C heating in air. We have observed some crystalline structure at the same region of SWNTs, and we proposed this crystalline behavior is due to the higher heating temperature transfer amorphous ZnO layer to poly-crystalline ZnO.

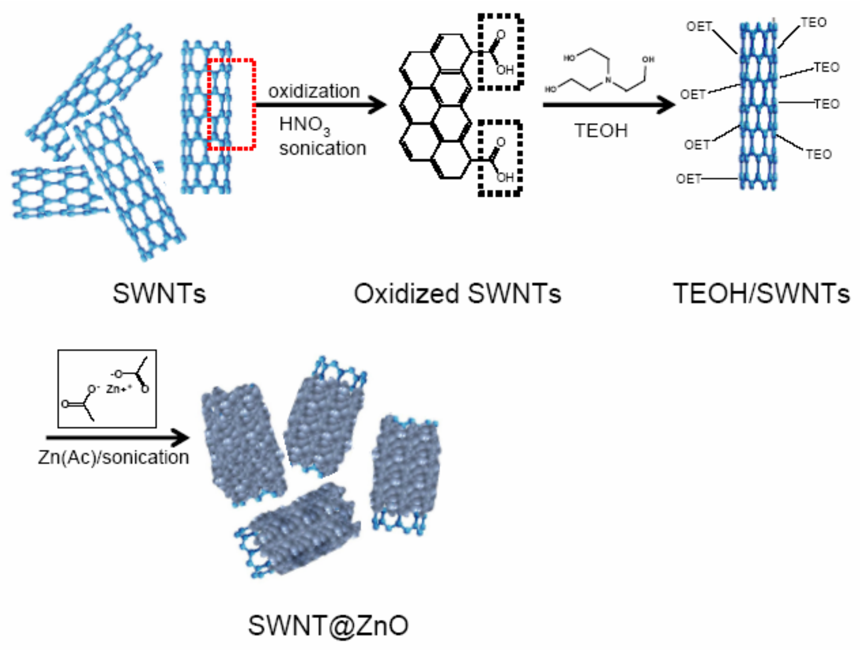

Figure 7.1 The schematic representation for the fabrication of SWNTs and ZnO composite.

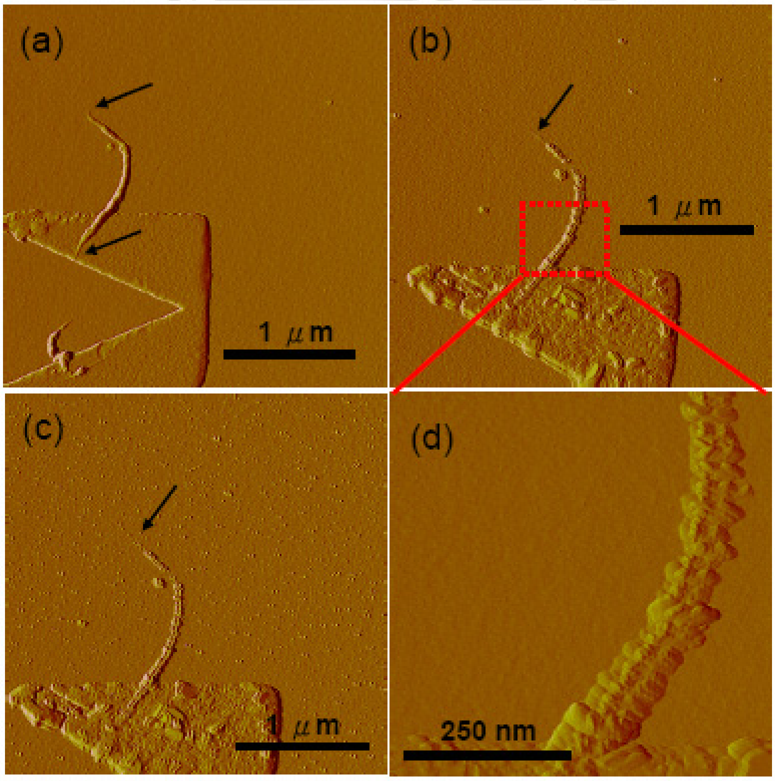

Figure 7.2 AFM images of SWNT@ZnO. (a) Before heating, (b) heating at 500^{o}C, (c) at 600^{o}C in air 40 min, and (d) high magnification of (b).

The ZnO coating studies have been complemented by micro Raman spectroscopy on the individual SWNTs and bucky-paper after coating process, as shown in **Figure 7.3**. The main features in the Raman spectra of SWNTs are the radial breathing mode (RBM) which is in the frequency range up to 200 cm^{-1}, G-line around 1600 cm^{-1} from the tangential vibrations of the carbon atoms, and the D-line at 1280 cm^{-1}. The intensity of the D-line is related to the amount of sp^3 defects on carbon nanotubes. Therefore, we suggested that the intensity of D-line increased is due to SWNTs were treated with nitric acid to create surface function group. Moreover, we found the Raman spectrum of SWNT@ZnO shows slow decrease and slight shift in the RBM intensity in individual nanotubes. In addition, it was found all Raman signals shifted toward low frequency about 2-5 cm^{-1}, in the Raman spectra of SWNT@ZnO bucky-paper materials, RBM peak especially (~5 cm^{-1}). We proposed the signals decrease was related to possible scattering and these peaks shift was contributed by the chemical interaction between carbon atom and TEOH-Zn, respectively. In order to demonstrate our contention, we evaporated 20 nm silicon monoxides to cover the individual SWNTs on chip and than measured by Raman spectroscopy. A similar quenching of the Raman signals occurs if a thick layer covered around SWNTs. However, within this SWNTs-SiO_x experiment, no shift in the Raman frequencies was observable. It means that only van der waal interaction between silicon monoxide and SWNTs, therefore, only scattering effect could be detected.

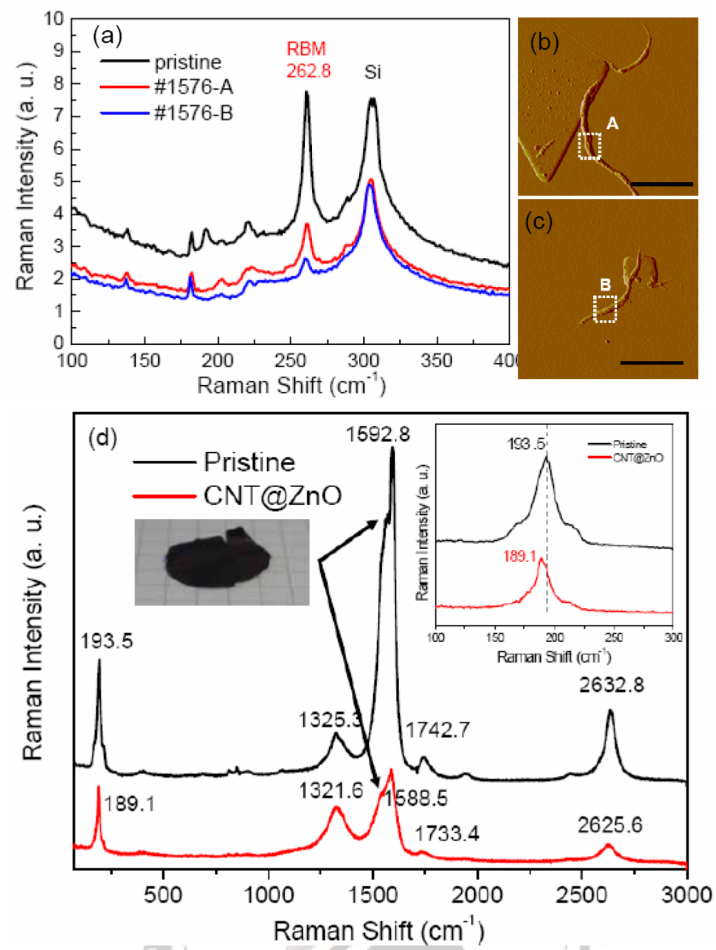

Figure 7.3 **(a)** Micro Raman spectroscopy on the individual SWNTs with and without ZnO coated. Laser spot was focused coated SWNTs as shown in AFM images (b) and (c). (d) Bucky-paper material was also measured by the same Raman system.

Figure 7.4 shows a transmission electron microscopy (TEM) image of coated SWNTs. The image presents the coating of nanotubes with a thin layer of non-crystalline material. In order to confirm this thin non-crystalline layer, energy-dispersive x-ray measurements made on a VG501 scanning TEM was used to analyze the element composition. The EDS spectrum shown in **Figure 7.4b** was obtained with an electron beam spot size of 1.0 nm and the beam with this spot size is focused directly in the coated SWNTs to get the spectrum. The Zn, O, and a significant carbon peaks could be clearly obtained by long time detecting.

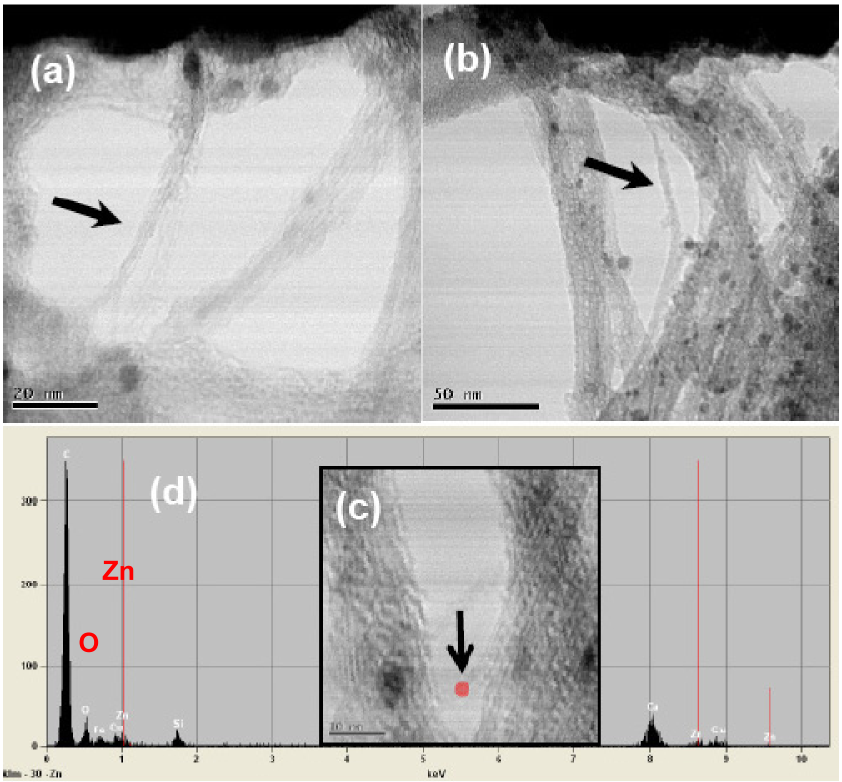

Figure 7.4 (a) and (b) show the low magnification TEM images of SWNT@ZnO. The high magnification TEM image with EDS elements mapping were shown in (c) and (d).

7.3 Electrical transport in individual core-shell nanotube

For the electrical transport measurement, the coating SWNTs were deposited on a degenerately doped silicon substrate with a thermally grown SiO_2 layer. Afterward Au/Pd electrodes were applied in two probe configuration by standard e-beam lithography. In our transport studies on SWNTs@ZnO, we have measured many individual tubes with ultraviolet (UV) light on them at room temperature. **Figure 7.5a** presents a set of Isd-Vg curves obtained from a typical device made by pristine

SWNTs and these pristine SWNTs showed *p*-type FET characteristics. During the measurement of I_{sd}, while we shined the UV light on the device, the current would slight decrease from $5x10^{-8}$ to $3x10^{-8}$ A. This phenomenon was called “photoinduced conductivity” and has been discussed by two research groups **[152,153]**. According to former articles, the photoinduced conductivity in the pristine SWNTs maybe due to (i) hot electrons attach to adsorbed molecules to induce desorption or (ii) contact electrodes were oxidized to change the barrier between electrode and SWNTs by UV light. In the (i) case, it should be difficult observed on metallic nanotubes because of large Isd current could not easy compensate by photoinduced effect. Additionally, if photoinduced conductivity was from contact electrodes oxidized, the device should be not reproducible because of electrodes were hard to recover as original one. However, we also could observe the similar transport characteristics on the coated SWNTs with UV light. For the coated SWNTs, firstly we have measured the Isd as the Vg changes from -5.0 to 5.0 V. As a result, some of the coated SWNTs exhibit distinct p-type characteristics and other tubes show metallic behavior. No matter ZnO coated on semiconductor or metallic SWNTs, we can easy observe the Isd current decrease drastically while shining the UV light on device. We suggest that current reduction behavior in coated nanotubes is a non-thermal process and is attributed by electronic compensation. As the UV excited the electron to conduction band, it will create some holes carrier at the ground state. At the same time, the electrons transported through the SWNTs will be compensated by the ground state hole carrier to reduce current. If we turned off the UV light, the e-h compensation behavior would disappear and than the current will increase again.

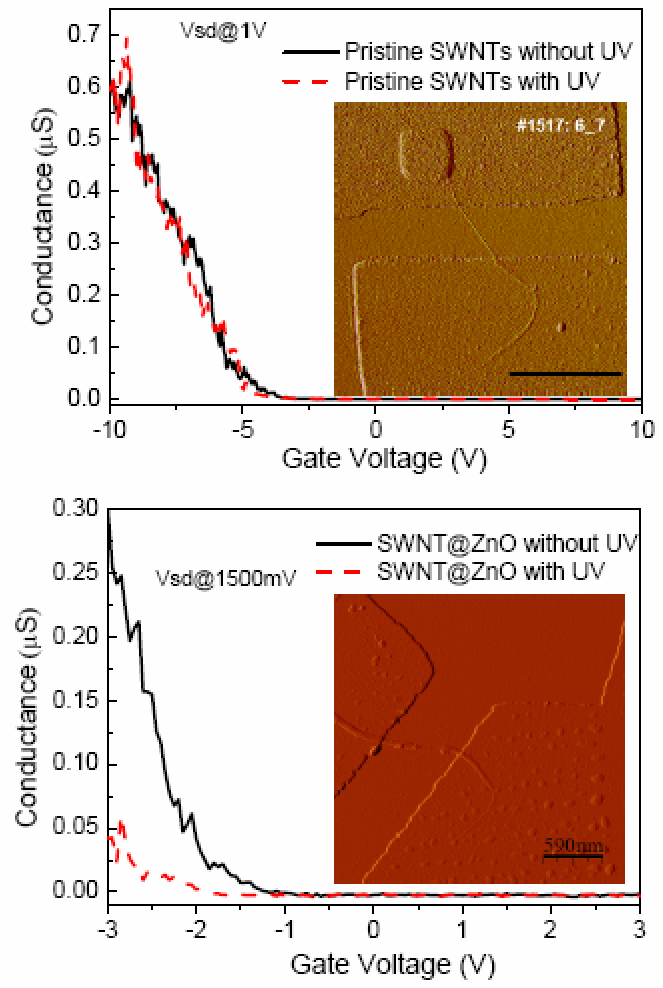

Figure 7.5 (a) Conductance vs gate voltage (Vg) of pristine SWNT recorded under a bias voltage of 1 V (scalar bar is 1 μm) and (b) SWNT@ZnO under a Vsd at 1500 mV in air and via UV exposure.

7.4 Ultraviolet photoresponse of single ZnO nanorod

ZnO nanorods were fabricated by soft chemical process and vapor-liquid-solid method from our lab and *ITRI* in Taiwan, respectively. The typical length of the resulting nanowires was 1 μm, with typical diameters in the range of 30–50 nm. Selected-area diffraction patterns showed the nanorods to be single crystal. They were released from the substrate and then transferred to SiO_2 coated metallic Si substrates. E-beam lithography was used to pattern sputtered Pd-Au electrodes contacting both ends of a single nanorod. The separation of the electrodes was 500 nm. Atomic force microscopy (AFM) of the completed device is shown in **Figure 7.6.** Au wires were bonded to the contact pad for current voltage (I–V) measurements performed at 25 ^{o}C in air. In some cases, the nanorods were illuminated with above band gap light mixed with 254 or 366 nm from Hg lamp. **Figure 7.7** shows the I–V characteristics of the nanorod in the dark. The conductivity is nearly non-changed as applying voltage, even at high bias. It suggests that terrible ohmic contacts were formed between the nanorod and electrodes. However, in photoresponse measurement, the conductivity is greatly increased during the illumination.

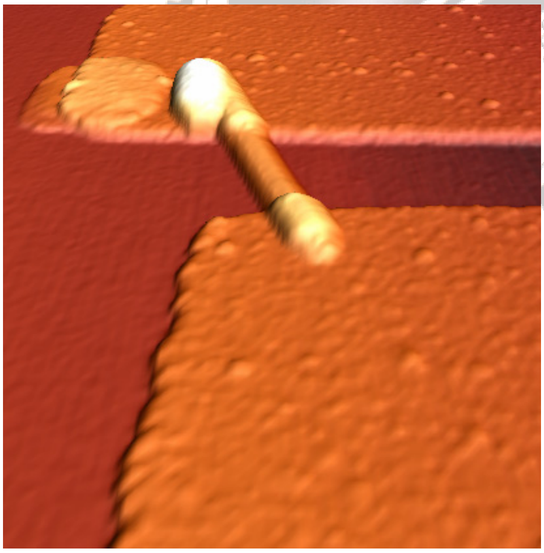

Figure 7.6 AFM image of ZnO nanorod device

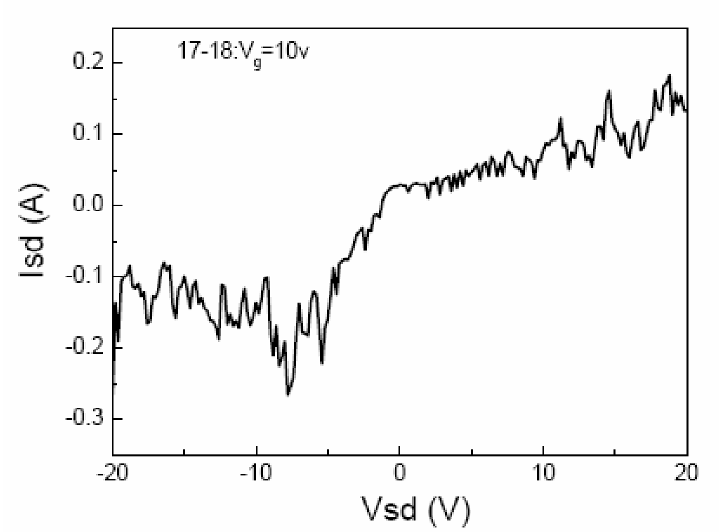

Figure 7.7 *I–V* characteristics of the ZnO nanorod in the dark.

Figure 7.8 shows the photoresponse of the single ZnO nanorod at zero bias under pulsed illumination from UV regional wavelength Hg lamp. The photoresponse is much faster than that reported for ZnO nanowires grown by thermal evaporation and likely is due to the reduced influence of the surface states seen in that material. In the photoconduction in ZnO nanorods, holes produced by both the above-gap and below-gap light discharge the negatively charged oxygen ions on the surface of the nanorods, the photoexcited electrons are trapped at some centers, and the electrons escaped from the centers transit to electrodes. The time constant under consideration corresponds to the trapping time of the electrons. The recombination times in high-quality ZnO measured from time-resolved photoluminescence are short (pico-sec), while the photoresponse measures the electron-trapping time. There is also a direct correlation reported between the photoluminescence lifetime and the defect density in both bulk and epitaxial ZnO. In our nanorods, the electron-trapping times are on the order of tens of seconds and these trapping effects are only a small fraction of the total photoresponse recovery characteristic.

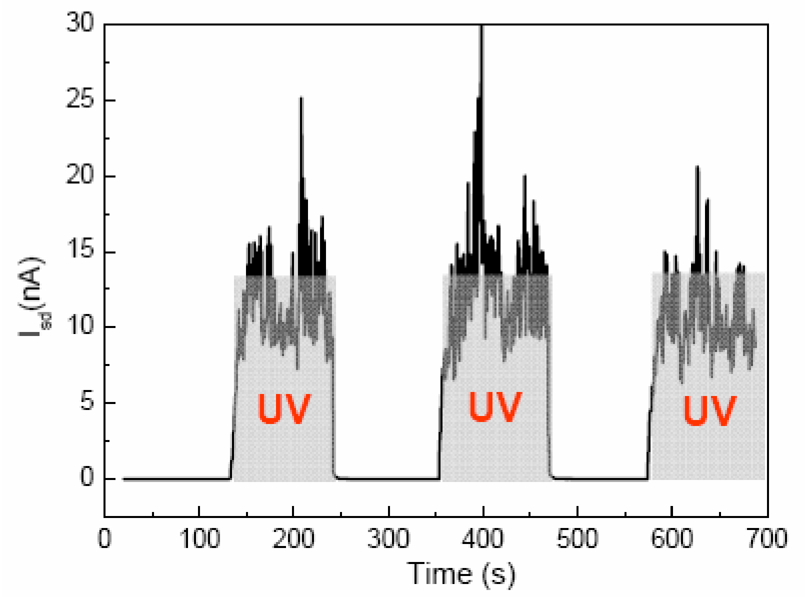

Figure 7.8 Photoresponse of the single ZnO nanorod at zero bias and Vsd=5V.

7.5 Summary

We have demonstrated a flexible method to coat SWNTs in solution. The results of Raman analysis presents the surface state in carbon nanotubes would be changed by react with TEO-Zn molecule. On transport measurements point to the electrons in SWNTs could be compensated by holes carrier attributed to ZnO layer with UV excitation. Furthermore, this continuous coating of one dimensional material supplies a future for multifunctional nanodevices. In addition to ZnO-SWNTs composite, the electrical transport property of individual ZnO nanorod presents the excellent photoresponse behavior. It has great potential for application in optical switch device.

Chapter 8

Conclusions

For this thesis, we studied the physical and electrical properties of ZnO material from thin films to one-dimensional nanostructure. Firstly, we have demonstrated the ZnO thin films have strongly preferred-orientation and with a sharp UV emission peak around 3.28 eV. Moreover, we have also shown that it is possible to control the UV and deep-level emissions in the sputtered ZnO films by changing annealing temperatures and using different gas atmospheres. In order to fabricate low defect concentration thin films, we used various buffer-layers to produce high quality ZnO films. As the previous study, we have also observed the a strong ultraviolet (UV) emission peak around 3.28 eV along with a weak deep-level emission from ZnO films on Si substrate annealed at 850°˚C in O_2 and N_2 atmospheres. In contrast, the ZnO films deposited on SiO_2/Si substrate show two double peaks in the room-temperature PL spectra, one double (374 nm and 394 nm) near to the UV peak and the other one (495 nm and 605 nm) located in the visible region. The peak at 394 nm (3.15 eV) in the ultraviolet region was assigned to the defect transition form oxygen vacancies ($V_o^{\bullet}$) level to valence band due to the variation of the type and concentration of intrinsic defects in the local microstructure of ZnO/SiO_2/Si. If the ZnO film was grown on Si_3N_4/Si, a very strong UV along with invisible deep-level emission was detected because the Si_3N_4 can effectively improve film stoichiometry and reduce the defect formation of oxygen vacancies and Zn interstitials compared to ZnO on SiO_2/Si and Si. (Chapter 3)

For formation *p*-type ZnO thin films, we used two elements to dope into ZnO films with ion implantation technology. In the phosphorus implantation, it has been demonstrated that below solubility (1.5×10^{18} ions/cm^3), the defect formation will be dominated by annealing atmosphere and more defects can be formed in oxygen ambient than in nitrogen atmosphere as revealed from PL spectra. However, excess phosphorus doping, above solubility (1.5×10^{18} ions/cm^3), will induce the formation of the phosphide compounds in ZnO films and seriously deteriorate the crystallinity and optical property of the films. However, a high resistive but not p-type ZnO film is obtained by phosphorus doping. But in another case, we have successfully fabricated p-type ZnO films deposited on a Si_3N_4/Si substrate and with nitrogen-implantation. The Si_3N_4 buffer layer can effectively improve film stoichiometry and reduce the formation of oxygen vacancies compared to ZnO on Si. The electrical properties of the *p*-type ZnO films implanted with 5×10^{12}-1×10^{14} cm^{-2} N^+ dose show a hole concentration of $5.0\times10^{16}-7.3\times10^{17}$ cm^{-3}, hole mobility of 2.51-6.02 cm^2/Vs, and resistivity of 10.11-15.3 Ωcm. The *p*-type ZnO films also showed an excellent crystallinity and a strong ultraviolet emission peak near 3.30 eV at room temperature. Moreover, as evidenced by extended x-ray absorption fine structure analysis, the local structure of the *p*-type ZnO films was changed due to the substitution of nitrogen ions for oxygen ions in *p*-type ZnO films. Our finding of *p*-type ZnO films grown on a Si_3N_4/Si substrate could provide a simple method to fabricate reproducible *p*-type ZnO films on silicon substrate for the development of large-scale optoelectronic integration device. (Chapter 4)

Based on high quality ZnO thin films, we continued to investigate physical and chemical characteristics of one-dimensional ZnO nanostructure. We have developed a low-temperature synthetic route to prepare well-aligned arrays of oriented ZnO nanorods in the diameter of ~60 nm on the organic substrates without any extra buffered layer in aqueous solution. It was found that the ZnO nanorods are preferentially nucleated from the ZnO monolayer under the concave regions of polystyrene (PS) layers and grown along <0001> direction in the initial growth stage. HRTEM analysis demonstrates that well-aligned ZnO nanorods are preferentially nucleated from the ZnO monolayer under the concave regions of PS layers. However, a long-term growth process leads to the formation of a larger ZnO crystal due to coplanar coalescence behavior of several individual ZnO nanorods. The room temperature photoluminescence measurement demonstrates that a stronger ultraviolet (UV) emission with a broad yellow emission around 575 nm was observed for the ZnO nanorods grown on organic substrates. This simple approach was demonstrated to shows great potential for optoelectronic devices because it can produce large-scale highly well-aligned ZnO nanorods on flexible organic substrates at lower temperatures. In the investigation of thermal annealing effects on ZnO nanorods, we concluded that optical properties of ZnO nanorods can be much improved by annealing at high temperatures in both atmospheres of N_2 and O_2. This improvement ascribed to the decrease in structure defects as compared to as-grown ZnO nanorods. However, for the ZnO nanorods annealed in H_2/N_2, a stronger UV emission occurs at 600^oC, above that the UV emission was rapidly disappeared that was attributed to the collapse of the ZnO nanorods due to H_2 etching during a higher-temperature annealing in H_2/N_2. The crystallinity and optical properties of the ZnO nanorods can be controlled by post-annealing treatment. (Chapter 5)

In order to improve the photoluminescence and electrical transport properties, we used plasma treatment to modify the surface state on ZnO nanorods. Photoelectronic characteristics are performed in well-aligned hydrogen-plasma ZnO nanorods grown on four-inch flexible organic substrates buffered with ZnO films. Enhancement of PL properties due to H_2 plasma treatment by a factor of 60 times for relative intensity ratio (ultraviolet emission (I_{UV}) to deep level emission (I_{DLE})) has been observed.

X-ray photoelectron spectroscopy (XPS) analysis reveals that the enhanced PL property is attributed to both defect passivation and modification on the surface region of ZnO nanorods due to the absorption of hydrogen ions. However, the photoluminescence spectra of H_2 -plasma ZnO nanorods can be restored to original state of ZnO nanorods by thermal annealing process. The *I-V* measurements suggest that the n-type ZnO nanorods with H_2 plasma treatment present a higher conductivity about 5-6 orders of magnitude than the non-plasma ZnO nanorods. In ammonia plasma treatment, x-ray photoelectron spectroscopy measurement demonstrates that the nitrogen-doped ZnO nanorods have been formed due to nitrogen diffusion through surface adsorption or defect routes. The photoluminescence spectra indicate that a strong UV emission peak around 3.31 eV with negligible deep level emission can be obtained for the nitrogen-doped ZnO nanorods compared to that of the untreated sample. The electrical transport measurements indicate that the p-type ZnO nanorods with a smaller threshold voltage of 1.5 V can be obtained. (Chapter 6)

The results of Raman analysis reveals the surface state in carbon nanotubes would be changed by react with TEO-Zn molecule. Moreover, we also used HRTEM with EDS to demonstrate ZnO could really be coated on SWNTs. On transport measurements point to the electrons in SWNTs could be compensated by holes carrier attributed to ZnO layer with UV excitation. Furthermore, this continuous coating of one dimensional material supplies a future for multifunctional nanodevices. In addition to ZnO-SWNTs composite, the electrical transport property of individual ZnO nanorod presents the excellent photoresponse behavior. It has great potential for application in optical switch device. (Cahpter 7)

References

[1] D. M. Bagnall, Y. R. Chen, Z. Zhu, T. Yao, S. Koyama, M. Y. Shen, T. Goto, *Appl. Phys. Lett.* **70** (1997) 2230.

[2] M. Wraback, H. Shen, S. Liang, C.R. Gorla, Y. Lu, *Appl. Phys. Lett.* **74** (1999) 507.

[3] J.-M. Lee, K.-K. Kim, S.-J. Park, W.-K. Choi, *Appl. Phys. Lett.* **78** (2001) 2842.

[4] D. C. Look, D. C. Reynolds, J. W. Hemsky, R. L. Jones, J. R. Sizelove, *Appl. Phys. Lett.* **75** (1999) 811.

[5] D. C. Look, J. W. Hemsky, J. R. Sizelove, *Phys. Rev. Lett.* **82** (1999) 2552.

[6] F. D. Auret, S. A. Goodman, M. Hayes, M. J. Legodi, H. A. van Laarhoven, D. C. Look, *Appl. Phys. Lett.* **80** (2002) 956.

[7] S. O. Kucheyev, J. E. Bradley, J. S. Williams, C. Jagerdish, M. V. Swain, *Appl. Phys. Lett.* **80** (2002) 956.

[8] M. Wraback, H. Shen, S. Liang, C. R. Gorla, Y. Lu, *Appl. Phys. Lett.* **76** (1999) 507.

[9] T. Aoki, D. C. Look, Y. Hatanaka, *Appl. Phys. Lett.* **76** (2000) 3257.

[10] P. M. Verghese, D. R. Clarke, *J. Appl. Phys.* **87** (2000) 4430.

[11] C. R. Gorla, N. W. Emanetoglu, S. Liang, W. E. Mayo, Y. Lu, M. Wraback, H. Shen, *J. Appl. Phys.* **85** (1999) 2595.

[12] H. Ohta, K. Kawamura, M. Orita, M. Hirano, N. Sarukura, H. Hosono, *Appl. Phys. Lett.* **77** (2000) 475.

[13] M. Joseph, H. Tabata, T. Kawai, *Japan. J. Appl. Phys.* **38** (1999) L1205.

[14] Y. Li, G. S. Tompa, S. Liang, C. Gorla, C. Lu, J. Doyle, *J. Vac. Sci. Technol. A* **15** (1997) 1663.

[15] C. C. Lin, S. Y. Chen, S. Y. Cheng, and H. Y. Lee, *Appl. Phys. Lett.* **84** (2004) 5040.

[16] J. Wollenstein, J. A. Plaza, C. Cane, Y. Min, H. Botttner, H. L. Tuller. *Sensors Actuat. B* **93** (2003) 350.

[17] M. W. Barsoum, Fundamentals of Ceramics (McGraw-Hill, New York, 1997).

[18] R. A. Powell, W. E. Spicer, and J. C. McMenamin, *Phys. Rev. Lett.* **27** (1971) 97.

[19] L. Ley, R. A. Pollak, F. R. McFeely, S. P. Kowalezyk, and D. A. Shirley, *Phys. Rev. B* **9** (1974) 600.

[20] D. W. Langer and C. J. Vesely, *Phys. Rev. B* **2** (1970) 4885.

[21] I. Ivanov and J. Pollmann, *Phys. Rev. B* **24** (1981) 7275.

[22] D. H. Lee and J. D. Joannopoulos, *Phys. Rev. B* **24** (1981) 6899.

[23] R. T. Girard, O. Tjernberg, G. Chiaia, S. Söderholm, U. O. Karlsson, C. Wigren, H. Nylèn, and I. Lindau, *Surf. Sci.* **373** (1997) 409.

[24] P. Schröer, P. Krüger, and J. Pollmann, *Phys. Rev. B* **47** (1993) 6971.

[25] C. B. Duke, R. J. Meyer, A. Paton, and P. Mark, *Phys. Rev. B* **18** (1978) 4225.

[26] P. Schröer, P. Krüger, and J. Pollmann, *Phys. Rev. B* **49** (1994) 17092.

[27] J. L. Martins, N. Troullier, and S. H. Wei, *Phys. Rev. B* **43** (1991) 2213.

[28] Y.-N. Xu and W. Y. Ching, *Phys. Rev. B* **48** (1993) 4335.

[29] O. Zakharov, A. Rubio, X. Blasé, M. L. Cohen, and S. G. Louie, *Phys. Rev. B* **50** (1994) 10780.

[30] D. Vogel, P. Krüger, and J. Pollmann, *Phys. Rev. B* **52** (1995) R14316.

[31] N. A. Hill and U. Waghmare, *Phys. Rev. B* **62** (2000) 8802.

[32] J. E. Jaffe, R. Pandey, and A. B. Kunz, *Phys. Rev. B* **43** (1991) 14030.

[33] J. E. Jaffe, J. A. Snyder, Z. Lin, and A. C. Hess, *Phys. Rev. B* **62** (2000) 1660.

[34] J. D. Albrecht, P. P. Ruden, S. Limpijumnong, W. R. L. Lambrecht, and K. F. Brennan, *J. Appl. Phys.* **86** (1991) 6864.

[35] D. C. Look, J. W. Hemsky, and J. R. Sizelove, *Phys. Rev. Lett.* **82** (1999) 2552.

[36] M. E. Lin, Z. Ma, F. Y. Huang, Z. F. Fan, L. H. Allen, and H. Morkoç, *Appl. Phys. Lett.* **64** (1994) 1003.

[37] A. A. Iliadis, R. D. Vispute, T. Venkatesan, and K. A. Jones, *Thin Solid Films* **420–421** (2002) 478.

[38] H. Ishikawa, K. Tsukui, Y. Koide, N. Teraguchi, Y. Tomomura, A. Suzuki and M. Murakami, *J. Vac. Sci. Technol. B* **14** (1996) 1812.

[39] H. K. Kim, J. W. Bae, T. K. Kim, K. K. Kim, T. Y. Seong, I. Adesida, *J. Vac. Sci. Technol. B* **21** (2003) 1273.

[40] H.-K. Kim, S.-H. Han, T.-Y. Seong, W.-K. Choi, *Appl. Phys. Lett.* **77** (2000) 1647.

[41] H.-K. Kim, S.-H. Han, T.-Y. Seong, W.-K. Choi, *J. Electrochem. Soc.* **148** (2001) G114.

[42] Y. Chen, D. Bagnell, T. Yao, *Mater. Sci. Eng. B* **75** (2000) 190.

[43] T. Akane, K. Sugioka, K. Midorikawa, *J. Vac. Sci. Technol. B* **18** (2001) 1406.

[44] H. Sheng, N.W. Emanetoglu, S. Muthukumar, S. Feng, Y. Lu, *J. Electron. Mater.* **31** (2002) 811.

[45] F. D. Auret, S. A. Goodman, M. Hayes, M. J. Legodi, H. A. van Laarhoven, and D. C. Look, *Appl. Phys. Lett.* **79** (2001) 3074.

[46] A. Y. Polyakov, N. B. Smirnov, E. A. Kozhukhova, V. I. Vdodin, K. Ip, Y. W. Heo, D. P. Norton, and S. J. Pearton, *Appl. Phys. Lett.* **83** (2003) 1575.

[47] B. J. Koppa, R. F. Davis, and R. J. Nemanich, *Appl. Phys. Lett.* **82** (2003) 400.

[48] R. C. Neville, C. A. Mead, *J. Appl. Phys.* **41** (1970) 3795.

[49] M. Fox, Optical Properties of Solids (Oxford, London, 2001)

[50] A. Mang, K. Reimann, and St. Rübenacke, *Solid State Commun.* **94** (1995) 251.

[51] K. Thonke, T. Gruber, N. Teofilov, R. Schönfelder, A. Waag, and R. Sauer,

Physica B **308–310** (2001) 945.

[52] K. -K. Kim, H. -S. Kim, D. -K. Hwang, J. -H. Lim, and S. -J. Park, *Appl. Phys. Lett.* **83** (2003) 63.

[53] D. C. Reynolds, D. C. Look, B. Jogai, C. W. Litton, G. Cantwell, and W. C. Harsch, *Phys. Rev. B* **60** (1999) 2340.

[54] A. F. Kohan, G. Ceder, D. Morgan, and C. G. Van de Walle, *Phys. Rev. B* **61** (2000) 15019.

[55] C. G. Van de Walle, *Physica B* **308–310** (2001) 899.

[56] C. Morhain *et al.*, *Phys. Stat. Sol. (b)* **229** (2002) 881.

[57] H. Kato, M. Sano, K. Miyamoto, and T. Yao, *J. Cryst. Growth* **237–239** (2002) 538.

[58] S. Y. Myong, S. J. Baik, C. H. Lee, W. Y. Cho, and K. S. Lim, *Jpn. J. Appl. Phys.* Part 2 **36** (1997) L1078.

[59] H. J. Ko, Y. F. Chen, S. K. Hong, H. Wenisch, T. Yao, and D. C. Look, *Appl. Phys. Lett.* **77** (2000) 3761.

[60] Z. F. Liu, F. K. Shan, Y. X. Li, B. C. Shin, and Y. S. Yu, *J. Cryst. Growth* **259** (2003) 130.

[61] W. Walukiewicz, *Phys. Rev. B* **50** (1994) 5221.

[62] C. G. Van de Walle, D. B. Laks, G. F. Neumark, and S. T. Pantelides, *Phys. Rev. B* **47** (1993) 9425.

[63] D. B. Laks, C. G. Van de Walle, G. F. Neumark, S. T. Pantelides, *Appl. Phys. Lett.* **63** (1993) 1375.

[64] A. Valentini, F. Quaranta, M. Rossi, G. Battaglin. *J. Vac. Sci. Technol. A* **9** (1991) 286.

[65] T. Nagata, T. Shimura, Y. Nakano, A. Ashida, N. Fujimura, T. Ito, *Jpn. J. Appl. Phys.* Part 1 **40** (2001) 5615.

[66] C. H. Park, S. B. Zhang, S.–H. Wei, *Phys. Rev. B* **66** (2002) 0732021.

[67] G. F. Neumark, *Phys. Rev. Lett.* **62** (1989) 1800.

[68] D. B. Laks, C. G. Van de Walle, G. F. Neumark, and S. T. Pantelides, *Phys. Rev. Lett.* **66** (1991) 648.

[69] A. Garcia and J. E. Northrup, *Phys. Rev. Lett.* **74** (1995) 1131.

[70] D. C. Look, B. Claflin, Ya. I. Alivov, and S. J. Park, *Phys. Stat. Sol. (a)* **201** (2004) 2203.

[71] L. Vayssieres, *Int. J. Nanotechnol.* **1(1–2)** (2004) 1.

[72] Z. L. Wang, *Mater. Today* **7** (2004) 26.

[73] W. I. Park, D. H. Kim, S.-W. Jung, and G.-C. Yi, *Appl. Phys. Lett.* **80** (2002) 4232.

[74] R. S. Wagner and W. C. Ellis, *Appl. Phys. Lett.* **4** (1964) 89.

[75] Z. W. Pan, Z. R. Dai and Z. L. Wang, *Science* **291** (2001) 1947.

[76] P. X. Gao, and Z. L. Wang, *J. Am. Chem. Soc.* **125 (37)** (2003) 11299.

[77] C. C. Lin, K. H. Liu, S. Y. Chen, S. Y. Cheng, *J. Crystal Growth* **269** (2004) 245.

[78] L. Vayssieres, C. Chaneac, E. Tronc, and J. P. Jolivet, *J. Colloid Interface Sci.* **205(2)** (1998) 205.

[79] S. Cho, J. Ma, Y. Kim, Y. Sun, G. K. L. Wang, and J. B. Ketterson, *Appl. Phys. Lett.* **75** (1999) 2761.

[80] E. G. Bylander, *J. Appl. Phys.* **49** (1978) 1188.

[81] D. Hahn and R. Nink, *Phys. Condens. Mater.* **3** (1965) 311.

[82] M. Liu, A. H. Kitai, and P. Mascher, *J. Lumin.* **54** (1992) 35.

[83] Y. Zhang, G. Du, D. Liu, X. Wang, Y. Ma, J. Wang, J. Yin, X. Yang, X. Hou, and S. Yang, *J. Cryst. Growth,* **243** (2002) 439.

[84] B. J. Jin, S. Im, and S. Y. Lee, *Thin Solid Films* **366** (2000) 107.

[85] P. H. Kasai, *Phys. Rev.* **130** (1963) 989.

[86] F. A. Kroger and H. J. Vink, *J. Chem. Phys.* **22** (1954) 250.

[87] E. A. Secco and W. J. Moore, *J. Chem. Phys.* **26** (1957) 942.

[88] G. D. Mahan, *J. Appl. Phys.* **54** (1983) 3825.

[89] S. A. M. Lima, F. A. Sigoli, M. Jafelicci, and M. R. Davolos, *Int. J. Inorg. Mater.* **3** (2001) 749.

[90] N. Fujimura, T. Nishihara, S. Goto, J. Xu, and T. Ito, *J. Cryst. Growth,* **130** (1993) 169.

[91] J. Hinze and K. Ellmer, *J. Appl. Phys.,* **88** (2000) 2443.

[92] Y. Chen, D. M. Bagnall, Z. Zhu, T. Sekiuchi, K.-T. Park, K. Hiraga, T. Yao, S. Koyama, M. Y. Shen, and T. Goto, *J. Cryst. Growth,* **181** (1997) 165.

[93] N. Riehl, *J. Lumin.* **24-25** (1981) 335.

[94] N. Y. Garces, N. C. Giles, L. E. Halliburton, G. Cantwell, D. B. Eason, D. C. Reynolds, and D. C. Look, *Appl. Phys. Lett.* **80** (2002) 1334.

[95] X. L. Wu, G. G. Siu, C. L. Fu, and H. C. Ong, *Appl. Phys. Lett.* **78** (2001) 2285.

[96] C. R. Gorla, N. W. Emanetoglu, S. Liang, W. E. Mayo, Y. Lu, M. Wraback, and H. Shen, *J. Appl. Phys.* **85** (1999) 2595.

[97] E. Fogarassy, A. Siaoul, C. Fuchs, and J. L. Regolini, *Appl. Phys. Lett.* **51** (1987) 337.

[98] E. P. O'Reilly and J. Robertson, *Phys. Rev. B* **27** (1983) 3780.

[99] S. H. Jeong, B. S. Kim, and B. T. Lee, *Appl. Phys. Lett.* **82** (2003) 2625.

[100] W. Göpel, *J. Vac. Sci. Technol.* **16** (1979) 1229.

[101] Q. X. Zhao, M. Willander, W. Lu, X. Q. Liu, S. C. Shen, H. H. Tan, C. Jagadish, J. Zou, and D. J. H. Cockayne, *J. Appl. Phys.* **88** (2000) 2519.

[102] T. Yamamoto and H. Yoshida, *Jpn. J. Appl. Phys.* Part 2 **38** (1999) L166.

[103] M. Kasuga and S. Ogawa, *Jpn. J. Appl. Phys.* Part 1 **22** (1983) 794.

[104] Y. Sato and S. Sato, *Thin Solid Films* **281** (1996) 445.

[105] X.-L. Guo, H. Tabata, and T. Kawai, *J. Cryst. Growth* **223** (2001) 135.

[106] S. M. Myers, *J. Vac. Sci. Technol.* **15** (1978) 1650.

[107] C. C. Lin, S. Y. Chen, and S. Y. Cheng, *Electrochem. Solid-State Lett.* **7** (2004) J20.

[108] S. H. Bae, S. Y. Lee, B. J. Jin, and S. Im, *Appl. Surf. Sci.* **154** (2000) 458.

[109] M. H. Huang, Y. Wu, H. Feick, N. Tran, E. Weber, P. Yang, *Adv. Mater.* **13** (2001) 113.

[110] W.T. Chiou, W.Y. Wu, J.M. Ting, *Diam. Relat. Mater.* **12(10-11)** (2003) 1841.

[111] N. Audebrand, J. P. Auffredic, D. Louer, *Chem. Mater.* **10** (1998) 2450.

[112] C.-H. Lu, C.-H. Yeh, *Ceram. Int.* **26** (2000) 351.

[113] L. Vayssieres, *Adv. Mater.* **15** (2003) 464.

[114] L. Vayssieres, K. Keis, S.-E. Lindquist, A. Hagfeldt, *J. Phys. Chem. B* **105** (2001) 3350.

[115] Z. R. Tina, J. A. Voigt, J. Liu, B. Mckenzie, M. J. Mcdermott, M. A. Rodriguez, H. Konishi, H. Xu, *Nature Mater.* **2** (2003) 821.

[116] S. C. Liou, C. S. Hsiao, S. Y. Chen, *J. Crystal Growth* **274** (2004) 438.

[117] C. Pacholski, A. Kornowski, H. Weller, *Angew. Chem. Int. Ed.* **41** (2002) 1188.

[118] A. N. Gruzintsev and E. E. Yakimov, *Inorg. Mater.* **41** (2005) 725.

[119] L. E. Greene, M. Law, J. Goldberger, F. Kim, J. C. Johnson, Y. Zhang, R. J. Saykall, and P. Yang, *Angew. Chem., Int. Ed.* **42** (2003) 3031.

[120] C. C. Lin, C. S. Hsiao, S. Y. Chen, and S. Y. Cheng, *J. Electrochem. Soc.* **151** (2004) G285.

[121] Y. Q. Chang, D. B. Wang, X. H. Luo, X. Y. Xu, X. H. Chen, L. Li, C. P. Chen, R. M. Wang, J. Xu, D. P. Yu, *Appl. Phys. Lett.* **83** (2003) 4020.

[122] J. J. Wu, S. C. Liu, M. H. Yang, *Appl. Phys. Lett.* **85** (2004) 1027.

[123] C. C. Lin, H. P. Chen, and S. Y. Chen, *Chem. Phys. Lett.* **404** (2005) 30.

[124] N. Ohashi, T. Ishigaki, N. Okada, T. Sekiguchi, I. Sakaguchi, and H. Haneda, *Appl. Phys. Lett.* **80** (2002) 2869.

[125] K. Ozawa and K. Edamoto, *Surf. Sci.* **524** (2003) 78.

[126] J. C. C. Fan, and J. B. Goodenough, *J. Appl. Phys.* **48** (1977) 3524.

[127] D. Li, Y. H. Leung, A. B. Djurisic, Z. T. Liu, M. H. Xie, S. L. Shi, S. J. Xu, W. K. Chen, *Appl. Phys. Lett.* **85** (2004) 1601.

[128] L. Spanhel, M. Hnase, H. Weller, A. Henglein, *J. Am. Chem. Soc.* **109** (1987) 5649.

[129] V. L. Colvin, M. C. Schlamp, A. P. Alivisatos, *Nature* **370** (1994) 354.

[130] P. V. Kamat, B. Shanghavi, *J. Phy. Chem.* **101** (1997) 7675.

[131] A. P. Alivisatos, *Science* **271** (1996) 933.

[132] C. Petit, M. P. Pileni, *J. Phy. Chem.* **92** (1988) 2282.

[133] X. Peng, M. C. Schlamp, A. V. Kadavanich, A. P. Alivisatos, *J. Am. Chem. Soc.* **119** (1997) 7019.

[134] A. R. Kortan, R. Hull, R. L. Opila, M. G. Bawendi, M. L. Steigerwald, P. J. Carroll, L. E. Brus, *J. Am. Chem. Soc.* **112** (1990) 1327.

[135] H. L. Xia, F. Q. Tang, *J. Phy. Chem. B* **107** (2003) 9175.

[136] Z. Tang, N. A. Kotov, *Adv. Mater.* **17** (2005) 951.

[137] E. C. Walter, B. J. Murray, F. Favier, R. M. Penner, *Adv. Mater.* **15** (2003) 396.

[138] F. Balavoine, P. Schultz, C. Richard, V. Mallouh, T. W. Ebbesen, C. Mioskowski, *Angew. Chem., Int. Ed.* **38** (1999) 1912.

[139] T. Seeger, T. Köhler, T. Frauenheim, N. Grobert, M. Rühle, M. Terrones, G. Seifert, *Chem. Commun.* (2002) 34.

[140] S. Fullam, D. Cottel, H. Rensmo, D. Fitzmaurice, *Adv. Mater.* **12** (2000) 1430.

[141] Y. P. Sun, W. Huang, Y. Lin, K. Fu, A. Kitaygorodskiy, L. A. Riddle, Y. J. Yu, D.

L. Carroll, *Chem. Mater.* **13** (2001) 2846.

[142] W. Q. Han, A. Zettl, *Nano Lett.* **3** (2003) 681.

[143] X. Li, J. Niu, J. Zhang, H. Li, Z. Liu, *J. Phy. Chem. B* **107** (2003) 2453.

[144] Q. Fu, C. Lu, J. Liu, *Nano Lett.* **2** (2002) 329.

[145] L. Fu, Y. Liu, Z. Liu, B. Han, L. Cao, D. Wei, G. Yu, D. Zhu, *Adv. Mater.* **18** (2006) 181.

[146] K. C. Chin, A. Gohel, W. Z. Chen, H. I. Elim, W. Ji, G. L. Chong, C. H. Show, A. T. S. Wee, *Chem. Phys. Lett.* **409** (2005) 85.

[147] J. S. Ye, H. F. Cui, X. Liu, T. M. Lim, W. D. Zhang, F. S. Sheu, *Small* **1** (2005) 560.

[148] C. Pacholski, A. Kronowski, H. Weller, *Angew. Chem. Int. Ed.* **41** (2002) 1188.

[149] N. Arul Dhas, A. Zaban, A. Gedanken, *Chem. Mater.* **11** (1999) 806.

[150] Y. Zhu, H. I. Elim, Y. L. Foo, T. Yu, Y. Liu, W. Ji, J. Y. Lee, Z. Shen, A. T. S. Wee, J. T. L. Thong, C. H. Sow, *Adv. Mater.* **18** (2006) 587.

[151] S. Ravindran, C. S. Ozkan, *Nanotechnology* **16** (2005) 1130.

[152] R. J. Chen, N. R. Franklin, J. Kong, J. Cao, T. W. Tombler, Y. Zhang, H. Dai, *Appl. Phys. Lett.* **79** (2001) 2258.

[153] M. Shim, G. P. Siddons, *Appl. Phys. Lett.* **83** (2003) 3564.

[154] Y. Yan and M. M. Al-Jassim, *Phys. Rev. B* **69** (2004) 085204.

[155] E.-C. Lee, Y.-S. Kim, Y.-G. Jin, and K. J. Chang, *Phys. Rev. B* **64** (2001) 085102.

Curriculum Vitae

Name: Chin-Ching Lin

15.12.1976 Born in Taichung (Taiwan)

1995-1999 Undergraduate study in the department of electronic engineering at Feng Chia University

1999-2001 Graduate study in the institute of precision engineering at Chung Hsing University

Master Thesis: A Research on $(Ba,Sr)TiO_3$ Thin Films for Dynamic Random Access Memory Applications

2001-2006 PhD study in the department of materials science and engineering at Chiao Tung University (Taiwan)

PhD Thesis: Optoelectronic Characteristics and Structure Development of One- and Two-Dimensional Zinc Oxide Materials

2005-2006 Scholarship study in Max-Planck Institute for Solid State Research, Stuttgart (Germany). Scholarship sponsored by Deutscher Akademischer Austauschdienst (DAAD) in Germany and “NSC” in Taiwan.

Publication list

Journal

1. C. C. Lin, C. S. Hsiao, S. Y. Chen, and S. Y. Cheng, "Ultraviolet Emission in ZnO Films Controlled by Point Defects", *J. Electrochem. Soc.*, **151(5)** (2004) G285.

2. C. C. Lin, S. Y. Chen, and S. Y. Cheng,, "PL Dependence of ZnO Films Grown on Si with Various Buffer Layers by RF Magnetron Sputtering", *Electrochem. Solid-State Lett.,***7** (2004) J20.

3. C. C. Lin, S. Y. Chen, S. Y. Cheng, and H. Y. Lee, "Properties of nitrogen-implanted *p*-type ZnO films grown on Si_3N_4/Si by radio-frequency magnetron sputtering", *Appl. Phys. Lett.*, **84** (2004) 5040.

4. C. C. Lin, S. Y. Chen, and S. Y. Cheng, "Physical characteristics and photoluminescence properties of Phosphrous-implanted ZnO thin films", *Appl. Surf. Sci.*, **238** (2004) 405.

5. C. C. Lin, K. H. Liu, and S. Y. Chen, "Growth and characterization of ZnO-Zn core-shell polygon prismatic nanocrystals on Si", *J. Crystals Growth*, **269** (2004) 425.

6. C. C. Lin, H. P. Chen, and S. Y. Chen, "Well-aligned and patterned arrays of ZnO nanorods on organic substrates in aqueous solutions", *J. Crystals Growth*, **283** (2005) 141.

7. C. C. Lin, H. C. Liao, S. Y. Chen, and S. Y. Cheng, "Luminescent and structural properties of ZnO nanorods by post annealing", *J. Vac. Sci. Technol., B* **24** (2006) 304.

8. C. C. Lin, H. P. Chen, and S. Y. Chen, "Synthesis and optoelectronic properties of arrayed *p*-type ZnO nanorods grown on Si wafer in aqueous solutions", *Chem. Phys. Lett.*, **404** (2005) 30.

9. **C. C. Lin**, H. P. Chen, H. C. Liao, and S. Y. Chen, “Enhanced luminescent and electrical properties of hydrogen-plasma ZnO nanorods grown on wafer-scale flexible substrates”, *Appl. Phys. Lett.,* **86** (2005) 183103.

10. K. H. Liu, **C. C. Lin**, and S. Y. Chen, “Formation of Zn-ZnO polygon prismatic nanocrystals by liquid source via thermal vapor transport”, *J. Mater. Sci. Forum*, **480** (2005) 309.

11. K. H. Liu, **C. C. Lin**, and S. Y. Chen, “Growth and physical characterization of polygon prismatic hollow Zn-ZnO crystals”, *Crystals Growth & Design,* **5** (2005) 483.

12. C. C. Yang, **C. C. Lin**, and S. Y. Chen, “Physical characteristics and photoluminescenceproperties of nitrogen-Implanted ZnO Thin Film”, *J. Crystals Growth,* **285** (2005) 96.

13. T. Y. Liu, H. C. Liao, **C. C. Lin**, S. H. Hu, and S. Y. Chen, “Biofunctional ZnO Nanorod Arrays Grown on Flexible Substrates”, *Langmuir, in press.*, (2006)

14. R. H. Horng, D. S. Wuu, C. Y. Kung, **C. C. Lin**, C. C. Leu, T. Y. Haung, and S. M. Sze, “Ion-implantation Treatment (Ba,Sr) TiO_3 Thin Films, *Jpn. J. Appl. Phys.*, **39** (2000) 6614.

15. D. S. Wuu, **C. C. Lin**, R. H. Horng, F. C. Liao, and Y. H. Liu, “Etching characteristics and plasma-induced damage of high-*k* Ba0.5Sr0.5TiO3 thin-film capacitors”, *J. Vac. Sci. Technol. B*, **19** (2001) 2231.

16. D. S. Wuu, R. H. Hrong, **C. C. Lin**, and Y. H. Liu, “Characterization of (Ba,Sr)TiO_3 thin-film capacitors with Ir bottom electrodes and its improvement by plasma treatment”, *Microelectronic Engineering*, **66** (2003) 600.

17. D. S. Wuu, R. H. Hrong, F. C. Liao, and **C. C. Lin**, “Nitridation of (Ba,Sr)TiO_3 films in an inductively couple plasma”, *J. non-crystalline Solids*, **280** (2001) 211.

18. R. H. Hrong, D. S. Wuu, C. Y. Kung, **C. C. Lin**, C. C. Leu, T. Y. Haung, and S.

M. Sze, “Ion-implanted treatment of (Ba,Sr)TiO_3 films for DRAM applications**”,** *J. non-crystalline Solids*, **280** (2001) 48.

Conference Papers

1. C. C. Lin, S. P. Lee, K. T. Kuo, and S. Y. Chen, “Engineered Surface with Improved Luminous Efficiency of Phosphor Powder for Plasma Planar Back Light”, Society for Information Display 2005 (SID 2005), Hynes Convention Center, Boston, Massachusetts, U.S.A., May 22nd –27th , 2005.

2. C. C. Lin, S. P. Lee, K. T. Kuo, and S. Y. Chen, “Improved luminescent efficiency of PDP blue phosphor by microwave irradiation”, 2005 MRS Spring Meeting, San Francisco, California, U. S. A., March 28th - April 1st ,2005.

3. T. Y. Liu, H. C. Liao, **C. C. Lin**, S. S. Hu, C. S. Hsiao and S. Y. Chen, “Immobilization of proteins on arrayed ZnO nanorods grown on thermoplastic polyurethane (TPU) flexible substrate for biomedical applications”, 2005 MRS Spring Meeting, San Francisco, California, U. S. A., March 28th - April 1st ,2005.

4. C. C. Lin, S. P. Lee, K. T. Kuo, and S. Y. Chen, “Study on luminous phosphor with improved luminous efficiency for plasma planar back light”, International Display Manufacturing Conferences (IDMC) 2005, Taipei, Taiwan, Feb. 21st- 24th, 2005.

5. C. C. Lin, H. C. Liao, H. P. Chen, and S. Y. Chen, “ Luminescent and structural properties of ZnO nanorods by post annealing”, The 1st international conference on one-dimensional nanomatetrials, Taipei, Taiwan, Jan. 10th-14th, 2005.

6. C. S. Hsiao, **C. C. Lin**, H. P. Chen, and S.Y. Chen, “Tunable growth of patterned ZnO nanorods synthesized in aqueous solutions at low temperatures”, The 1st international conference on one-dimensional nanomatetrials, Taipei, Taiwan, Jan. 10th-14th, 2005.

7. P. C. Kuo, **C. C. Lin**, H. C. Liao, and S. Y. Chen, “Synthesis and properties of

ZnS/ZnO core-shell nanotube arrays", The 1st international conference on one-dimensional nanomatetrials, Taipei, Taiwan, Jan. 10th-14th, 2005.

8. H. C. Liao, **C. C. Lin**, H. P. Chen, and S. Y. Chen "Photoluminescence study of arrayed ZnO nanorods on flexible substrate with hydrogen plasma treatment", International Electron Devices and Materials Symposia, Hsinchu, Taiwan, Dec. 20th -24th , 2004.

9. C. C. Lin, H. P. Chen, and S. Y. Chen, "Hydrogen plasma treatment effects on optical and electrical properties of ZnO nanorods", Taiwan International Conference on Nano Science and Technology, Hsinchu, Taiwan, June 30th - July 3rd , 2004.

10. C. C. Lin, S. Y. Chen, and S. Y. Cheng, "Physical characteristics and photoluminescence properties of Phosphrous-implanted ZnO thin films", First International Meeting on Applied Physics, Badajoz, Spain, Oct. 13rd-18th, 2003.

11. K. H. Liu, **C. C. Lin**, and S. Y. Chen, "Formation of Zn-ZnO polygon prismatic nanocrystals by liquid source via thermal vapor transport", First International Meeting on Applied Physics, Badajoz, Spain, Oct. 13rd-18th, 2003.

12. D. S. Wuu, Y. H. Liu, R. H. Horng, and **C. C. Lin**, "Characterization of (Ba, Sr)TiO_3 thin-film capacitors with Ir bottom electrodes and its improvement by plasma treatment", IUMRS-ICEM 2002, Xi'an, China, June 10th-14th, No. P023.

13. C. C. Lin, R. H. Horng, and D. S. Wuu, "Study of electrical and dielectric properties of (Ba,Sr)TiO_3 films on multi-layer Ir-Pt bottom electrodes", IEDMS, Chung-Li, Taiwan, Dec. 20th-21st, 2000.

14. D. S. Wuu, R. H. Horng, F. C. Liao, and **C. C. Lin**, "Nitridation of (Ba,Sr)TiO_3 thin films in an inductively coupled plasma", 3rd symposium SiO_2 and advanced dielectrics, France, June 19th-21st, 2000 (G-1).

15. R. H. Horng, D. S. Wuu, **C. C. Lin**, T. Y. Haung and S. M. SZE, "Ion-implanted treatment (Ba,Sr)TiO_3 thin films for the DRAM application", 3rd symposium SiO_2 and advanced dielectrics, France, June 19th-21st, 2000 (I-4).

Patents

1. S. Y. Chen, **C. C. Lin**, and H. P. Chen, "Highly arrayed nitrogen-doped *p*-type ZnO nanorods with low temperature process", Taiwan patent: I243096 (2005).

2. S. Y. Chen, and **C. C. Lin**, "High carrier concentration of *p*-type ZnO thin films with nitrogen-implanted treatment", Taiwan patent: I243433 (2005).